

RADIATIVE TRANSPORT MODELING TO IMPROVE *IN VIVO* OPTICAL DETECTION
OF MYCOBACTERIUM TUBERCULOSIS

A Dissertation

by

MADELEINE SIMONNE DURKEE

Submitted to the Office of Graduate and Professional Studies of
Texas A&M University
in partial fulfillment of the requirements for the degree of

DOCTOR OF PHILOSOPHY

Chair of Committee,	Kristen C. Maitland
Committee Members,	Vladislav Yakovlev
	Gerard L. Cote
	Jeffrey D. Cirillo
Head of Department,	Michael J. McShane

August 2018

Major Subject: Biomedical Engineering

Copyright 2018 Madeleine S. Durkee

ABSTRACT

Tuberculosis (TB) is the deadliest disease caused by a single organism, killing 1.7 million people in 2016. TB is especially deadly in immuno-compromised populations, including HIV-positive patients and children. In 2014, HIV-associated TB was responsible for roughly one-third of all deaths associated with HIV/AIDS, and TB was one of the top ten causes of death in children. Additionally, drug resistant strains of the causative agent, *Mycobacterium tuberculosis* (Mtb), have emerged, and those infected with these strains have an elevated mortality rate. There is a need for a rapid testing of new treatment regimens in pre-clinical studies, and a need for a sensitive, rapid diagnostic tool for childhood TB.

In vivo optical detection of Mtb has previously been used to study disease pathogenesis in small animal models. However, whole-animal imaging suffers from a high detection threshold and high-intensity tissue autofluorescence (TAF) background signal. Intravital illumination of the lung has significantly reduced this detection threshold and is a potential tool for longitudinal studies of therapeutic efficacy. However, the system is not robust enough to provide reproducible results at low bacterial doses, and its current detection threshold is 1-2 orders of magnitude higher than the infectious dose of Mtb. We have developed an optical model of the mouse torso and Mtb infection to understand the physiological limitations imposed on the optical system and the sensitivity of the system to experimental variability. The optical model is validated with multiple iterations of phantoms to assess the capability of the model to simulate radiative transport in three-dimensional complex structures, porous and multi-layered materials, and fluorescent materials. We explore the efficacy of different illumination methods and show the system sensitivity to manipulations of the intravital source. The optical model also shows that the

tissue-limited detection threshold of the system is between 10 and 100 colony forming units, and that TAF will further increase this detection threshold if the TAF cannot be spectrally separated from bacteria fluorescence. The fluorescence model is extrapolated to a human child, showing the potential to detect a manifestation of childhood TB known as miliary TB. Finally, we simulate and test an external mirror device to enhance luminescence collection in a mouse model of infection. The validated fluorescence model of infection is shown to accurately replicate previous pre-clinical experiments and accurately predicts the signal enhancements provided by external mirror devices. The extrapolation of the model to the torso of a human child is expected to be a valid preliminary estimate of the performance of the optical system as a clinical diagnostic of TB in children.

ACKNOWLEDGEMENTS

I would like to thank my committee chair, Dr. Kristen Maitland, for her unwavering support and encouragement throughout my Ph.D. work, including invaluable professional and technical advice. Thank you to my committee members, Dr. Jeffrey Cirillo, Dr. Gerard Cote, and Dr. Vladislav Yakovlev, for their guidance throughout the course of this research. I would also like to thank Dr. Kenith Meissner, Dr. Brian Applegate, Dr. Jeremy Wasser, Dr. Andreea Trache, Dr. Michael McShane, and Carl Johnson for their various forms of teaching, support, and mentorship over the past five years.

My friends and colleagues at Texas A&M have also provided immense support throughout my degree. A special thanks goes to Grace Fletcher for providing me with both comic relief and sanity while writing this dissertation. I would like to acknowledge my lab mates and all students involved with the Texas A&M chapter of SPIE for contributing to the diversity of my experience and technical background by helping me explore topics tangentially related to this research. In particular, I would like to acknowledge Taylor Hinsdale, Haley Marks, and Cory Olsovsky for many memorable technical discussions which broadened my understanding of physics, optics, and biomedical sciences.

I have also been very lucky to have powerful female role models in my mentors and colleagues. Here, I would like to re-acknowledge Dr. Kristen Maitland, Dr. Haley Marks, and Grace Fletcher for personal, professional, and technical guidance throughout my degree. I would also like to acknowledge my first research mentor, Dr. Christina Marasco, without whom I would never have taken this path, and I would like to thank Kris Gerrick, Paula Durkee, and Eloura Durkee for teaching me from a young age about tenacity, hard work, and perseverance.

Finally, I would like to thank my family, who have always been supportive of me throughout my education. My mother, Paula; father, John; sister, Eloura; and brother, Mitchell have all been so helpful and understanding through the years of studying, researching, and writing. They have been a never-ending source of encouragement, comfort, and oft-needed laughter. I would also like to thank the rest of my friends and family, who have all been so supportive and a great source of strength through my entire education.

CONTRIBUTORS AND FUNDING SOURCES

Contributors

This work was supported by a dissertation committee consisting of Dr. Kristen C. Maitland, Dr. Vladislav Yakovlev, Dr. Gerard Cote, and Dr. Michael McShane of the Department of Biomedical Engineering and Professor Jeffrey Cirillo of the Department of Microbial Pathogenesis and Immunology at the Texas A&M Health Science Center.

Funding Sources

Funding for the work related to this thesis was provided by the following grants: National Science Foundation CAREER Award (CBET-1254767); National Institute of Allergy and Infectious Diseases (R01AI104960).

NOMENCLATURE

3D	three-dimensional
ANSI	American national standards institute
ASL	airway surface liquid
BCG	bacille Calmette-Guérin
CAD	computer-aided design
CFU	colony forming units
EM	electromagnetic
ERV	expiratory reserve volume
<i>ex vivo</i>	tissue from an organism outside of the natural environment
FRC	functional reserve capacity
FRET	Forster resonance energy transfer
<i>g</i>	anisotropy factor
HIV	human immunodeficiency virus
HRME	high-resolution micro-endoscope
IACUC	institutional animal care and use committee
IAD	inverse adding-doubling
IC	inspiratory capacity
IGRA	interferon-gamma release assay
<i>in vivo</i>	in a living organism
INH	isoniazid
IRV	inspiratory reserve volume

IS	integrating sphere
LTBI	latent tuberculosis infection
Mtb	<i>Mycobacterium tuberculosis</i>
MC	Monte Carlo
MCML	multi-layer Monte Carlo
MDR-TB	multi-drug resistant tuberculosis
MFP	mean free path
MPE	maximum permissible exposure
NIR	near infrared
PDMS	polydimethylsiloxane
R	reflectance
REF	reporter enzyme fluorescence
RIF	rifampin
ROI	region of interest
RTE	radiative transport equation
RV	residual volume
SNR	signal to noise ratio
T	transmittance
TAF	tissue autofluorescence
TB	tuberculosis
TiO ₂	titanium dioxide
TLC	total lung capacity
TST	tuberculin skin test

TV	tidal volume
μ_a	absorption coefficient
μ_s	scattering coefficient
μ_s'	reduced scattering coefficient
VC	vital capacity
V_{Tmax}	maximum tidal volume
WHO	World Health Organization
XDR-TB	extremely drug resistant tuberculosis

TABLE OF CONTENTS

	Page
ABSTRACT.....	ii
ACKNOWLEDGEMENTS.....	iv
CONTRIBUTORS AND FUNDING SOURCES.....	vi
NOMENCLATURE.....	vii
TABLE OF CONTENTS.....	x
LIST OF FIGURES.....	xii
LIST OF TABLES.....	xx
1. INTRODUCTION AND MOTIVATION.....	1
1.1 Tuberculosis: Disease burden and pathogenesis.....	1
1.2 Current diagnostic methods: strengths and weaknesses.....	4
1.3 Pre-clinical studies for therapy development.....	7
1.4 Exploiting optics to address the TB epidemic.....	7
2. TECHNICAL BACKGROUND.....	9
2.1 Optical imaging and sensing of pathogenic bacteria.....	9
2.2 Integrated imaging system for in vivo detection of pathogenic bacteria.....	11
2.3 Radiative transport: A brief overview.....	12
2.4 Monte Carlo Modeling.....	21
2.5 Optical tissue phantoms.....	23
3. OPTICAL PHANTOM DESIGN AND FABRICATION.....	25
3.1 Optical phantoms as simulation validation.....	25
3.2 Material optical properties.....	27
3.3 Advanced methods for complex, multi-layer structure.....	33
3.4 Geometry verification and optical imaging.....	35
3.5 Full torso and sparse tissue phantom design.....	37
3.6 Optical phantom stability and tunability.....	39
4. MULTI-LAYER MIE SCATTERING MODEL FOR ALVEOLAR SCATTERING.....	42
4.1 Concentric sphere Mie scattering model.....	42
4.2 Phantom validation of concentric Mie model.....	44
4.3 Pulmonary alveoli as concentric spheres.....	45

4.4 Scattering properties of lung parenchyma along respiration	47
4.5 Modeling pathogenic states and animal models of disease	49
5. MONTE CARLO MODELING FOR OPTIMAL ILLUMINATION OF MOUSE LUNG	54
5.1 Illumination of mouse lung for detecting fluorescent targets	54
5.2 Phantom design and simulation validation	57
5.3 Simulation design of murine anatomy and optical properties.....	61
5.4 Intravital v. external illumination of mouse lung.....	67
5.5 Intravital illumination source manipulation.....	70
5.6 Limitations of illumination model	76
5.7 Summary	78
6. MODELING <i>IN VIVO</i> FLUORESCENCE DETECTION OF PATHOGENIC BACTERIA.....	80
6.1 Expanding the illumination model to cover fluorescence phenomena	80
6.2 Preliminary infection model and validation.....	81
6.3 Improved replication of the murine anatomy: TAF and ASL.....	86
6.4 Spectral unmixing	88
6.5 Infection modeling in advanced murine torso model	90
6.6 Limitations of the infection model.....	98
6.7 Summary of murine model of infection.....	99
6.8 Preliminary model of human anatomy: A clinical outlook.....	102
7. ENHANCEMENT OF LUMINESCENCE COLLECTION USING TURNING MIRRORS.....	108
7.1 Fluorescence detection of bacteria in vivo.....	108
7.2 Phantom validation of model and mirror stage.....	109
7.3 Predicted performance with variable bacterial loads	114
7.4 In vivo imaging of infection with turning mirrors for enhancement	117
7.5 Summary	122
8. CONCLUSION AND OUTLOOK.....	126
8.1 Pre-clinical applications: Improving optical detection	126
8.2 Clinical implications: Potential diagnosis.....	129
REFERENCES	131
APPENDIX A.....	149
APPENDIX B.....	154

LIST OF FIGURES

	Page
Figure 1. Flowchart of the general diagnostic process used to gain a confident diagnosis of TB. Each step has its own time scale ranging from 1 day to 8 weeks.	5
Figure 2. Integrated imaging system: Custom microendoscope (red box) coupled into the IVIS Lumina whole animal imaging system through a light-tight port in the side (red circle). <i>Inset:</i> Diagram of fluorescence microendoscope with filters (EX/EM), lenses (CL, OL), and dichroic mirror (DM). The CCD camera can be used for detection or guidance for source placement.	11
Figure 3. Optical attenuation through an absorbing sample follows an exponential decay.	14
Figure 4. Linear excitation and fluorescence. A photon with sufficient energy to increase a molecules energy state can be absorbed by that molecule, resulting in an electronic transition (green arrows). The molecule undergoes non-radiative vibrational relaxation (red arrow) to the lowest vibrational state within its elevated electronic state. The molecule can then emit a photon through radiative decay (orange arrows), returning to its ground electronic state.	15
Figure 5. Optical attenuation through a scattering sample. Light incident on a particle is redirected rather than absorbed.	16
Figure 6. System for measuring sample reflectance, transmittance, and unscattered transmittance. A) The integrating sphere system used for reflectance and transmittance measurements consists of a collimated light source launched into an integrating sphere. Scattered light is collected with a spectrometer connected to an offset port. Reflectance is measured with the sample at port 2 with port 1 open. Transmittance is measured with the sample at port 1 and port 2 closed. B) The unscattered transmittance pathway consists of the same collimated source incident on the sample, then a pinhole and the detector. This pathway allows for angular characterization of scattering.....	20
Figure 7. Flowchart of the decision process of Monte Carlo models of radiative transport. This decision process continues for the lifespan of a single photon. It is repeated for every photon launched in the model.	22
Figure 8. Flow diagram of fabrication of optical tissue phantom. (A) Determine optimal recipe for target optical properties of tissue of interest. (B) Verify recipe. (C) Design internal structure. (D) Print internal structure using dissolvable material. (E) Vapor polish printed part to smooth surface. (F) Mix polymer and optical particles, and pour into heat-resistant mold. (G) Degas and cure polydimethylsiloxane (PDMS). (H) Dissolve printed part to create internal void. (I) verify phantom geometry and optical properties.	26

- Figure 9. Trends in absorption coefficient for India ink and TiO₂ concentration. Absorption coefficients are shown for a range of India ink and titanium dioxide concentrations at 488 nm (A), 535 nm (B), 630 nm (C), and 775 nm (D). Absorption is low for low concentrations for both particles, and generally increases with concentrations of each particles. A plateau is reached between 5-7.5 μ L India ink per mL PDMS. The rate of increase depends on the concentration of the other particle and the wavelength. 28
- Figure 10. Trends in reduced scattering coefficient for India ink and TiO₂ concentration. Reduced scattering coefficients are shown for a range of India ink and titanium dioxide concentrations at 488 nm (A), 535 nm (B), 630 nm (C), and 775 nm (D). The reduced scattering coefficient is low for low concentrations for both particles, and generally increases with concentrations of each. Like absorption, the rate of increase depends on the concentration of the other particle and the wavelength. 29
- Figure 11. Interdependency of optical properties on India ink and TiO₂ concentration. Absorption coefficients and reduced scattering coefficients are shown for recipes with a constant TiO₂ concentration of 1 mg/mL PDMS (A, B) and constant India ink concentration of 5 μ L/mL PDMS (C, D). Panel (B) shows that scattering coefficient will change with a constant TiO₂ concentration when India ink concentration is varied, and panel (C) shows that absorption coefficient will change for a constant India ink concentration when TiO₂ is varied..... 30
- Figure 12. Mixing effects on optical scattering. Improper mixing of the uncured polymer and optical particles can result in a shift in the optical properties. The poorly mixed phantom represented in this figure showed settling of TiO₂ particles prior to curing.. 31
- Figure 13. Representative airway phantoms with low scattering coefficient material to illustrate successful and suboptimal fabrication. Vapor polishing and degassing are integral steps in producing a phantom that has minimal uncharacterized scattering elements. A-B) White light images of phantoms without vapor polishing and degassing (A) and with vapor polishing and degassing (B). C-D) Phantoms from A-B are illuminated with 535 nm light. Insets from (C) are shown to depict scattering effects of 1) air bubbles and 2) a rough 3D printed surface. E) Rendering of an optical simulation based on the computer aided design (CAD) model used for the phantom fabrication..... 34
- Figure 14. Validation of airway geometry. A segmented micro-computed tomography image of an optically turbid phantom reveals an air bubble near the airway surface..... 36
- Figure 15. Imaging of phantoms with internal illumination. A computer simulation of the phantom (A) demonstrates the orientation of the internal geometry and source placement (yellow star) for the phantom images in panels (C) and (D). A segmented micro-CT scan of the healthy lung tissue phantom (B) confirms the internal structure is present in the optically opaque phantom. The mock airway is used as a pathway for the endoscope for internal illumination of the optical phantoms at a wavelength of 535 nm. The two phantoms imaged with internal

illumination are identical in external shape and internal structure, with material optical properties optimized for healthy (C) and inflamed (D) lung tissue. All images and renderings are on the same scale. Scale bar in panel (C) is 1 cm.....	37
Figure 16. Inflated lung tissue modeled by glass microbubble phantoms. Fluorescence confocal images show an increase in microbubble concentration consistent with the intended recipe.	38
Figure 17. Flowchart of fabrication process for mouse torso phantoms. Uncured PDMS with the optical properties of lung tissue is loaded with microbubbles to represent inflated lung (A). The uncured mixture is placed in a lung-shaped clamp mold (C) with a 3D printed, dissolvable airway (B). The lung mold is degassed and heat cured (D). The cured lung phantom is secured in a cylindrical mold (E) and PDMS representing optical properties of bulk tissue is poured into the mold (shown optically clear for demonstration). This layer is degassed and cured, and the entire phantom is placed in a heated base bath to dissolve the internal airway (F). The final phantom (G) is shown with a clear bulk tissue layer and an absorbing lung layer for visualization.	39
Figure 18. Spherical particles modeled in traditional Mie scattering (a) and in the concentric sphere model (b).....	42
Figure 19. Phantom validation of the concentric sphere model shows a fairly constant μ_s for each volume fraction over the visible spectrum (a). The change in μ_s is linearly correlated with volume fraction in both the phantoms and the simulation (b).....	45
Figure 20. Lung parenchyma consists of microscale air sacs connected by airway branching (a). The alveoli expand and contract over the respiratory cycle for passive and forced inspiration and expiration (b-c). Residual volume (RV) is the minimal airspace a living organism can achieve without alveolar collapse. Expiratory reserve volume (ERV) is the difference between RV and passive breathing (forced exhale). Functional residual capacity (FRC) is the air volume in the lung at the end of passive breathing. Tidal volume (TV) is the volume fluctuation during passive breathing. Inspiratory reserve volume (IRV) is the difference between passive breathing and total lung capacity (TLC).	46
Figure 21. At a constant lung volume, μ_s is similar for all ASL thicknesses modeled (a). The change in baseline and phase of g (b) causes a shift in μ_s' and leads to unique spectral features (c).	50
Figure 22. Fluorescence whole-animal imaging of mice can be accomplished through multiple illumination pathways including (a) external epi-illumination, (b) external trans-illumination, and (c) internal illumination with a microendoscope (ME) light source. 55	
Figure 23. Position of the mouse in the imaging system effects collected fluorescence. Mice were intratracheally infected with 10^6 colony forming units BCG and administered REF substrate 24 hours post-infection. Fluorescence distribution is different with external epi-illumination in the ventral (a) and dorsal (b) position. Under the same infection conditions, detected fluorescence intensity with internal illumination also	

varies for mice imaged in the ventral (c) and dorsal (d) positions. Although the fluorescence signal is higher in the ventral position (c), the signal to noise ratio was found to be significantly higher for the dorsal position (d).⁸³ All radiance values are measured in photons/second/cm²/steradian..... 56

Figure 24. 3D models for photon transport in LightTools. The rectangular phantom used for validation studies has a 4-generation fractal tree as a model airway (a). The full-torso model of the mouse includes a more anatomically accurate model airway (b) and lungs of comparable volume to that of a mouse. The lung and heart are immersed in a cylindrical model of other soft tissues (d-e). The star in (b) is the location of the internal illumination source..... 59

Figure 25. Validation of the computational model with IVIS imaging of optical phantoms shows a similar irradiance profile at the phantom surface. Phantom 535 is shown here illuminated internally with 535 nm (a) and 730 nm (c) microendoscope sources. The simulation replicates total flux output to the detector (Table 15) and the irradiance profile at 535 nm (b) and 730 nm (d). 60

Figure 26. Maximum intensity projections of fluence rate (mW/mm²) are shown for ventral external illumination (a, d), dorsal external illumination (b, e), and internal illumination (c, f). Greater penetration can be seen at the excitation wavelength for the REF NIR probe (d-f) compared to that of tdTomato (a-c). All projections with epi-illumination are normalized to have the same maximum. Internal illumination projections are saturated to that maximum to better represent the fluence rate on the same scale. The average fluence rate within the lung decreases exponentially with distance away from the source for both external illumination (g) and internal illumination (h)..... 68

Figure 27. The fluence rate in the lung is sensitive to the parameters of the internal source, including diffuser tip (a), fiber position (b), and divergence angle of the fiber (c). The efficiency of a fiber diffuser increases as more source power is emitted through the tip of the fiber rather than radially (d). The microendoscope (ME) efficiency is more sensitive to position (e) than divergence angle (f). The average fluence rate in the lung follows similar trends to efficiency for all source manipulations (g-i)..... 71

Figure 28. The three-dimensional illumination of the lung is shown for 535 nm (a-d) and 730 nm (e-h). Maximum intensity projections of the fluence rate (mW/mm²) in the coronal plane (a, d), sagittal plane (b, e), and transverse plane (c, f). A mask of the lung is also shown in each projection. (g) 3D rendering of the illumination is shown for both wavelengths. 75

Figure 29. Validation of the fluorescence simulation. A) The IVIS image of the optical phantom shows the fluorescing capillary tubes emerging from the phantom. B) The optical simulations shows a very similar fluorescence distribution, with a percent error in radiant efficiency of only 2.36%. 82

Figure 30. A) Fluorescence signal from model related to bacterial load. Simulations of infections below the level of detection are not shown for clarity. For an evenly distributed infection, signal is expected to be linearly related to bacterial load in this simplified model. B) A characteristic irradiance map of a high bacterial load simulation is shown to reference the spatial distribution of fluorescence signal. 83

Figure 31. A) Predicted fluorescence signal after excitation with a fiber diffuser. The illumination profile of the fiber diffuser varies from 100% power coming from the tip of the diffuser (0/100) to only 25% reaching the tip, the remaining 75% of the power emitted from the length of the diffuser (75/25). ME: current microendoscope. B) Incident power density on a plane bisecting the torso model. The trachea is delineated in blue to show that fluorescence signal detected at lower CFU is in response to simulated bacteria residing in the trachea, and not the lung tissue. 84

Figure 32. Predicted fluorescence signal collected after excitation with a fiber source of varying numerical aperture..... 85

Figure 33. Effects of ASL on illumination. A) A 3D representation of the torso structure in the simulation. The ASL is noted on the inset. B-E) Illumination on a plane bisecting the lung layer of the phantom. Panels B&C show illumination with the ASL included in the model with the internal source offset (B) and in contact with the ASL. Panels D&E show illumination with no ASL modeled with the source offset (D) and in contact (E) with the tissue at the tracheal bifurcation..... 87

Figure 34. Simulated tissue autofluorescence spectra when the tissue is illuminated with 535 nm light (black) and 730 nm light (red). Spectra are normalized to the 535 nm TAF peak. 88

Figure 35. tdTomato fluorescence traversing perfused tissue. As emitted photons travel through perfused tissue, the higher energy photons are more likely to be absorbed by hemoglobin. The result is a red-shifted fluorescence spectrum. The peak of the resulting spectrum (orange) will continue to shift from the original spectrum (blue) as it travels through more tissue. When sampled at discrete spectral points the shape of the spectrum appears quite different. 90

Figure 36. Different mechanisms for detection fluorescence from bacteria include genetic modification (left), and sensing with an external molecular beacon (right). 91

Figure 37. Unmixed tdTomato and CNIR probe fluorescence. A) For epi-illumination simulations, the unmixed detection threshold ranged from 10^3 - 10^4 CFU. Error bars represent the post-unmixing standard deviation with $n = 3$ simulations. B) Trans-illumination simulations showed a detection threshold of 10^3 CFU, which was not dependent on position. C-D) Internal illumination yielded a wavelength-dependent detection threshold at every collection position. 94

Figure 38. Signal at the microendoscope tip and dorsal collection for six different positions of the microendoscope. No correlation between microendoscope signal and dorsal fluorescence was found for tdTomato (A) or CNIR probe (B). 96

Figure 39. Simulated fluorescence signal with internal illumination sources of 20° and 40° divergence angles. Only ventral collection with 10⁴ CFU showed significant enhancement in the tdTomato range (p < 0.05) with increased divergence angle (A). Both dorsal and ventral collection with 10² CFU showed significant enhancement in the NIR range (p < 0.05) with increased divergence angle (B). However, there was also a significant decrease in fluorescence collection in the ventral position for 10⁶ CFU in the NIR range (p < 0.05). 97

Figure 40. A) Tissue autofluorescence decreases at higher wavelengths for external illumination in any position (VD = ventral illumination with dorsal collection, VV = ventral illumination with ventral collection, DD = dorsal illumination with dorsal collection, DV = dorsal illumination with ventral collection). B) For internal illumination, an inverse trend in tissue autofluorescence signal is found. (II = internal illumination with internal collection, ID = internal illumination with dorsal collection, IV = internal illumination with ventral collection)..... 101

Figure 41. Clinical presentations of TB can vary. Adults usually exhibit cavitory TB, in which the bacteria reside in a focal lesion before reactivation and dissemination. Children more frequently present with miliary TB, a widespread, multifocal infection. Young children are also more susceptible to lymphadenitis of the hilar lymph nodes..... 103

Figure 42. Simulated bacterial fluorescence in a child model of infection indicates that miliary TB in a child could be detected at doses higher than 10⁶ CFU..... 106

Figure 43. A) The mirror stage with 45° angled mirrors for use in the whole-animal imaging system. B) A photoreal rendering of the simulation in LightTools shows the multi-directional view provided by the mirrors. C) The mirrors are expected to enhance fluorescence collection from internal illumination experiments. D) The mirrors are also expected to provide multi-directional illumination in epi-illumination experiments. 109

Figure 44. A) The simulated Xenogen phantom with two embedded LEDs (marked A and B) with angled mirrors. B) Predicted irradiance on the phantom and mirrors with only LED A turned on in the phantom. C) Predicted irradiance on the phantom and mirrors with only LED B turned on in the phantom. Note the image scale is one order of magnitude lower than panels B and D. D) Predicted irradiance on the phantom and mirrors with both LEDs turned on in the phantom..... 110

Figure 45. IVIS imaging of Xenogen phantom. The top row of images show the phantom imaged without the mirror stage. LED illumination is noted on each panel. A direct comparison can be made with the images of the phantom and mirrors below. For LED B imaged with the mirrors, the maximum signal is found on the mirrors..... 111

Figure 46. A statistical comparison shows that the mirrors provide a significant signal enhancement (*p << 0.05) for each source condition in the Xenogen phantom..... 112

Figure 47. Fluorescence from the Xenogen phantom was measured with epi-illumination. The emission filter was held at 580 nm, and the source wavelength was shifted. The

signal enhancement from the mirrors is a result of both multi-directional illumination and multi-directional fluorescence collection.....	113
Figure 48. The multi-directional illumination is shown to enhance fluorescence signal. With the measured ROI covering only the phantom, and not the mirrors in the second row of images in figure 46, a statistically significant enhancement is still found (*p << 0.005).....	113
Figure 49. A) Total fluorescence signal collected from the simulated detector for epi-illumination is shown for the ventral and dorsal positions, with and without the mirror stage for CFU ranging from control to 10 ⁶ . Error bars show average error in the simulation. NOTE: This error cannot be extrapolated to the unmixed data (B and D). B) The unmixed simulated fluorescence signal for epi-illumination shows the scattering-limited detection threshold. A signal enhancement from the mirrors is shown for both positions. C) Total simulated fluorescence signal for internal illumination is shown with ventral and dorsal collection, with and without the mirror stage. D) Unmixing the fluorescence signal shows the expected enhancement provided by the mirror platform for each CFU.	115
Figure 50. The predicted signal enhancement from the mirrors varies with CFU, animal position, and illumination method.....	116
Figure 51. A) Representative spectrally unmixed images of mice imaged ventrally with epi-illumination at 0, 10 ² , 10 ⁴ , and 10 ⁶ CFU. The top and bottom images show the same mouse imaged with and without the mirror platform. B) Representative spectrally unmixed images of mice imaged dorsally with epi-illumination at 0, 10 ² , 10 ⁴ , and 10 ⁶ CFU. The top and bottom images show the same mouse imaged with and without the mirror platform.....	119
Figure 52. Spectrally unmixed data show no significant difference from control for any cohort, with or without the mirrors for ventral (A) or dorsal (B) epi-illumination experiments.	120
Figure 53. A) Representative spectrally unmixed images of mice imaged ventrally with internal illumination at 0, 10 ² , 10 ⁴ , and 10 ⁶ CFU. The top and bottom images show the same mouse imaged with and without the mirror platform. B) Representative spectrally unmixed images of mice imaged dorsally with internal illumination at 0, 10 ² , 10 ⁴ , and 10 ⁶ CFU. The top and bottom images show the same mouse imaged with and without the mirror platform.	121
Figure 54. Spectrally unmixed data show a significant difference from control for only the 10 ⁶ CFU cohort (p < 0.05), with and without the mirrors for internal illumination with ventral collection (A). For dorsal collection, no cohort without the mirrors is different from control. However, with mirrors, 10 ² and 10 ⁶ CFU cohorts are significantly different from “control with mirrors” (p < 0.05).....	121
Figure 55. A) Example spectra of tdTomato and TAF spectra used for spectral unmixing for animal experiments. B) With a control mouse in the ventral position, the TAF	

spectrum varies spatially, with some spectra approaching the shape of the tdTomato spectrum. C) A control mouse in the ventral position also shows variable TAF spectra across the fluorescence overlay..... 124

LIST OF TABLES

	Page
Table 1. A side-by-side comparison of the TST and IGRA diagnostics shows the strengths and weaknesses of each method.....	6
Table 2. Optical properties of healthy and inflamed mouse lung tissue compared to the corresponding phantom recipes for properties at 535 nm.	27
Table 3. Optical properties of healthy and inflamed mouse lung tissue compared to the corresponding phantom recipes for properties at 730 nm.	28
Table 4. Look-up table for phantom recipes at 488 nm base on experimental measurements. Greyed out recipes do not follow the expected trend.....	31
Table 5. Look-up table for phantom recipes at 535 nm base on experimental measurements.	32
Table 6. Look-up table for phantom recipes at 630 nm base on experimental measurements.	32
Table 7. Look-up table for phantom recipes at 775 nm base on experimental measurements.	33
Table 8. Effects of vapor polishing on size of 3D printed internal structure. The molded phantom was also measured for airway size using the micro-CT images for validation of internal geometry.	35
Table 9. Inputs for phantom and tissue models.	48
Table 10. Physiological parameters of the human lung over respiration ^{104, 105}	48
Table 11. Scattering properties of human alveoli at discrete points along the respiratory cycle. Values are averaged over the spectrum modeled. ASL thickness modeled is 0.5% and 1% of r_{alv} at V_{Tmax}	49
Table 12. Alveolar scattering values with pathological thickening of fluid in alveoli (ASL, mucous, or edema fluid).....	51
Table 13. Values describing alveolar physiology for different animal models of pulmonary disease as reported by Mercer <i>et. al.</i> and calculated at maximum tidal volume.	52
Table 14. Alveolar scattering for humans and animal models.....	52
Table 15. Absorption coefficients (μ_a) and reduced scattering coefficients (μ_s') of infected mouse lung and validation phantoms at wavelengths of interest. Percent error between total flux measured experimentally with the phantom and simulated in the model.	61

Table 16. Properties of inflated mouse lung used to calculate approximate optical properties. *Lung tissue volume was calculated from lung volume and an inflation factor of 0.8.....	63
Table 17. Optical properties for other soft tissues from Ref. 30. Values denoted with ‘*’ were calculated from scattering coefficient and anisotropy factor. Values from LightTools biological materials library were used for heart optical properties.	65
Table 18. Decay of fluence rate within lung. Average power was fit to a decaying exponential: $f(x) = a*exp(-b*x)$ where a is the initial average fluence rate at the detection plane nearest the source and b is the decay constant.	69
Table 19. Ability of different illumination sources to couple light into the lung.	69
Table 20. Parameters and performance of optimized internal illumination. The bolded values are represented spatially in Figure 28.	73
Table 21. Values relating source power in the simulations to ANSI standards for MPE of a collimated laser beam on skin for the wavelengths of interest.....	78
Table 22. Simulated detection thresholds for fluorescence detection are wavelength dependent after spectral unmixing for all internal and trans-illumination. The epi-illumination threshold is dependent on the positioning of the mouse.	94
Table 23. Simulated fluorescence signal was linearly correlated with CFU. For epi- and internal illumination, the dorsal position was the most sensitive, while trans-illumination showed no position dependence.	95
Table 24. Total TAF signal scales with wavelength at each position for external illumination. The trend does not hold for internal illumination.	102
Table 25. The simulations predict that the mirrors provide a signal enhancement ranging from 53-82%.	110
Table 26. The measured signal enhancement from the Xenogen phantom agrees well with the simulation, serving as a validation.	112
Table 27. The measured signal enhancement from the multi-directional illumination provided by the mirror device is roughly 45% for every illumination wavelength. If the mirrors are included in the measurement ROI, the enhancement is measured to be ~ 100%.....	114
Table 28. For an individual mouse, the mirrors usually provided a signal enhancement after spectral unmixing. Negative “enhancements” are bolded and italicized. These values are likely due to spectral unmixing errors. Average signal enhancement for each cohort is shown in the bottom section of the table.	122

1. INTRODUCTION AND MOTIVATION

1.1 Tuberculosis: Disease burden and pathogenesis

Tuberculosis (TB) is a deadly disease resulting from infection with the pathogen *Mycobacterium tuberculosis* (Mtb). TB recently surpassed HIV as the deadliest disease caused by a single infectious agent, killing more than 1.8 million people in 2016¹. TB is also one of the leading killers of HIV-positive individuals, and is responsible for roughly one third of deaths associated with HIV/AIDS². Additionally, TB is one of the top ten causes of death in children worldwide. Disease rates are highest in low-resource areas and developing countries, with 94% of cases and 98% of deaths coming from these areas¹. The TB epidemic is a multi-faceted world health problem, and addressing it effectively requires an in-depth understanding of the disease pathogenesis and shortcomings of the current diagnostic and treatment methods.

Mtb is a slow-growing pulmonary pathogen with a complex, multi-stage pathogenesis that is still not fully agreed upon by experts in the field³. Although TB is primarily a result of a pulmonary infection with Mtb, extrapulmonary infections are not uncommon^{4,5}. It is estimated that up to one third of the world population is infected with Mtb; however, only 10-15% of those infected ever develop symptoms of the disease TB⁶. During this asymptomatic infection, known as latent TB infection (LTBI), it is assumed that Mtb remains viable, but dormant within the host until the immune system becomes compromised⁷. Once the latent infection progresses to the active disease, the bacteria becomes transmittable. The most identifiable symptom of TB is a harsh cough, which is also the mode of transmission. A sick individual will cough and expel droplet nuclei, which are small, aerosolized particles containing 1-10 bacilli⁸. These small particles remain aerosolized, and the bacteria inside remain viable for several hours. Therefore,

direct contact with a sick individual is not necessary for disease transmission, rather a prolonged shared airspace⁹. After falling ill, it is estimated that a person will infect up to 20 others before successful diagnosis and treatment¹⁰.

1.1.1 Geographical disease burden

TB predominantly affects low-resource areas, with upwards of 95% of TB-related deaths coming from developing countries. While high-population countries like India and China have the largest number of cases (roughly 23% and 10% of total cases, respectively), sub-Saharan Africa has the highest disease burden, with nearly 300 incident cases per 100,000 individuals¹⁰. Access to healthcare is a limiting factor in many of these areas, and TB requires many visits to the doctor or clinic. A lack of advanced microscopy centers and labs means that a positive diagnosis requires a secondary appointment, and therefore a delay in treatment. While recent developments such as the Xpert MTB/RIF assay have alleviated some of these issues^{11, 12}, the strict antibiotic regimens are difficult for patients to adhere to, which contributes to the emergence of drug-resistant strains of Mtb.

1.1.2 Drug resistance

In addition to a complex disease progression and a low infectious dose, multiple drug-resistant strains of Mtb have emerged. This is due in most part to a lapse in patient compliance with the strict antibiotic regimens that are necessary for treatment¹³. Up to 20% of previously treated TB cases and 3.5% of new cases have been identified as resistant to Rifampin (RIF) and Isoniazid (INH), the two most common frontline antibiotics for TB. This form of drug resistance, known as multidrug-resistant TB (MDR-TB), accounts for 4.1% of new cases and 19% of previously treated cases of TB¹. Additionally, nearly 10% of these MDR-TB cases are also extensively drug-resistant TB (XDR-TB). In addition to RIF and INH resistance, the strains of

Mtb responsible for XDR-TB are also resistant to fluoroquinolones, and at least one other second-tier antibiotic TB treatment¹⁴. Strains of totally drug resistant Mtb have even reportedly been found in India¹⁵. As Mtb continues to evolve to resist current treatments, the demand for new, highly effective treatments and early and effective diagnostic methods also increases.

1.1.3 Vaccine efficacy

Vaccine efficacy is also a factor contributing to the spread of TB. The most widely used TB vaccine is the bovine strain of Mtb, bacille Calmette-Guérin (BCG), a strain with attenuated virulence in humans with sufficient antigen presentation to build an acquired immune response to Mtb antigens. In many populations, the BCG vaccine is up to 80% effective. However, in some populations, the vaccine shows little to no efficacy^{16,17}. Unfortunately, the underperformance of the vaccine coincides with high burden areas, compounding the difficulties in addressing the epidemic¹⁸. Without rapid development methods of new vaccines, preventative treatment for TB will remain ineffective.

1.1.4 Bacterial pathogenesis

As previously mentioned, the most common form of transmission of Mtb is through shared airspace⁸. The infectious dose of bacteria is expected to be as low as 1-10 colony forming units (CFU)¹⁹. Upon preliminary infection, a disease stage with flu-like symptoms, the host immune system recognizes the bacteria as a foreign body. Resident macrophages in the lung parenchyma (alveolar macrophages) then internalize the bacteria and attempt to lyse the cell¹⁸. However, Mtb has evolved to be resistant to this phagocytic process, and multiplies within the phagosome. The infected macrophage will rupture, releasing the multiplied bacteria into the lung. Mtb will also survive within foamy macrophages without rupturing the cell^{20,21}. This process also recruits more macrophages to the site of infection, and the host immune systems attempts to kill the

bacteria. Eventually, the immune system of a non-immunocompromised host will wall off the bacteria, infected macrophages, and dead immune cells into a calcified granuloma.

This concludes the preliminary infection, and many people never experience a relapse. It is unknown whether the bacteria is actually eradicated in these people, or if they live healthily with a latent TB infection (LTBI) encased in these granulomas^{6, 22-24}. In this LTBI stage, the bacteria slip into a slow-metabolic state, and become very difficult to detect. Unfortunately, in 10-15% of LTBI cases, the host immune system becomes compromised and fewer lymphocytes are available to maintain a stable granuloma; granulomas become unstable and rupture, releasing live, active bacteria and necrotic tissue into the lung^{20, 25}. This stage of disease is the symptomatic active stage of TB, with ~70% of untreated cases leading to death²⁶. The immune system attempts to fight this secondary infection as it did in the preliminary infection, but is usually unable to kill or encase the bacteria²⁷⁻²⁹. The patient will essentially drown from the build-up of liquid, necrotic tissue, and dead immune cells that slowly fill the lungs.

1.2 Current diagnostic methods: strengths and weaknesses

One of the factors contributing to the severity of the TB epidemic is the inefficiency of diagnosing the disease. The current gold standard for diagnosing active TB is sputum culture, but this is a multi-step process (Figure 1), with each step having its own limitations. In general, a patient will start with a consultation with a clinician. If the patient is suspected of having an infection, even if they show no signs of active disease, the next step is to test the acquired immune system for a response to Mtb antigens. This will be done with either the tuberculin skin test (TST) or the interferon-gamma release assay (IGRA) blood test³⁰. These methods both have poor sensitivity and specificity in certain populations, on top of general limitations in low

resource settings (Table 1). Given a positive response to this test, the patient will receive a chest x-ray to search for granulomas characteristic of TB within the lung^{31, 32}.

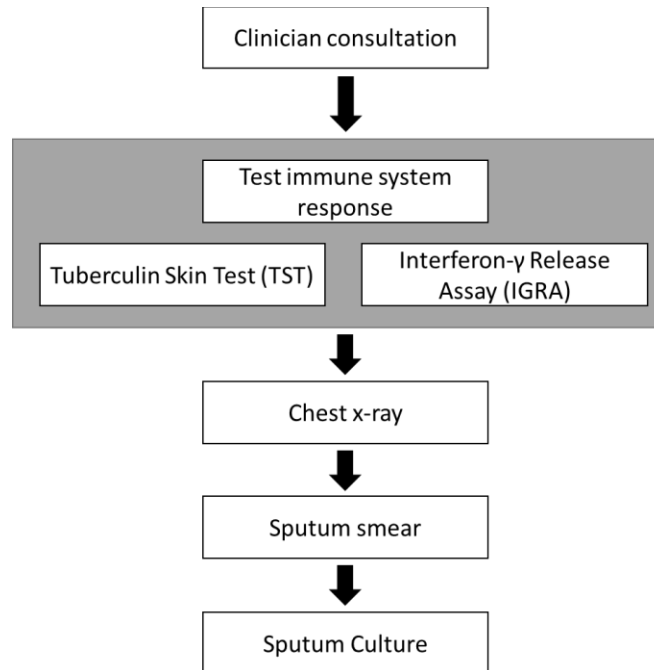


Figure 1. Flowchart of the general diagnostic process used to gain a confident diagnosis of TB.

Each step has its own time scale ranging from 1 day to 8 weeks.

If a patient has severe symptoms of TB, they will often go to direct diagnostic methods, which require collection of the bacteria. Even if a confirmation of infection or previous exposure to Mtb was reached with the TST or IGRA, an active infection cannot be confirmed without further testing, usually acid-fast microscopy and a sputum culture. Mtb has a notoriously slow growth rate, and a positive sputum culture could take up to 10 weeks to confirm that the patient has TB³³. Given the proper equipment, the bacteria can be stained with an acid-fast stain and imaged under white-light microscopy. Although this method is quick, it has a high detection threshold ($\sim 10^4$ CFU), and it is not specific to Mtb, but a larger group of mycobacteria. For low resource settings where TB is most rampant, the long timeline for confirmation with sputum culture can be extended if sputum samples must be sent to an external lab for processing. Within

the past decade, successful diagnostic tests for identifying TB and MDR-TB, such as the Xpert Mtb/RIF assay, have been recently developed using antigen and biomarker recognition techniques³⁴. While these methods are improving diagnostic yield and time, there are still some shortcomings, specifically the efficacy of the diagnostic in children.

Table 1. A side-by-side comparison of the TST and IGRA diagnostics shows the strengths and weaknesses of each method.

	Tuberculin Skin Test (TST)	Interferon-γ Release Assay (IGRA)
<i>False positive for BCG vaccinated patients</i>	Yes	No
<i>False negative for immunocompromised (HIV)</i>	Yes	Yes
<i>Number of appointments required</i>	2; one for injection and another 48-72 hours later for analysis	1; results available within 24-30 hours
<i>Differentiate between active and latent infection</i>	No	No
<i>Method of detection</i>	Acquired inflammatory response in vivo	Acquired inflammatory response ex vivo
<i>Preferred for testing infants/pregnant mothers</i>	Yes/Yes	No/Ask doctor
<i>Acceptable test for recent exposure to Mtb</i>	No	No

Diagnosing an active infection via sputum culture is also problematic for infection young children. Infants are susceptible to pulmonary infection with Mtb, but are not prime candidates for the diagnostic methods above due an under-developed immune system and an inability to expectorate³⁵. In developed countries, gastric aspiration is available as an alternative to sputum culture in young children, but these methods are simply not available or even feasible in low resource areas. This expresses a need for a sensitive point-of-care method of diagnosis which does not require an immunogenic test or sputum culture to confirm an active infection.

1.3 Pre-clinical studies for therapy development

The rise of drug resistance in strains of Mtb increases the need for new antibiotics and antibiotic regimens. Development of new treatments for MDR-TB and XDR-TB patients is hindered by the slow growth rate of Mtb and a minimal understanding of the mycobacterium's complex, multi-stage pathogenesis^{18, 22, 23}. Animal studies on disease pathogenesis require a large number of animals because disease progression is tracked by sacrificing animals at discrete time points, then excising, homogenizing, and culturing the lungs to enumerate bacteria^{36, 37}. Not only does this method require a large sample size (multiple animals at each time point), but it discards vital information that could be gained from monitoring infection in a single organism over time. Pre-clinical studies on potential therapeutics also use this method of sacrificing at selected stages to quantify the reduction of CFU in the lung and consequently treatment efficacy^{37, 38}. Utilizing a method which would allow longitudinal studies on treated animals could maximize information gained from pre-clinical experiments while simultaneously reducing costs and number of animals required to achieve significant results.

1.4 Exploiting optics to address the TB epidemic

Difficulties exist on all fronts when it comes to treating the TB epidemic; all but the newest diagnostics have low sensitivity and/or specificity, drug-resistant strains render even our most advanced antibiotics ineffective, and vaccination is completely ineffective in some populations. To address these problems, we look more specifically at where current medical technologies can alleviate the disease burden. First, diagnosis of TB has a few clear problems: 1) diagnosis by sputum culture is too slow, 2) rapid diagnosis by smear microscopy is not sensitive enough, and not accessible in areas of high burden, and 3) infants children cannot produce sputum to get a proper diagnosis. All of these problems with diagnosis involve sputum. Even the Xpert

MTB/RIF diagnostic, which has shown great potential for improving rapid diagnosis of TB and MDR-TB, is ineffective in small children because it requires a sputum sample. Secondly, the development of new reactionary and preventative therapies is greatly hindered by the slow growth rate of Mtb. Pre-clinical studies on new treatments and vaccines require a high number of animals and/or a long post-sacrifice culture step.

Optical technologies show potential to address both of these problems. In addressing diagnosis, especially in small children, optical imaging or sensing of virulent bacteria would provide rapid feedback if the quantification of bacteria could be tied to an optical signal. However, an even more accessible goal is to design optical tools for pre-clinical analyses for development of TB therapies and vaccines. Optical imaging of animals during pre-clinical studies allows for longitudinal studies. If an optical signal can be confidently correlated to a bacterial load, a single animal can be imaged over the course of an infection, rather than multiple animals being sacrificed at discrete time points. Pre-clinical studies also allow for genetic modification of pathogens, rather than sensing wild-type bacteria with an exogenous chemical. With a method for linking bacterial load to an optical signal, detecting bacteria transforms from a biological/biochemical problem into and bio-optical engineering problem.

2. TECHNICAL BACKGROUND

2.1 *Optical imaging and sensing of pathogenic bacteria*

Addressing the TB epidemic requires a multi-pronged approach including development of new diagnostics and therapies, methods for minimizing transmission of Mtb, and research into the complex pathogenesis of the disease. Optical sensing and imaging has been used to observe disease pathogenesis in small animal models and even in preliminary studies for the development of antibiotic treatment regimens³⁹⁻⁴³. Different methods exist for detection of viable bacteria. First, a bovine strain of the bacteria, bacille Calmette-Guérin (BCG) can be transfected as a fluorescent vector to make the bacteria produce the tdTomato fluorescent protein. Because the bacteria itself fluoresces when transfected with this vector, there is no baseline fluorescence associated with an exogenous probe. However, the excitation and emission wavelengths of tdTomato lie in the range of visible wavelengths, and biological tissue has a high optical attenuation and high tissue autofluorescence (TAF) in this spectral range. This physiological phenomenon limits the signal to noise ratio (SNR) of *in vivo* detection optical systems.

Another method for detecting viable bacteria is through using an exogenous fluorogenic probe. *Xie et al* have developed an NIR fluorescent probe that is sensitive to the class C beta-lactamase enzyme, a surface enzyme expressed by a small group of mycobacteria, including Mtb⁴⁴. This probe consists of a NIR fluorophore connected to a large organic quenching molecule by a lactam ring. When the molecule is intact, the fluorescence from the NIR dye is quenched through Forster resonance energy transfer (FRET). However, if the molecule is

* Portions reprinted with permission from “Optical model of the murine lung to optimize pulmonary illumination” by Durkee, Madeleine S., Nooshabadi, Fatemeh, Cirillo, Jeffrey D., Maitland, Kristen C., 2018. *Journal of Biomedical Optics*, 23, 071208, Copyright 2018 by International Society for Optics and Photonics.

cleaved by a beta-lactamase enzyme on the surface of a bacterium, the large tail of the probe is no longer close enough to the fluorophore to quench fluorescence via FRET, and the remaining marker will fluoresce. This method has two main advantages 1) NIR light is much less attenuated by biological tissue and produces less TAF, so a higher SNR is theoretically possible, and 2) because this method can detect wild-type bacteria, there is potential for translation to a clinical diagnostic tool. However, this sensing method also has downsides. The probe enters the bloodstream of the animal, and is broken down by the body, so fluorescence can be generated even if there are no bacteria present. Also, an exogenous probe will be broken down and cleared by the body. The marker will therefore have a pharmacokinetic time scale of efficacy^{39, 41}, unlike imaging transfected bacteria, which have no time-dependence on signal intensity because the infection is not cleared by the body.

Recently, the incorporation of an internal illumination source has improved the sensitivity of optical detection for both of the previously mentioned detection schemes to be within the range of physiologic doses of bacteria^{41, 45}. Previously, a high detection threshold of $>10^5$ colony forming units (CFU)⁴⁰ prevented the use of these optical tools in pre-clinical trials because the reduction of CFU could not be monitored along the course of treatment. The use of a fiber microendoscope for intravital illumination has shown a reduction of that detection threshold to $\sim 10^3$ CFU in the visible spectrum (tdTomato-transfected BCG)⁴⁵ and $\sim 10^2$ CFU in the NIR (exogenous bacteria-sensing probe)⁴¹. These detection thresholds come from experiments with intravital illumination with external detection, and while this method works for experiments with small animal imaging, internal fluorescence collection with the microendoscope would help to translate this method to a clinical diagnostic tool.

2.2 Integrated imaging system for *in vivo* detection of pathogenic bacteria

In previous research, a multiscale imaging system was designed and tested to improve the detection of BCG and Mtb *in vivo*^{41, 45, 46}. This system includes a high-resolution microendoscope (HRME) and the IVIS Lumina small animal imaging system (Figure 2). The HRME consists of an LED or laser diode source depending on the operating wavelength, collimating optics if necessary, excitation and emission filters, a dichroic mirror, objective lens, and CCD camera. The excitation light is projected through the objective lens and coupled into a 10,000-microfiber endoscope with an outer diameter of 0.66 mm. This endoscope is fed through a light-tight port in the side of the IVIS, and used for intravital illumination of the animal. Fluorescence can be collected through the HRME or through the external IVIS camera.

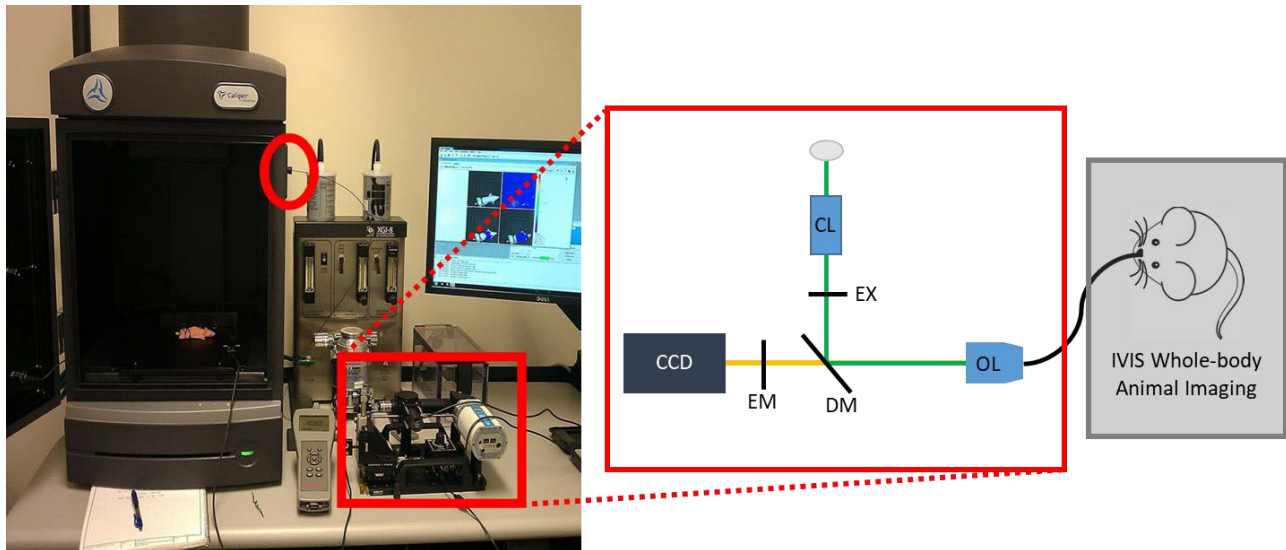


Figure 2. Integrated imaging system: Custom microendoscope (red box) coupled into the IVIS Lumina whole animal imaging system through a light-tight port in the side (red circle). *Inset:* Diagram of fluorescence microendoscope with filters (EX/EM), lenses (CL, OL), and dichroic mirror (DM). The CCD camera can be used for detection or guidance for source placement.

While this system has already shown improvement in the detection level of bacteria and potential for correlating fluorescence signal with bacterial load, the effects of both physiologic and instrument variables are unknown. Rather than optimizing this system through multiple iterations of animal experiments, we have developed a radiative transport model of the mouse torso to computationally assess the current status of the system and predict effective improvements to the instrumentation to overcome any currently limiting variables. Simulations also provide the opportunity to expand the size of the tissue representation from mouse lungs to larger mammalian lungs for a prediction as to how this technology would behave in larger animal models and if it would translate well into clinical studies. The mouse and other rodent lung models will aid longitudinal studies on therapeutic treatments for TB with the goal of determining the bacterial load within the animal, while the human model will simply aim to provide a yes/no diagnosis of bacterial infection. It is important to point out that the optimized imaging system is only intended to diagnose active TB infections and not LTBI.

2.3 Radiative transport: A brief overview

Radiative transport generally refers to the interaction of electromagnetic (EM) radiation with matter. Radiative transport is fundamentally explained by Maxwell's equations, which characterize the response of both the electric and magnetic field components of a wave incident on a material⁴⁷. Maxwell's equations can be used across all size scales, given enough computational power. The radiative transport equation (RTE) (Eq. 1) is derived from Maxwell's equations, and describes the spatio-temporal radiance (L) in a material⁴⁸.

$$\begin{aligned} \frac{1}{v} \frac{\partial L(\mathbf{r}, \hat{\boldsymbol{\Omega}}, t)}{\partial t} + \hat{\boldsymbol{\Omega}} \cdot \nabla L(\mathbf{r}, \hat{\boldsymbol{\Omega}}, t) \\ = -\mu_t L(\mathbf{r}, \hat{\boldsymbol{\Omega}}, t) + \mu_s \int_{4\pi} L(\mathbf{r}, \hat{\boldsymbol{\Omega}}', t) p(\mathbf{r}, \hat{\boldsymbol{\Omega}}' \rightarrow \hat{\boldsymbol{\Omega}}) d\hat{\boldsymbol{\Omega}}' + Q(\mathbf{r}, \hat{\boldsymbol{\Omega}}, t) \end{aligned} \quad (1)$$

There is no analytic solution to the RTE, but analytic approximations exist with valid assumptions about the material in question^{48,49}. For example, the diffusion approximation is used for larger scales, assuming the material scatters light at a higher rate than it absorbs it⁴⁸. Fine details on the directional dependence of the radiance are lost, but those details are not often a concern when looking at the radiance on a larger scale. Stochastic solutions to the RTE, most commonly Monte Carlo simulations, use a high number of deterministic scattering and absorption events to approximate the tissue radiance. Monte Carlo modeling is discussed in more detail in section 2.4. Here, we discuss the different light-matter interactions which contribute to the overall radiance within a material.

2.3.1 Light absorption

Light absorption occurs when a photon or wave is incident on a particle or molecule, and the energy of the photon is wholly transferred to that particle. As described by Beer's Law in (Eq.2),

$$I = I_0 e^{-\mu_a l} \quad (2)$$

if an absorbing medium is illuminated with a collimated beam, the intensity of transmitted light is related to the intensity of the initial beam through a decaying exponential function (Figure 3). The exponential term relates the path length (l) of the light through the medium and the absorption coefficient (μ_a), a medium-dependent and wavelength dependent term that describes the probability of a photon being absorbed. In a medium with multiple populations of absorbers, the total absorption coefficient is a weighted sum of the coefficients of each absorbing particle (Eq. 3)⁵⁰.

$$\mu_a = \sum_{i=1}^n c_i \mu_{a,i} \quad (3)$$

The optical imaging window is ideal for biological and biomedical imaging due to the low absorption of water within this spectral region. The primary absorbers in biological tissue within this range are melanin and oxy- and deoxy-hemoglobin. The absorption of all of these decrease in the NIR compared to visible, making the NIR even more favorable for bio-optical imaging^{50, 51}.

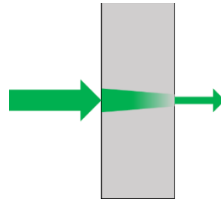


Figure 3. Optical attenuation through an absorbing sample follows an exponential decay.

2.3.1.1 Fluorescence

Fluorescence is a phenomenon stemming from an absorption event of a specific energy. If a photon incident on a molecule has the appropriate energy, the absorbing molecule can undergo an electronic transition upon absorbing the photon energy. As with most absorption events, the molecule will experience some non-radiative decay—motion, heat, vibrational relaxation—in transitioning back to its ground state. However, upon reaching the lowest vibrational state in its elevated electronic state, the molecule may undergo radiative decay. This releases a photon with energy equivalent to the remaining energy differential. The light emitted from a fluorescent molecule is incoherent, isotropic, and always a lower energy than the excitation energy (Figure 4)⁵¹.

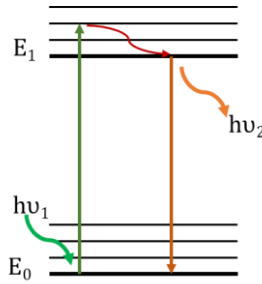


Figure 4. Linear excitation and fluorescence. A photon with sufficient energy to increase a molecule's energy state can be absorbed by that molecule, resulting in an electronic transition (green arrows). The molecule undergoes non-radiative vibrational relaxation (red arrow) to the lowest vibrational state within its elevated electronic state. The molecule can then emit a photon through radiative decay (orange arrows), returning to its ground electronic state.

Biological tissues have characteristic tissue autofluorescence (TAF), a fluorescence signal produced by molecules naturally occurring in the organism. TAF molecules in humans and animals include collagen, keratin, metabolic cofactors NADH and FAD, melanin, and others⁵². These molecules have stronger fluorescence at lower wavelengths, and can contribute significant background to *in vivo* imaging systems in which they are not target fluorophores. For example, optical sensing of biological phenomena can be accomplished through detecting the fluorescence of an exogenous fluorophore, and spectral overlap with resident TAF molecules will lower sensitivity to that molecular marker⁴⁵.

2.3.2 Optical scattering

Rather than transferring energy to a material or molecule it is incident upon, an EM wave can experience an elastic interaction with the media, resulting in a change of direction of the total energy of the wave. In a truly scattering medium, no energy is lost to the material, but redirected depending on the size and refractive index of the scattering particles in the medium (Figure 5). The likelihood of a photon hitting a scatterer over a unit distance is known as the scattering

coefficient (μ_s). Similarly, the mean free path (MFP) is the inverse of μ_s and represents the average distance a photon will travel between scattering events^{47, 50, 51, 53}. As with absorption, an overall scattering coefficient can be calculated from multiple populations of scattering particles, each having its own concentration-dependent weight in the summation of scattering coefficients (Eq. 4).

$$\mu_s = \sum_{i=0}^n c_i \mu_{s,i} \quad (4)$$

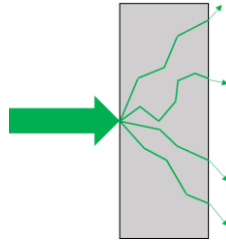


Figure 5. Optical attenuation through a scattering sample. Light incident on a particle is redirected rather than absorbed.

Unlike absorption, scattering is not fully described by the density of scatterers within the media. A photon will continue moving after encountering a scatterer, and the directionality of that continued motion is defined by the phase function. The phase function varies for each particle, and describes the probability of a photon to continue travel at a different angle after a scattering event. Most particles yield a scattering distribution that is not isotropic. The degree of this anisotropy is described by the anisotropy factor (g)⁵⁰. This factor is the average cosine of the scattering angle of a photon incident on a particle with values spanning -1 to 1. A particle which yields isotropic scattering will have a $g = 0$, while values of -1 and 1 correspond to complete backscattering and forward scattering, respectively. Most biological tissues have a g -value between 0.7-0.95, meaning that a given scattering event will likely be forward biased.

2.3.2.1 Henyey-Greenstein phase function

Tissue scattering is well-approximated by the Henyey-Greenstein phase function (Eq.5)⁵¹.

$$p(\theta) = \frac{1-g^2}{4\pi[1+g^2-2g(\cos\theta)]^{3/2}} \quad (5)$$

This function is the relation between g and the scattering distribution, and fully describes the probability of a photon being scattered at a given angle, θ . The phase function and g , just like μ_a and μ_s , are wavelength dependent, and can be calculated or estimated based on particle size, particle shape, medium refractive index, and particle refractive index. The scattering coefficient and anisotropy factor can be combined into the reduced scattering coefficient (μ_s') to give a spatial average of scattered light (Eq. 6).

$$\mu_s' = \mu_s(1 - g) \quad (6)$$

2.3.2.2 Rayleigh and Mie Scattering

Light scattering in biological tissue is best approximated using to populations of scattering particles, Rayleigh and Mie scatterers. Both theories model optical scatterers as spherical particles that redirect the energy of an incident photon or wave. Rayleigh scattering is an elastic scattering event that occurs when the scattering particle is much smaller than the wavelength of light. The intensity of scattered light in the Rayleigh model of scattering is related to the wavelength through a λ^{-4} (Eq. 7), meaning higher energy light is preferentially scattered⁴⁷.

$$I = I_0 \frac{8\pi^4 \alpha^2 (1 + \cos^2 \theta)}{\lambda^4 R^2} \quad (7)$$

In this equation, α is the molecular polarizability, which is related to refractive index, and R is the distance from the scatterer. Rayleigh scattering is also characterized by a fairly isotropic distribution of scattering angles, with equal likelihood of forward and back scatter.

Mie scattering is described by the Mie solution to Maxwell's equations, an infinite converging series of Legendre polynomials. The Mie equations fully described the EM components of the incident, internal, and scattered waves, for spherical particles of any size. At small particle sizes, Mie theory converges to Rayleigh scattering⁵³. However, as particle size approaches the wavelength of incident light, the Rayleigh scattering model begins to fall apart, and the full Mie model is necessary to accurately predict light scattering. Mie theory calculates the coefficients a_n and b_n (Eq. 8-9) using the relative refractive index, $m = n_{par}/n_{med}$, and spherical Bessel functions of the first (j_n) and third (h_n) kind to fully describe the amplitude of the scattered field⁴⁷.

$$a_n = \frac{m^2 j_n(mx)[x j_n(x)]' - j_n(mx)[x j_n(mx)]'}{m^2 j_n(mx)[x h_n^{(1)}(x)]' - h_n^{(1)}(mx)[x j_n(mx)]'} \quad (8)$$

$$b_n = \frac{j_n(mx)[x j_n(x)]' - j_n(mx)[x j_n(mx)]'}{j_n(mx)[x h_n^{(1)}(x)]' - h_n^{(1)}(mx)[x j_n(mx)]'} \quad (9)$$

These coefficients are also used to calculate the scattering efficiency of the particle (Eq. 10), a value which conceptually relates the geometrical cross section of the particle to the scattering cross-section (Eq.11). The scattering cross-section is directly related to μ_s , through the particle density in the medium, ρ_s , (Eq. 12) therefore deriving material-level scattering properties based on the incidence of and EM wave on a single spherical particle^{47, 53}.

$$Q_{sca} = \frac{2}{x^2} \sum_{n=1}^{\infty} (2n+1) (|a_n|^2 + |b_n|^2) \quad (10)$$

$$\sigma_s = \pi r^2 Q_{sca} \quad (11)$$

$$\mu_s = \sigma_s \rho_s \quad (12)$$

The overall scattering coefficient of biological tissue can be estimated by (Eq. 13):

$$\mu_{s,total} = A \left[f_{Ray} \left(\frac{\lambda}{\lambda_0} \right)^{-4} + (1 - f_{Ray}) \left(\frac{\lambda}{\lambda_0} \right)^{-b_{Mie}} \right] \quad (13)$$

where λ_0 is a reference wavelength, f_{Ray} is the fraction of scatterers in the Rayleigh regime, and A is the scattering coefficient at the reference wavelength, and b_{Mie} is the scattering power of the Mie particles present⁵⁰.

2.3.3 Measurement of optical properties

Absorption and scattering properties of biological tissues can be estimated through mathematical models if the components of the tissue are known. However, given the complexity and variability of biological tissues, directly probing the optical properties of the material may be more accurate. One of the most common ways to determine μ_a and μ_s' of a material is through integrating sphere (IS) measurements and inverse adding-doubling (IAD) convergence algorithms^{51, 54}. Because these measurements are indirect and IAD is a stochastic convergence algorithm, the acceptable error between the measured and expected optical properties is relatively high, sometimes up to 15%⁵⁵. Despite this high error, this is still a widely accepted method for measurement of optical properties of turbid biological tissue.

2.3.3.1 Integrating sphere measurements

Absorption and scattering coefficients of turbid media cannot be directly measured, so they must be inferred from other measurements. Using an integrating sphere, diffuse reflectance (R) and transmittance (T) of thin samples are directly measured. In the measurement setup (Figure 6), a collimated broadband light source is launched at the entry port of the integrating sphere. A detector is connected to another port on the integrating sphere, offset from the light path. For transmission measurements, the sample is placed at the entry port, and the exit port of the sphere is capped. For reflectance measurements, the sample is placed at the exit port of the sphere, so that any diffusely reflected light can be measured. Calibration measurements including dark spectra and reflectance from standard(s) and the sphere are also collected to calculate the R

and T values of the sample. Assuming a sample thin enough to minimize multiply scattered photons, a these R and T values and sample thickness can be used as inputs into IAD to estimate optical coefficients.

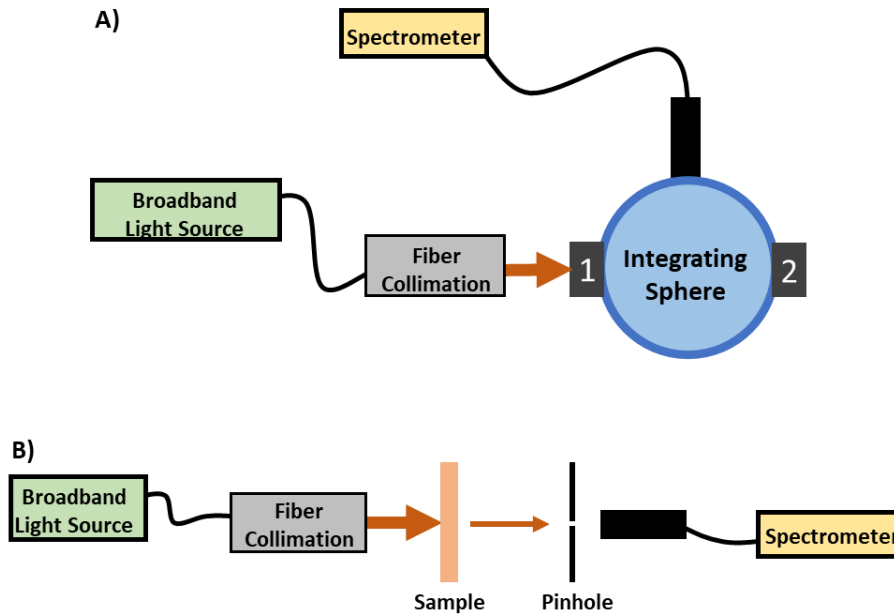


Figure 6. System for measuring sample reflectance, transmittance, and unscattered transmittance.

A) The integrating sphere system used for reflectance and transmittance measurements consists of a collimated light source launched into an integrating sphere. Scattered light is collected with a spectrometer connected to an offset port. Reflectance is measured with the sample at port 2 with port 1 open. Transmittance is measured with the sample at port 1 and port 2 closed. B) The unscattered transmittance pathway consists of the same collimated source incident on the sample, then a pinhole and the detector. This pathway allows for angular characterization of scattering.

2.3.3.2 Inverse adding-doubling

IAD is the inverse process of adding-doubling, a forward modeling method which simplified the 6-dimensional RTE to a one-dimensional problem⁵¹. By taking a very thin sample and summing over all angles, the radiance at a single point is assumed to be a sum of two terms: the transmitted radiance from a neighboring thin slice, and the radiance reflected from a

neighboring point off the boundary. Each radiance term is calculated based off of the absorption and scattering coefficients of the material. “Doubling” takes the radiance from this thin slice and propagates it to an arbitrarily thick sample. “Adding” propagates the radiance through different thin slabs of varying optical properties. This forward adding-doubling method calculates the R and T values of a sample of a known thickness. Inverse adding-doubling simply does the reverse. The software iteratively estimates μ_a and μ_s' , calculates R and T based on the forward model, and re-estimates μ_a and μ_s' based on the error between measured the measured R and T values and the R and T values calculated from the most recent iteration of the forward model.

2.4 Monte Carlo Modeling

Monte Carlo simulations of light transport have a well-defined general structure and flow (Figure 7). The propagation of each photon through the tissue is determined by a decision tree and a random number generator. A photon is launched into the tissue, and propagated at a step size calculated based on the material optical properties. If the photon hits a boundary over this transition, the photon is transmitted or reflected accordingly. If it does not hit a boundary, the photon deposits energy in the tissue at that point, and/or is re-directed (scattered) based on the optical properties of the material in that region. The photon undergoes a roulette step based on the random number generator, and if the photon survives, it is propagated in the same manner until the photon no longer survives. As the number of photons launched approaches infinity, the error between the actual and modeled radiance will converge to zero^{53, 56}.

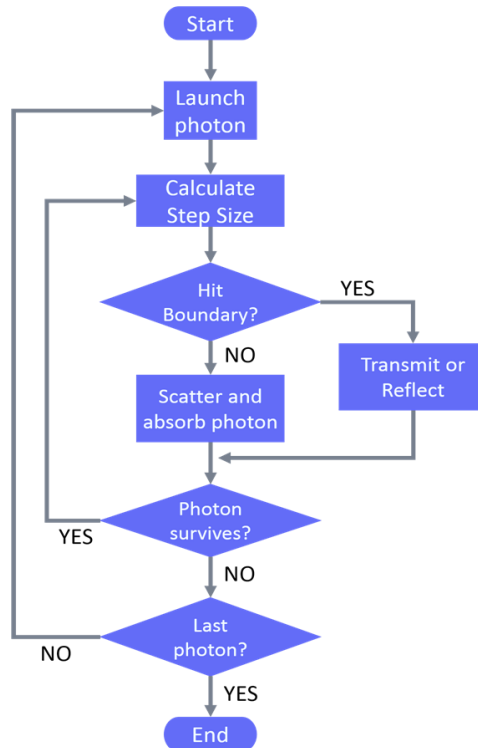


Figure 7. Flowchart of the decision process of Monte Carlo models of radiative transport. This decision process continues for the lifespan of a single photon. It is repeated for every photon launched in the model.

Stochastic optical simulations such as Monte Carlo models can predict both the fluence of light within the tissue and the diffuse reflectance which travels back to an external detector, making them useful for both optically radiative therapeutic treatments and optical diagnostic methods. A variety of these stochastic models have been developed to describe the complex interaction of light and tissue. Time-resolved Monte Carlo simulations have helped to describe the fluorescence lifetime shift in the endogenous fluorophores present in fluorescence lifetime imaging. Multi-layer Monte Carlo (MCML) has frequently been used to analyze the diffuse reflectance of dysplastic, precancerous and cancerous epithelial tissues for optical diagnosis of cancer⁵⁶⁻⁵⁹. Complex geometry MCML models have incorporated cylindrical structures

representative of capillaries to find the necessary dose to rupture blood vessel walls in the elimination of port wine stain birthmarks^{60, 61}.

2.5 Optical tissue phantoms

Tissue-simulating phantoms have historically played a large part in the development of new optical techniques for biological and medical imaging. As a model of the optical environment of a biological sample or subject, optical tissue phantoms are used for simulation validation, device development, calibration, and quality control. Commercial phantoms with highly controlled properties are available, but for many research labs developing novel system, it is necessary to have a custom standard or model to characterize and test the system during and post-development. Depending on the purpose, the phantom must have one or all of the following characteristics: 1) mimic a specific biology or physiology, 2) highly controlled properties including optical, mechanical, and geometric, 3) long-term stability, and 4) reproducibility⁶².

As new optical imaging techniques emerge or are combined into multi-modality systems, new phantoms are developed for appropriate testing and calibration of these systems. Many optical imaging systems are gaining prevalence in both preclinical and clinical settings, and it is imperative to have tools to ensure the proper performance of these systems. Phantoms and standards often serve as inter-device calibration tools, ensuring optimal performance of the imaging system. These phantoms need to be long-lasting, consistent, and stable for continued, reliable use. Other phantoms are used for device characterization and optimization, and may not need long-term stability, but must be more structurally complex, or even modular to fully define the capabilities of a biological imaging system. While some phantoms have been developed to test multiple types of optical systems, it is more common for a phantom to be modality-specific, with many also being specific to the sample or physiological system to be imaged. Both the

modality and sample will inform the design of the optical phantom. A variety of techniques have emerged to create phantoms and standards for optical imaging.

3. OPTICAL PHANTOM DESIGN AND FABRICATION

3.1 *Optical phantoms as simulation validation*

Tissue phantoms are used widely for system characterization and calibration of optical imaging and spectroscopy instruments, including multimodality systems incorporating ultrasound or nuclear modalities⁶³⁻⁶⁶. Phantoms provide a controlled optical environment for system characterization and quality control of multiple biological imaging techniques. Tissue-mimicking phantoms are useful tools in predicting system performance and optimizing system design for the physiological task at hand; for example, to predict the probing depth of spectroscopic probes for assessing tumor margins⁶⁷. Optical properties and structural design of the phantoms can be tuned to mimic the specific physiological environment in which the instrument will be used, therefore allowing for both feasibility studies and verification of system performance^{65, 68, 69}. Verification of imaging system performance with realistic optical phantoms prior to entering pre-clinical or clinical trials reduces risk of malfunction or acquisition of unusable data during *in vivo* studies. The reproducibility and stability of optical phantoms make them customizable calibration standards for optical techniques to monitor intra- and inter-instrument variability, particularly in multicenter clinical trials with different instruments, operators, and environmental conditions^{70, 71}.

Tissue-mimicking phantoms also serve as tunable and reproducible physical models for validation of theoretical optical models. Simulations aid in the design and optimization of *in vivo* optical instruments, while reducing the need for animal experiments^{72, 73}. The development and

* Reprinted with permission from “Fabrication and Characterization of Optical Tissue Phantoms Containing Macrostructure” by Durkee, Madeleine S., Nash, Landon D., Nooshabadi, Fatemeh, Cirillo, Jeffrey D., Maitland, Duncan J., Maitland, Kristen C., 2018. *Journal of Visualized Experiments*, 132, e57031, Copyright 2018 by MyJoVE Corps.

validation of optical simulations to accurately represent the *in vivo* environment can be encumbered by the complexity of the tissue structure, the biochemical content, and the location of the target or tissue within the body. Variability between subjects makes validation of theoretical models challenging using animal or human measurements. Polymer optical tissue phantoms allow for validation of theoretical models by supplying a known and reproducible optical environment in which to study photon migration^{62, 74-76}.

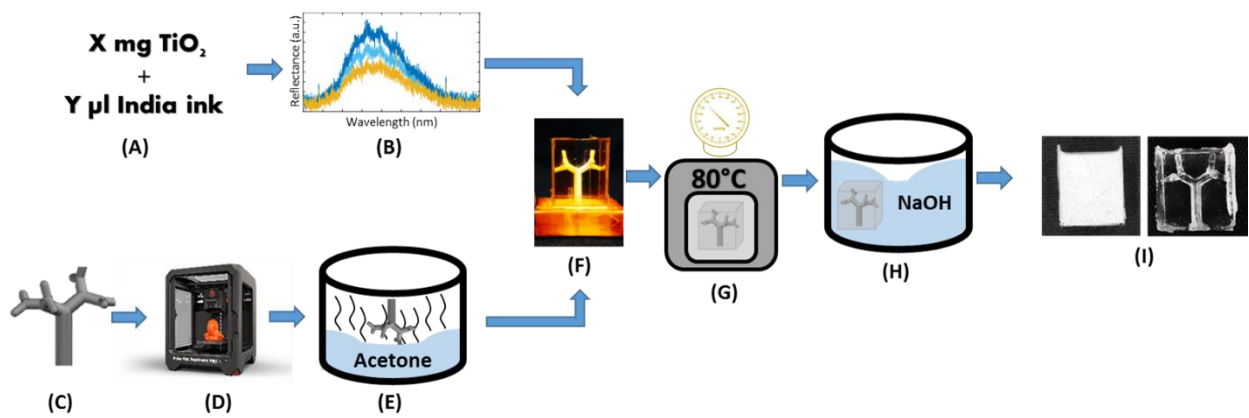


Figure 8. Flow diagram of fabrication of optical tissue phantom. (A) Determine optimal recipe for target optical properties of tissue of interest. (B) Verify recipe. (C) Design internal structure. (D) Print internal structure using dissolvable material. (E) Vapor polish printed part to smooth surface. (F) Mix polymer and optical particles, and pour into heat-resistant mold. (G) Degas and cure polydimethylsiloxane (PDMS). (H) Dissolve printed part to create internal void. (I) verify phantom geometry and optical properties.

For the purpose of system calibration, solid optical phantoms may consist of a single homogeneous slab of cured polymer with the optical scattering, absorption, or fluorescence tuned for the wavelengths of interest. Layered polymer phantoms are frequently used to mimic the depth variance of the tissue optical properties in epithelial tissue models^{77, 78}. These phantom structures are sufficient for epithelial imaging and modeling, because the tissue structure is fairly homogeneous through each layer. However, larger scale and more complex structures affect radiative transport in other organs. Methods to create more complex phantoms have been

developed to simulate the optical environment of subcutaneous blood vessels^{79, 80} and even whole organs, such as the bladder⁸¹. Modeling light transport in the lungs provides a unique problem due to the branching structure of the air-tissue interface; a solid phantom would not likely replicate radiative transport in the organ accurately⁸². To describe a method for incorporating complex structure into an optical phantom, we describe a method to create an internal, reproducible fractal tree void that represents the three-dimensional (3D) macroscopic structure of the airway (Figure 8c).

3.2 Material optical properties

The material matrix for the mouse lung tissue phantoms was designed to simulate measured optical properties of excised healthy and inflamed murine lung tissue at 535 nm and 730 nm (Tables 2-3). These wavelengths of interest are the excitation wavelengths for tdTomato fluorescent protein used in recombinant reporter strains of mycobacteria and the NIR fluorescent bacteria-sensing probe used in the mouse model of infection^{45, 83}. Reflectance (R) and transmittance (T) values of *ex vivo* mouse lung tissue were obtained using an integrating sphere. Inverse adding-doubling (IAD) software was used to convert these R and T values into absorption and scattering coefficients. Use of animals was approved by the Institutional Animal Care and Use Committee (IACUC) at Texas A&M University.

Table 2. Optical properties of healthy and inflamed mouse lung tissue compared to the corresponding phantom recipes for properties at 535 nm.

535 nm	Absorption Coefficient (cm⁻¹)	Reduced Scattering Coefficient (cm⁻¹)
Healthy mouse lung tissue	2.05 ± 0.58	52.69 ± 7.83
Healthy phantom (2 mg TiO ₂ + 3.5 μL India ink)	1.96 ± 0.699	49.66 ± 0.12
Inflamed mouse lung tissue	5.49 ± 1.32	38.94 ± 9.68
Inflamed phantom (1 mg TiO ₂ + 10 μL India ink)	4.34 ± 0.873	39.56 ± 5.02

Table 3. Optical properties of healthy and inflamed mouse lung tissue compared to the corresponding phantom recipes for properties at 730 nm.

730 nm	Absorption Coefficient (cm^{-1})	Reduced Scattering Coefficient (cm^{-1})
Healthy mouse lung tissue	0.71 ± 0.16	58.44 ± 5.14
Healthy phantom (2 mg TiO_2 + 1 μL India ink)	0.62 ± 0.48	51.18 ± 11.20
Inflamed mouse lung tissue	1.01 ± 0.55	34.84 ± 8.19
Inflamed phantom (2 mg TiO_2 + 2.5 μL India ink)	1.44 ± 0.26	34.18 ± 5.06

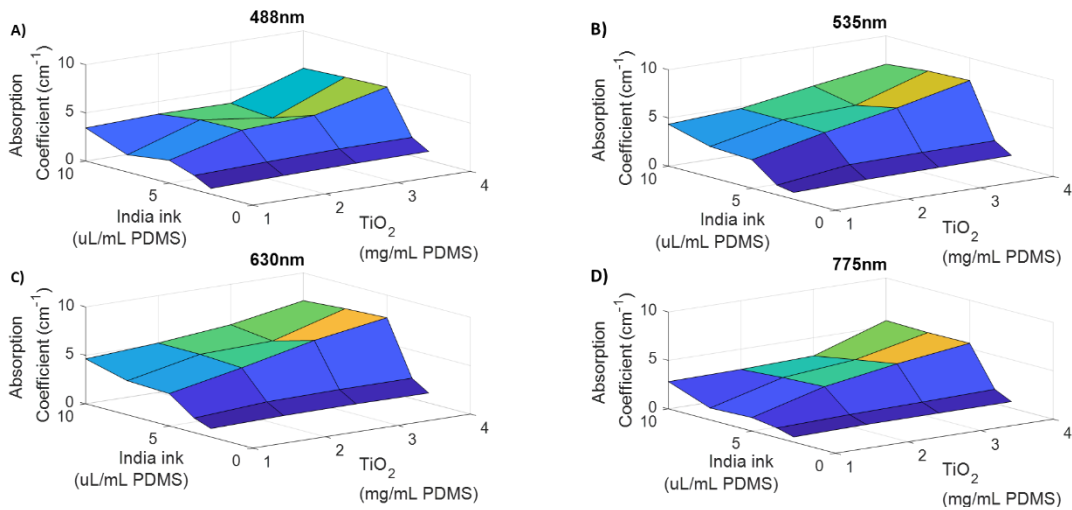


Figure 9. Trends in absorption coefficient for India ink and TiO_2 concentration. Absorption coefficients are shown for a range of India ink and titanium dioxide concentrations at 488 nm (A), 535 nm (B), 630 nm (C), and 775 nm (D). Absorption is low for low concentrations for both particles, and generally increases with concentrations of each particles. A plateau is reached between 5-7.5 μL India ink per mL PDMS. The rate of increase depends on the concentration of the other particle and the wavelength.

Polydimethylsiloxane (PDMS, Sylgard, Dow Corning) was used as the base material for these phantoms due to a similar refractive index to biological tissue⁵⁰. Titanium dioxide (TiO_2) and India ink were used as scattering and absorbing particles, respectively. To optimize the optical properties of material to model the four desired tissue states (healthy and inflamed tissue

at 535 nm and 730 nm), an array of phantoms were made with concentrations of TiO₂ ranging from 1-8 mg/mL PDMS and concentrations of India ink ranging from 2.5-10 μ L/mL PDMS.

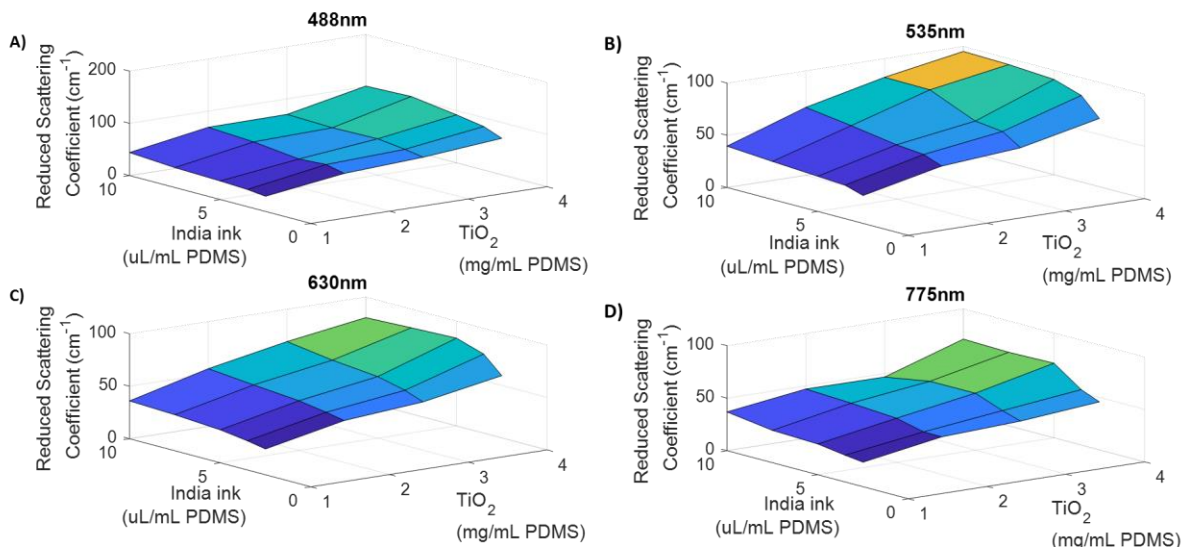


Figure 10. Trends in reduced scattering coefficient for India ink and TiO₂ concentration. Reduced scattering coefficients are shown for a range of India ink and titanium dioxide concentrations at 488 nm (A), 535 nm (B), 630 nm (C), and 775 nm (D). The reduced scattering coefficient is low for low concentrations for both particles, and generally increases with concentrations of each. Like absorption, the rate of increase depends on the concentration of the other particle and the wavelength.

Figures 9-10 show the resulting absorption and reduced scattering coefficients for these recipes. The dependence of absorption and scattering on particle concentration are summarized in Figure 11. Trends in absorption coefficient and reduced scattering coefficient for phantoms with a constant concentration of TiO₂ (scattering particle) (Figure 11a, b) and a constant concentration of India ink (absorbing particle) (Figure 11c, d) demonstrate the relation of optical properties to both particles. To ensure reproducibility of these optical properties, proper mixing technique must be used. Settling and ribboning of TiO₂ particles will cause a shift in the

scattering coefficient of the cured phantom (Figure 12). India ink staining the mixing container will also reduce the absorption coefficient. Look-up tables for phantom recipes corresponding physiologically relevant values of absorption and scattering coefficients for 488 nm, 535 nm, 630 nm, and 775nm light can be used to help achieve the desired optical properties at the spectral region of interest (Tables 4-7).

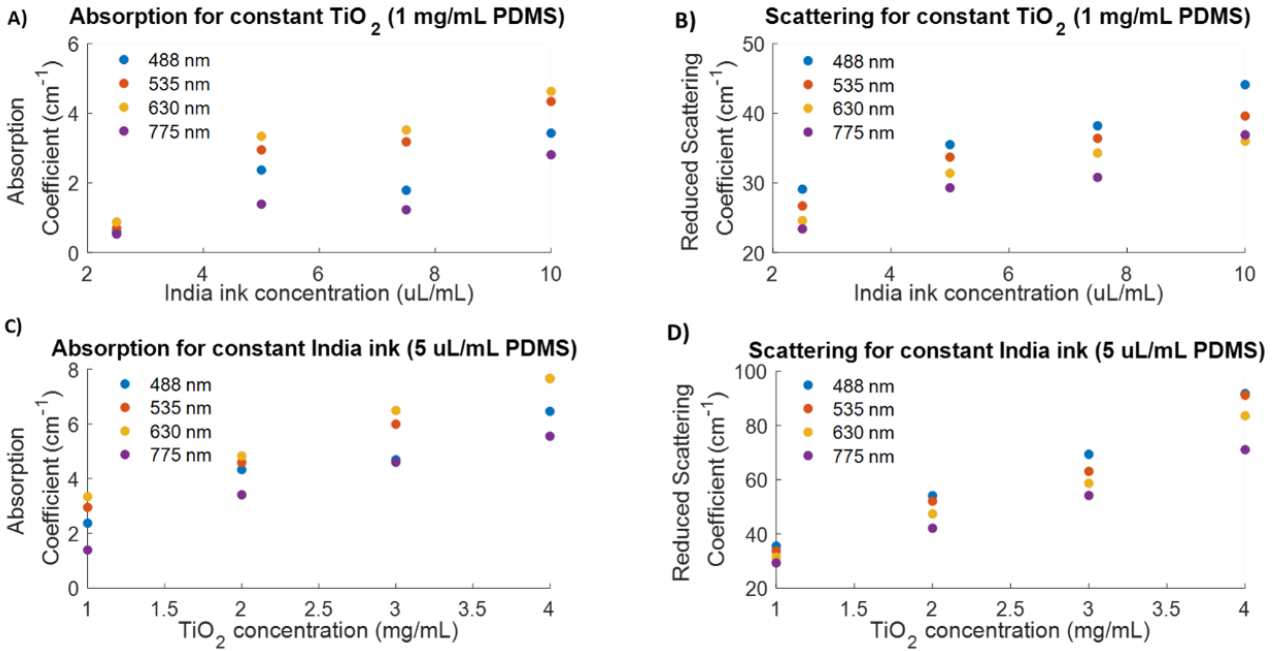


Figure 11. Interdependency of optical properties on India ink and TiO₂ concentration. Absorption coefficients and reduced scattering coefficients are shown for recipes with a constant TiO₂ concentration of 1 mg/mL PDMS (A, B) and constant India ink concentration of 5 uL/mL PDMS (C, D). Panel (B) shows that scattering coefficient will change with a constant TiO₂ concentration when India ink concentration is varied, and panel (C) shows that absorption coefficient will change for a constant India ink concentration when TiO₂ is varied.

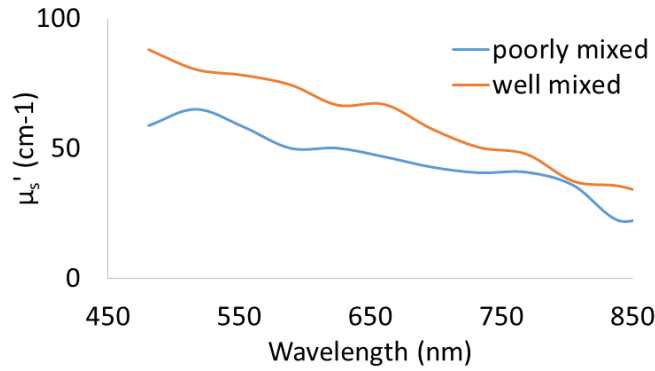


Figure 12. Mixing effects on optical scattering. Improper mixing of the uncured polymer and optical particles can result in a shift in the optical properties. The poorly mixed phantom represented in this figure showed settling of TiO₂ particles prior to curing.

Table 4. Look-up table for phantom recipes at 488 nm base on experimental measurements.

Greyed out recipes do not follow the expected trend.

488 nm		$\mu_s' (cm^{-1})$									
		0.5	1	1.5	2	2.5	3	3.5	4	4.5	6.5
$\mu_s' (cm^{-1})$	30	1 mg TiO ₂ + 2.5 uL India ink	---	1.5 mg TiO ₂ + 5uL India ink	---	---	---	---	---	---	---
	40	---	---	---	1 mg TiO ₂ + 7.5 uL India ink	1 mg TiO ₂ + 5 uL India ink	---	1 mg TiO ₂ + 10 uL India ink	---	---	---
	50	---	2 mg TiO ₂ + 2.5 uL India ink	---	---	---	---	---	2 mg TiO ₂ + 5 uL India ink	---	---
	60	---	---	2 mg TiO ₂ + 3.5 uL India ink	---	---	3 mg TiO ₂ + 7.5 uL India ink	---	---	3 mg TiO ₂ + 5 uL India ink	1.5 mg TiO ₂ + 12 uL India ink
	70	---	4 mg TiO ₂ + 2.5 uL India ink	---	---	---	---	---	---	---	---
	80	---	---	---	4 mg TiO ₂ + 3.5 uL India ink	---	---	---	---	---	---
	90	---	---	---	---	---	---	---	---	---	4 mg TiO ₂ + 5 uL India ink

Table 5. Look-up table for phantom recipes at 535 nm base on experimental measurements.

535 nm		μ_a (cm^{-1})						
		0.5	1	2	3	4.5	6	7
μ_s (cm^{-1})	30	1 mg TiO ₂ + 2.5 uL	---	---	1 mg TiO ₂ + 5 uL India	---	---	---
	40	---	2 mg TiO ₂ + 2.5 uL India ink	---	1 mg TiO ₂ + 7.5 uL India ink	1 mg TiO ₂ + 10 uL India ink	---	---
	50	---	---	2 mg TiO ₂ + 3.5 uL India ink	---	2 mg TiO ₂ + 5 uL India ink	---	---
	70	---	4 mg TiO ₂ + 2.5 uL India ink	---	---	3 mg TiO ₂ + 5 uL India ink	---	---
	80	---	---	4 mg TiO ₂ + 3.5 uL India ink	---	3 mg TiO ₂ + 7.5 uL India ink	3 mg TiO ₂ + 10 uL India ink	---
	90	---	---	---	---	---	---	4 mg TiO ₂ + 10 uL India ink

Table 6. Look-up table for phantom recipes at 630 nm base on experimental measurements.

630 nm		μ_a (cm^{-1})							
		1	2	3.5	4.5	5	6	6.5	7
μ_s (cm^{-1})	20	1 mg TiO ₂ + 2.5 uL India ink	---	---	---	---	---	---	---
	30	---	1.5 mg TiO ₂ + 5 uL India ink	1 mg TiO ₂ + 7.5 uL India ink	---	---	---	---	---
	40	2 mg TiO ₂ + 2.5 uL India ink	2 mg TiO ₂ + 3.5 uL India ink	---	1 mg TiO ₂ + 10 uL India ink	---	---	---	---
	50	---	---	---	---	2 mg TiO ₂ + 5 uL India ink	---	---	---
	60	4 mg TiO ₂ + 2.5 uL India ink	---	---	---	3 mg TiO ₂ + 7.5 uL India ink	---	3 mg TiO ₂ + 5 uL India ink	2 mg TiO ₂ + 10 uL India ink
	70	---	---	---	---	---	3 mg TiO ₂ + 10 uL India ink	---	---
	80	---	4 mg TiO ₂ + 3.5 uL India ink	---	---	---	---	---	4 mg TiO ₂ + 10 uL India ink

Table 7. Look-up table for phantom recipes at 775 nm base on experimental measurements.

775 nm		μ_a (cm ⁻¹)							
		0.5	1	1.5	3	3.5	4.5	5.5	6
μ_s' (cm ⁻¹)	20	1 mg TiO ₂ + 2.5 uL India ink	---	---	---	---	---	---	---
	30	---	1 mg TiO ₂ + 7.5 uL India ink	1 mg TiO ₂ + 5 uL India ink	---	---	---	---	
	40	2 mg TiO ₂ + 2.5 uL India ink	2 mg TiO ₂ + 3.5 uL India ink	---	1 mg TiO ₂ + 10 uL India ink	2 mg TiO ₂ + 5 uL India ink	---	---	
	50	4 mg TiO ₂ + 2.5 uL India ink	---	4 mg TiO ₂ + 3.5 uL India ink	3 mg TiO ₂ + 10 uL India ink	3 mg TiO ₂ + 7.5 uL India ink	3 mg TiO ₂ + 5 uL India ink	1 mg TiO ₂ + 15 uL India ink	
	70	---	---	---	---	---	---	4 mg TiO ₂ + 5 uL India ink	4 mg TiO ₂ + 10 uL India ink

3.3 Advanced methods for complex, multi-layer structure

The first generation of complex phantoms was a rectangular phantom with a mock airway, fractal tree void (Figure 8c). This void was obtained by 3D printing a fractal tree in a base-soluble material and securing it to the base of the polymer mold (Figure 8f). The 3D printed structure was vapor polished to create a smooth internal surface inside the phantom (Figure 8e). After pouring the PDMS mixture into this mold, the uncured phantom was degassed to remove unwanted air bubbles, then cured at 80 °C for 2 hours. Figure 13 shows a comparison of light scattering from a PDMS phantom (with no TiO₂ or India ink) that was not degassed or vapor polished (Figure 13a, c), and a phantom that had a vapor polished internal part and was degassed (Figure 13b, c). The phantoms were imaged using illumination from an external white light source (Figure 13a, b) and with an internal microendoscope source at 535 nm (Figure 13c, d).

Vapor polishing and degassing minimize the presence of irreproducible scatterers, including surface roughness (Figure 13c, inset 2) and bubbles (Figure 13c, inset 1). Degassing is particularly important, because air bubble location is random and unpredictable. Furthermore, air bubbles are obscured once TiO₂ particles are incorporated (not shown in Figure 13), making the phantom optically opaque. Therefore, unseen bubbles may undermine the phantom material's representation of tissue optical properties.

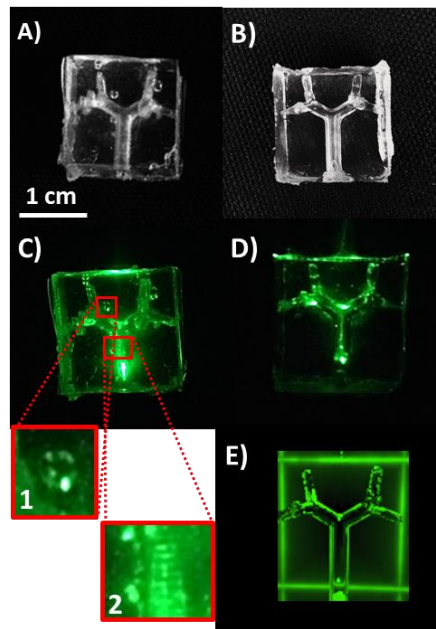


Figure 13. Representative airway phantoms with low scattering coefficient material to illustrate successful and suboptimal fabrication. Vapor polishing and degassing are integral steps in producing a phantom that has minimal uncharacterized scattering elements. A-B) White light images of phantoms without vapor polishing and degassing (A) and with vapor polishing and degassing (B). C-D) Phantoms from A-B are illuminated with 535 nm light. Insets from (C) are shown to depict scattering effects of 1) air bubbles and 2) a rough 3D printed surface. E) Rendering of an optical simulation based on the computer aided design (CAD) model used for the phantom fabrication.

3.4 Geometry verification and optical imaging

For optically turbid phantoms with an internal void, geometry verification must be performed by means other than visual inspection. Methods for geometry verification of optical imaging of turbid phantoms is described for the preliminary block phantom with a fractal tree void. The vapor-polished 3D printed part was measured with calipers at the base and at the distal branches, and dimensions are compared to the 3D solid model in Table 8. Following fabrication of the polymer phantom, the phantom was imaged using a micro-CT imaging system. Using the 3D dataset, dimensions of the internal void at the base and distal branches were measured for comparison (Table 8). Using micro-CT for geometry verification, a small amount of residual material was found within the airway void. Additionally, a segmentation of this same CT scan reveals a small air bubble next to the branching structure (Figure 14). During fabrication, optically clear phantoms yielded a full dissolution of the material of the internal structure and no air bubbles within the polymer matrix.

Table 8. Effects of vapor polishing on size of 3D printed internal structure. The molded phantom was also measured for airway size using the micro-CT images for validation of internal geometry.

	Base diameter (mm)	Distal branch diameter (mm)
<i>Solid model</i>	2.7	1.38
<i>Vapor polished print</i>	2.56 ± 0.026	1.38 ± 0.141
<i>PDMS mold (measured from CT)</i>	2.55 ± 0.021	1.39 ± 0.055

Verification with micro-CT showed that the optically opaque phantoms may contain small flaws, not otherwise visible in turbid phantoms. The vapor polished tree is slightly smaller at the base because the smoothing of the surface by the acetone vapor causes the surface of the plastic to flow. With the 3D printed part suspended by the base, the surface flows towards the distal branches, causing a small change in dimension of the part. There is a trade-off between

surface smoothness and maintaining part size. A longer vapor polish will result in a smoother surface, but will cause more material to flow, resulting in altered dimensions. For the fractal geometry shown here, polishing the internal structure yielded a decrease in average surface roughness of molded PDMS from 37.4 μm to 7.2 μm .

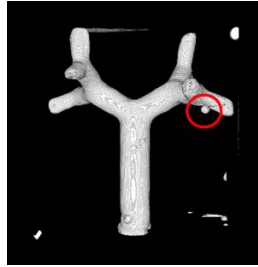


Figure 14. Validation of airway geometry. A segmented micro-computed tomography image of an optically turbid phantom reveals an air bubble near the airway surface.

Phantoms were imaged in a PerkinElmer IVIS Lumina II with an access port for insertion of a microendoscope fiber bundle (Figure 15). The microendoscope was placed into the void within the phantoms from which the printed part had been dissolved. The microendoscope was used for internal illumination at 535 nm and the IVIS illumination pathway was blocked. The placement of the microendoscope is indicated in Figure 15a. The IVIS was used for external collection of signal. Phantoms imaged had the same internal structure as those imaged in Figure 3. With identical internal structures and external dimensions, the difference in optical properties between healthy lung tissue (Figure 15a) and infected lung tissue (Figure 15a) is apparent in the surface irradiance of the phantoms. As these phantoms maintain an appropriate response to a change in optical properties, this method for phantom fabrication can be applied for phantoms used in internal illumination studies.

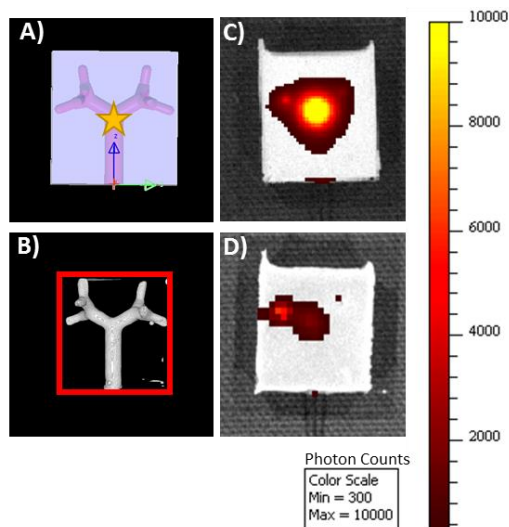


Figure 15. Imaging of phantoms with internal illumination. A computer simulation of the phantom (A) demonstrates the orientation of the internal geometry and source placement (yellow star) for the phantom images in panels (C) and (D). A segmented micro-CT scan of the healthy lung tissue phantom (B) confirms the internal structure is present in the optically opaque phantom. The mock airway is used as a pathway for the endoscope for internal illumination of the optical phantoms at a wavelength of 535 nm. The two phantoms imaged with internal illumination are identical in external shape and internal structure, with material optical properties optimized for healthy (C) and inflamed (D) lung tissue. All images and renderings are on the same scale. Scale bar in panel (C) is 1 cm.

3.5 Full torso and sparse tissue phantom design

The phantoms discussed above are single-layer phantoms with a complex structure dissolved out to mimic the mouse airway. However, the lung is a porous organ with a low tissue density. The porosity of the tissue greatly affects tissue scattering, so an improved physical model of the lung parenchyma would be a polymer foam. Figure 16 shows representative images of PDMS phantoms loaded with glass microbubbles at 30%, 40%, 50%, and 60% volume fractions. The glass layer within these phantoms approximates scattering from the surfactant liquid layer

within the alveoli. Detailed scattering characteristics of this physical model are discussed in chapter 4.

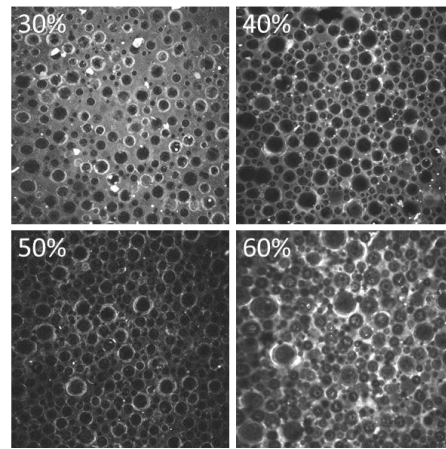


Figure 16. Inflated lung tissue modeled by glass microbubble phantoms. Fluorescence confocal images show an increase in microbubble concentration consistent with the intended recipe.

The final iteration of these phantoms are composed of multiple layers of polymer mixtures representing the optical properties and general anatomy of the mouse torso. The stability of PDMS phantoms should allow these phantoms to serve as validations of the optical model and calibration standards for imaging experiments with intravital illumination. Figure 17 shows the overall design of these phantoms, and the current status of the phantom fabrication. These phantoms consist of a 3D printed, dissolvable airway, a polymer mold of mouse lung tissue with glass microbubbles, and a final outer mold of the bulk tissue surrounding the lung. These phantoms are fabricated with a multi-layer molding process including 3D printing, clamp molding, and pour-over molds.

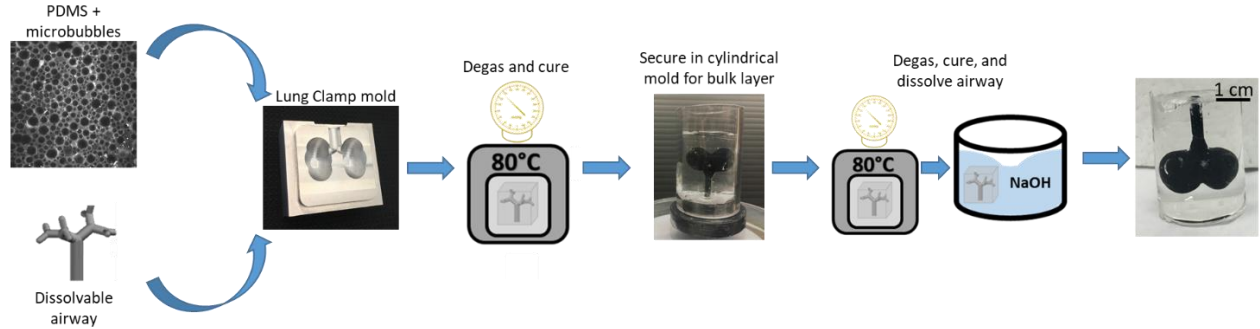


Figure 17. Flowchart of fabrication process for mouse torso phantoms. Uncured PDMS with the optical properties of lung tissue is loaded with microbubbles to represent inflated lung (A). The uncured mixture is placed in a lung-shaped clamp mold (C) with a 3D printed, dissolvable airway (B). The lung mold is degassed and heat cured (D). The cured lung phantom is secured in a cylindrical mold (E) and PDMS representing optical properties of bulk tissue is poured into the mold (shown optically clear for demonstration). This layer is degassed and cured, and the entire phantom is placed in a heated base bath to dissolve the internal airway (F). The final phantom (G) is shown with a clear bulk tissue layer and an absorbing lung layer for visualization.

3.6 Optical phantom stability and tunability

We have demonstrated a method for creating optical phantoms to represent a murine lung with an internal branching structure to simulate the internal air-tissue interface. The optical properties of murine lung tissue are achieved by incorporating unique concentrations of optically scattering and absorbing particles distributed homogeneously within the bulk matrix polymer. These optical properties can be tuned to mimic the physiological values within different spectral ranges of tissues in different states (i.e. healthy versus diseased tissue). The optical properties are dependent on the wavelength of interest, the base material, and the concentrations of the particles within the phantom. However, with multiple particles, the relationship between scattering and absorption is not always intuitive⁸⁴. The rate of increase of absorption is dependent on the concentration of the scattering particle as well as the absorbing particle, and likewise for the rate

of increase of the reduced scattering coefficient. (Figures 9-10). PDMS phantoms have also been shown to maintain their optical properties for up to 1 year^{62, 85}. We have measured a 3-week stability of optical properties within the error of our integrating sphere measurements (< 15%). Storage of these phantoms and standards in a light-tight container can help preserve their optical properties for longer periods of time.

The design of these phantoms is limited by the 3D printed part. The mock airway is designed so that the support material can be pried off, as it is not dissolvable. This can be overcome by moving to a more advanced printer that can either print materials with varying solubility, or a laser sintering printer, that does not need support material. It is also important to note that the lung is inherently a very porous organ because of the distal airways and the alveoli. While that is not represented in this phantom, the optical effects of similar structures have been observed using a Bragg-Nye bubble raft for optical coherence tomography⁸², air bubbles in olive oil⁸⁶, and shaving cream or dish detergent for nuclear magnetic resonance imaging⁸⁷. Creating polymer foams with reproducible characteristics may be able to reconcile this difference between the solid phantoms presented here and the lung microstructure⁸⁸.

The shape of the final phantom can also be customized depending on the application. The rectangular phantom shown here was imaged with internal illumination and used for validation of a computational model of healthy and infected lungs (Figure 15). This design can be updated further to represent the cylindrical torso of the mouse by simply changing the design of the external polymer mold.

While we have detailed here the design of a murine lung and airway phantom, these methods can be modified to fit other organs or animals of interest. The internal structure can be converted to a flow pathway for vascular phantoms, or can be used as a cast for a complex

internal structure with unique optical properties. The overall shape of the phantom can also be tuned to the application, animal, or organ of interest. 3D printing of both internal structures and polymer molds gives freedom to the design process of structured polymer optical phantoms. These are integral tools in simulation validation and calibration of *in vivo* optical imaging techniques, because they can more accurately represent the *in vivo* environment than homogeneous single or multi-layer phantoms.

4. MULTI-LAYER MIE SCATTERING MODEL FOR ALVEOLAR SCATTERING

4.1 Concentric sphere Mie scattering model

Mie scattering theory is based on the propagation of electromagnetic waves in materials with different dielectrics. Traditionally, Mie theory approximates scattering particles as spherical inclusions with a different dielectric constant than the surrounding medium. Many adaptations of Mie theory have since been employed, including approximation of scatterers as ellipsoidal particles to better mimic cellular scattering events⁸⁹, and multi-layer concentric sphere models, the first of which was conceived by Aden and Kerker in 1951⁹⁰. The concentric spheres in this model have variable dielectrics across each layer of the spherical particles (Figure 18), and are commonly used for modeling the enhanced scattering fields by semi-conductor nanoparticles⁹¹⁻⁹³.

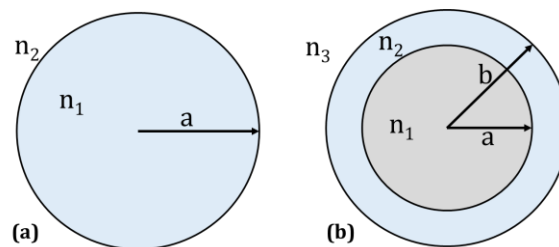


Figure 18. Spherical particles modeled in traditional Mie scattering (a) and in the concentric sphere model (b).

Using the properties of the electromagnetic wave propagation in both the spherical particle and surrounding medium, Mie theory establishes equations for both the transmitted and scattered fields. In radiative transport for biological materials, we are mainly concerned with the scattered electric and magnetic fields⁹⁴. The Mie coefficients a_n and b_n used in these field equations are given above in Equations 8 and 9, where m is the ratio of refractive indices of the particle and medium, and j_n and h_n are spherical Bessel functions of the first and third order,

respectively. Aden and Kerker first extrapolated these equations to a two layer concentric sphere model, where a third set of equations is included to describe the field in the second particle dielectric, or the field within the particle “shell”. Extra terms are added to the original transmitted and scattered fields to account for field interaction with the outer particle layer. The complete Mie coefficients for the scattered field in a concentric Mie model are listed in Equations 14-19, where n_1 is the refractive index of the inner sphere, n_2 is the refractive index of the shell, n_3 is the refractive index of the medium, m_1 is the ratio n_1/n_3 , m_2 is the ratio n_2/n_3 , α is the inner sphere radius, and v is the outer sphere radius (Figure 18).

$$a_n = \frac{\left(\frac{[v j_n(v)]'}{v}\right) A_1 + n_3^2 j_n(v) A_2}{\left(\frac{[v h_n(v)]'}{v}\right) A_1 + n_3^2 h_n(v) A_2} \quad (14)$$

$$b_n = -\frac{j_n(v) A_3 + n_3^2 \left(\frac{[v j_n(v)]'}{v}\right) A_4}{h_n(v) A_3 + n_3^2 \left(\frac{[v h_n(v)]'}{v}\right) A_4} \quad (15)$$

$$A_1 = n_3^2 \left(\frac{[m_1 \alpha j_n(m_1 \alpha)]'}{m_1 \alpha}\right) [j_n(m_2 v) h_n(m_2 \alpha) - j_n(m_2 \alpha) h_n(m_2 v)] + n_1 n_2 j_n(m_1 \alpha) \left[\left(\frac{[m_2 \alpha j_n(m_2 \alpha)]'}{m_2 \alpha}\right) h_n(m_2 v) - \left(\frac{[m_2 \alpha h_n(m_2 \alpha)]'}{m_2 \alpha}\right) j_n(m_2 v) \right] \quad (16)$$

$$A_2 = n_2 \left(\frac{[m_1 \alpha j_n(m_1 \alpha)]'}{m_1 \alpha}\right) \left[j_n(m_2 \alpha) \left(\frac{[m_2 v h_n(m_2 v)]'}{m_2 v}\right) - h_n(m_2 \alpha) \left(\frac{[m_2 v j_n(m_2 v)]'}{m_2 v}\right) \right] + n_1 j_n(m_1 \alpha) \left[\left(\frac{[m_2 v j_n(m_2 v)]'}{m_2 v}\right) \left(\frac{[m_2 \alpha h_n(m_2 \alpha)]'}{m_2 \alpha}\right) - \left(\frac{[m_2 \alpha j_n(m_2 \alpha)]'}{m_2 \alpha}\right) \left(\frac{[m_2 v h_n(m_2 v)]'}{m_2 v}\right) \right] \quad (17)$$

$$A_3 = n_2^2 j_n(m_1 \alpha) \left[\left(\frac{[m_2 \nu j_n(m_2 \nu)]'}{m_2 \nu} \right) \left(\frac{[m_2 \alpha h_n(m_2 \alpha)]'}{m_2 \alpha} \right) - \left(\frac{[m_2 \alpha j_n(m_2 \alpha)]'}{m_2 \alpha} \right) \left(\frac{[m_2 \nu h_n(m_2 \nu)]'}{m_2 \nu} \right) \right] + n_1 n_2 \left(\frac{[m_1 \alpha j_n(m_1 \alpha)]'}{m_1 \alpha} \right) \left[j_n(m_2 \alpha) \left(\frac{[m_2 \nu h_n(m_2 \nu)]'}{m_2 \nu} \right) - h_n(m_2 \alpha) \left(\frac{[m_2 \nu j_n(m_2 \nu)]'}{m_2 \nu} \right) \right] \quad (18)$$

$$A_4 = n_2 j_n(m_1 \alpha) \left[\left(\frac{[m_2 \alpha j_n(m_2 \alpha)]'}{m_2 \alpha} \right) h_n(m_2 \nu) - \left(\frac{[m_2 \alpha h_n(m_2 \alpha)]'}{m_2 \alpha} \right) j_n(m_1 \nu) \right] + n_1 \left(\frac{[m_1 \alpha j_n(m_1 \alpha)]'}{m_1 \alpha} \right) [j_n(m_2 \nu) h_n(m_2 \alpha) - j_n(m_2 \alpha) h_n(m_2 \nu)] \quad (19)$$

These coefficients can also translate into a scattering efficiency (Q_{sca}) and scattering coefficient (μ_s) (Eqs. 10-12) to describe the optical properties of a bulk material. Scattering coefficient can also be determined with volume fraction rather than number fraction. Eq. 11-12 can be rewritten as Eq. 20 where ν is the particle outer diameter and f is the volume fraction of particles.

$$\mu_s = Q_{sca} \left[\frac{\pi \nu^2}{4} \right] \left[\frac{3f}{4\pi \nu^3} \right] = Q_{sca} \left[\frac{3f}{16\nu} \right] \quad (20)$$

4.2 Phantom validation of concentric Mie model

A brief validation of the model was performed with silicone phantoms. The phantoms consisted of soda-lime borosilicate glass microbubbles (3M Glass Bubbles) embedded in a polydimethylsiloxane (PDMS, Sylgaard, Dow Corning) matrix. Prior to fabrication, microbubbles were filtered by size to select particles between 45-100 μm . Shell thickness was calculated to be $\sim 2\text{-}5 \mu\text{m}$ based on material and particle density. Phantoms were fabricated with 30-60% microbubbles by volume. Scattering coefficients were determined by inverse adding-doubling (IAD) after obtaining sample reflectance and transmittance. As predicted by the concentric sphere model, the scattering coefficients were fairly constant over the visible spectrum, and were linearly correlated with the volume fraction of microbubbles (Figure 19). For

microbubbles with 95 μm diameter, 3.28 μm shell thickness, and a refractive index of 1.53 embedded in PDMS ($n = 1.43$), the simulation predicted a 3.20 cm^{-1} change in μ_s per percent volume fraction. Phantoms showed a relationship of 3.31 cm^{-1} per percent volume fraction ($R^2 > 0.93$). The linear regression for this data was set to have an intercept at 0, as would be theoretically expected with 0% microbubbles.

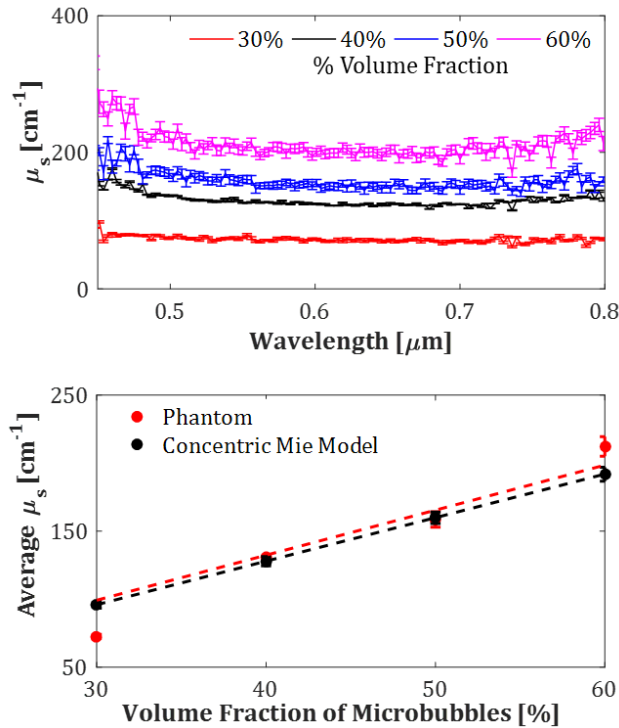


Figure 19. Phantom validation of the concentric sphere model shows a fairly constant μ_s for each volume fraction over the visible spectrum (a). The change in μ_s is linearly correlated with volume fraction in both the phantoms and the simulation (b).

4.3 Pulmonary alveoli as concentric spheres

Here, we employ a two-layer concentric sphere Mie scattering model to investigate the effects of the pulmonary surfactant layer on light scattering within the lung *in vivo* across multiple species.

The lung presents a unique problem for modeling *in vivo* radiative transport. The tissue within the lung exhibits similar absorption and scattering properties as other highly perfused soft tissues^{92, 93}. However, the airspace within the lung parenchyma is constantly changing in a living organism, which changes the bulk scattering properties of the lung⁴⁷. Structurally, the lung can be likened to a foam, with a high volume-fraction of air held within the alveoli of the lung (Figure 20).

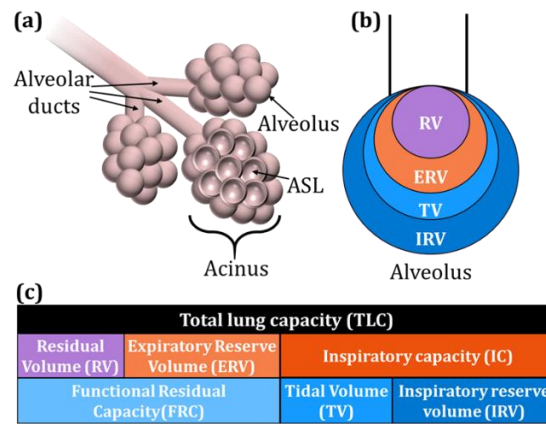


Figure 20. Lung parenchyma consists of microscale air sacs connected by airway branching (a). The alveoli expand and contract over the respiratory cycle for passive and forced inspiration and expiration (b-c). Residual volume (RV) is the minimal airspace a living organism can achieve without alveolar collapse. Expiratory reserve volume (ERV) is the difference between RV and passive breathing (forced exhale). Functional residual capacity (FRC) is the air volume in the lung at the end of passive breathing. Tidal volume (TV) is the volume fluctuation during passive breathing. Inspiratory reserve volume (IRV) is the difference between passive breathing and total lung capacity (TLC).

However, unlike traditional foams, there is no foam coarsening within the lung; there is a set number of “bubbles” (alveoli), surrounded by cells and an elastic matrix of tissue. Each alveolus—composed of epithelial cells and a layer of pulmonary surfactant and hypophase (together ASL)—grows and shrinks over the respiratory cycle^{51, 55}. Over the course of this cycle,

the air volume within the lung will oscillate between the functional residual capacity (FRC) and the maximum tidal volume (V_{Tmax}) during passive breathing, and occasionally reach the extents of the vital capacity (VC) (Figure 20c)⁹⁵. The alveoli are therefore constantly changing size, along with the volume fraction of air in the lung. Modeling the alveoli as spherical bubbles within the lung, the fields calculated by Mie scattering become dependent on the point in the respiratory cycle. Previously, the optical properties of piglet lung over the course of respiration has been modeled and characterized⁴⁷. However, this description is limited to a single animal model and ignores the effects of the airway surface liquid (ASL), a liquid coating the alveolar surface composed of fluid hypophase and pulmonary surfactant. Concentrating on the scattering due to alveolar size and structure, we expand on this model to include a surfactant and hypophase layer to the Mie alveolar model. We use this multi-layer model to estimate the lung optical properties for humans and multiple animal models for pulmonary disease, including mice, hamsters, rats, rabbits, and non-human primates (macaques) using values from the literature describing pulmonary anatomy⁹⁶⁻⁹⁹.

4.4 Scattering properties of lung parenchyma along respiration

After validation, the inputs to the concentric sphere model inputs were edited to describe physiological values (Table 9). First, scattering within the human lung was modeled at four points along the respiratory cycle: total lung capacity (TLC), maximum tidal volume (V_{Tmax}), functional residual capacity (FRC), and residual volume (RV). V_{Tmax} , FRC, and RV were assumed to 50%, 40%, and 20% of TLC, respectively. These values correspond to the airspace within the lung, tissue volume is not included in these percentages. Weibel reports that tissue volume at TLC is roughly 12% of the total lung volume⁹⁹. This constant volume is added to the airspace volume at each point in respiration to calculate a total lung volume. Alveolar diameter

was calculated for each lung volume based on the total air volume in the lung and a constant number of alveoli (Table 10). ASL thickness at the alveolar level is estimated to be 10-1000 nm^{55, 100-103}. In this model, we conserve the total volume of the ASL, and model at two volumes. At the maximum tidal volume (V_{Tmax}), the ASL thickness is assumed to be 0.5% or 1% of the alveolar radius (r_{alv}), corresponding to ~500 nm or ~1000nm thickness at V_{Tmax} . The volume of ASL at this thickness is conserved, so the shell thickness at all other points in the respiration cycle scales accordingly.

Table 9. Inputs for phantom and tissue models.

	Phantom	Tissue
n_1 (air)	1.00	1.00
n_2 (Glass/ASL)	1.53	1.33
n_3 (PDMS/tissue)	1.43	1.40

Table 10. Physiological parameters of the human lung over respiration^{104, 105}.

	Airspace volume (mL)	Tissue fraction	Alveolus volume (μm^3)	Alveolar diameter (μm)
<i>RV</i>	1000	0.38	2.06E+06	157.81
<i>FRC</i>	2000	0.23	4.12E+06	198.82
V_{Tmax}	2500	0.19	5.14E+06	214.17
<i>TLC</i>	5000	0.12	1.03E+07	269.84

The model showed that scattering coefficient (μ_s), anisotropy factor (g), and reduced scattering coefficient (μ_s') remained relatively constant over the wavelength modeled. Table 11 compares the scattering properties of the lung modeled with and without the ASL layer, averaged over the modeled wavelengths (400-850 nm). While only small changes emerge in μ_s between the simple and concentric model, the baseline of g increases with the addition of the ASL. As a result, the average μ_s' decreases by 4-7% for the thinner ASL model and 5-9% for the thicker model. Because g has slightly more variability with wavelength, this decrease is more significant

in the blue/green (4.9%) compared to the near-infrared (2.9%). As expected, the alveolar size and volume ratio affect μ_s values.

Table 11. Scattering properties of human alveoli at discrete points along the respiratory cycle.

Values are averaged over the spectrum modeled. ASL thickness modeled is 0.5% and 1% of r_{alv} at

V_{Tmax} .

	μ_s (cm^{-1})		
	No ASL	0.5%	1%
<i>RV</i>	118.73 ± 0.73	118.31 ± 0.71	118.31 ± 0.74
<i>FRC</i>	116.92 ± 0.59	116.61 ± 0.55	116.61 ± 0.55
V_{Tmax}	114.15 ± 0.57	113.87 ± 0.56	113.86 ± 0.56
<i>TLC</i>	98.36 ± 0.44	98.18 ± 0.42	98.16 ± 0.42
	g		
	No ASL	0.5%	1%
<i>RV</i>	0.811 ± 0.001	0.824 ± 0.001	0.827 ± 0.001
<i>FRC</i>	0.811 ± 0.001	0.821 ± 0.002	0.823 ± 0.001
V_{Tmax}	0.811 ± 0.001	0.821 ± 0.002	0.822 ± 0.001
<i>TLC</i>	0.810 ± <0.001	0.818 ± 0.002	0.820 ± 0.002
	μ_s' (cm^{-1})		
	No ASL	0.5%	1%
<i>RV</i>	22.45 ± 0.02	20.89 ± 0.09	20.44 ± 0.06
<i>FRC</i>	22.1 ± 0.02	20.84 ± 0.17	20.67 ± 0.07
V_{Tmax}	21.63 ± 0.01	20.41 ± 0.16	20.26 ± 0.08
<i>TLC</i>	18.66 ± 0.01	17.86 ± 0.18	17.63 ± 0.14

4.5 Modeling pathogenic states and animal models of disease

We also investigated the effect of ASL thickness on the scattering properties of the lung. Values for ASL thickness found in the literature spanned two orders of magnitude. Five points along this range were selected to compare scattering properties. It becomes clear that while the alveolar size and density affects μ_s and ASL thickness affects g —and μ_s' by extension. At a constant alveolar volume (corresponding to V_{Tmax}), a thicker ASL layer leads to a higher g (Figure 21b). A phase shift between the μ_s and g also begins to emerge, and μ_s' becomes more

variable along the spectrum (Figure 21c). This insight can be applied to pulmonary pathologies. In the case of acute lung injury, the alveolar wall can become leaky, and fluid begins to fill the alveoli, resulting in pulmonary edema. Also, chronic pulmonary diseases such as asthma and cystic fibrosis result in a collection of mucous in the airways. While the ASL in cystic fibrosis patients actually gets thinner, the refractive index of ASL and mucous are similar, so the thicker mucous layer can be modeled as a thickening ASL layer^{106, 107}. Table 12 shows the scattering properties of pathological thickening of this layer, and a full pulmonary edema, averaged over the modeled wavelength. The g value continues to rise with layer thickness, and a full edema—collapsing the model inner diameter—results in such a high g that the reduced scattering falls below 1% of μ_s . This also converges with the simple Mie scattering model of a scatterer with a refractive index of 1.35 (roughly equivalent to water, blood and mucous).

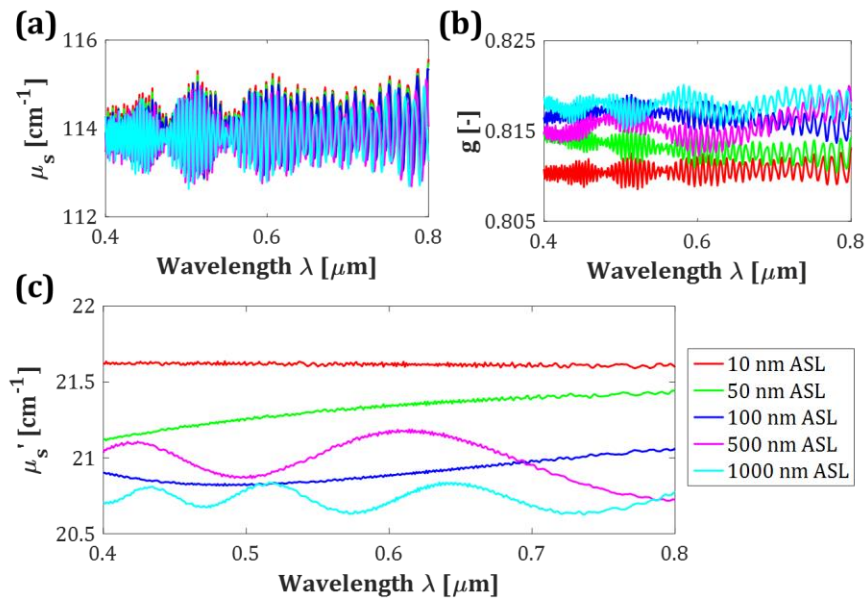


Figure 21. At a constant lung volume, μ_s is similar for all ASL thicknesses modeled (a). The change in baseline and phase of g (b) causes a shift in μ_s' and leads to unique spectral features (c).

Table 12. Alveolar scattering values with pathological thickening of fluid in alveoli (ASL, mucous, or edema fluid).

ASL (μm)	μ_s (cm^{-1})	g	μ_s' (cm^{-1})
1.5	113.82 ± 0.57	0.820 ± 0.001	20.49 ± 0.05
2.0	113.85 ± 0.65	0.822 ± 0.001	20.26 ± 0.04
3.0	113.93 ± 0.99	0.826 ± 0.002	19.81 ± 0.03
5.0	113.91 ± 0.84	0.834 ± 0.001	18.95 ± 0.02
<i>Edema</i>	113.81 ± 1.37	$0.991 \pm <0.001$	1.026 ± 0.004

Finally, we have also modeled the alveolar and ASL scattering in different animal models of pulmonary disease. Alveolar density and diameter changes between species, so the scattering modeled in human lungs cannot be extrapolated to these models. Using values from *Mercer et. al.*, we have calculated the alveolar diameter at $V_{T\text{max}}$ for macaque, rabbit, rat, hamster, and mouse lungs (Table 13)⁹⁶. Values from *Mercer et. al.* were in agreement with previous studies^{98, 99, 105, 108}. These values assume: 1) the lungs in *Mercer et. al.* were fixed at FRC and 2) the airspace volume at $V_{T\text{max}}$ scales the same as human lungs (roughly 50% TLC). Using these values and an ASL thickness of 100 nm, μ_s , g , and μ_s' were modeled for each species (Table 14). While the alveolar size and density obviously affect the material scattering characteristics, it is important to note the model sensitivity to refractive index. Specifically, this model estimates the refractive index of tissue to be 1.40. Tables 11, 12 and 14 show the scattering properties of lung tissue with these assumptions. However, the accepted values for refractive index of biological tissue range from ~1.38-1.41. For a given alveolar radius and shell thickness, the difference in μ_s' at the extents of this range is ~6.6% (data not shown). This shows that an accurate estimation of the refractive index of the tissue layer is equally important as modeling the scattering contribution of the ASL.

Table 13. Values describing alveolar physiology for different animal models of pulmonary disease as reported by Mercer *et. al.* and calculated at maximum tidal volume.

	Fixed Lung Volume (mL) <i>(Mercer et. al.)</i>	Alveoli/lung (x10⁶) <i>(Mercer et. al.)</i>	Alveolar Diameter (μm) <i>(Mercer et. al.)</i>
<i>Human</i>	2494 \pm 300	486.0 \pm 37.0	225 \pm 15
<i>Macaque</i>	313 \pm 10	85 \pm 3.0	212 \pm 10
<i>Rabbit</i>	59.9 \pm 5.4	64.9 \pm 7.0	97 \pm 5
<i>Rat</i>	8.4 \pm 0.5	19.7 \pm 2.0	94 \pm 4
<i>Hamster</i>	2.7 \pm 0.5	6.9 \pm 1.0	74 \pm 2
<i>Mouse</i>	0.7 \pm 0.1	4.2 \pm 1.0	58 \pm 4

	Air space at V_{Tmax} (mL)	Alveolus volume at V_{Tmax} (μm^3)	Diameter at V_{Tmax} (μm)
<i>Human</i>	2500	5.14E+06	214.17
<i>Macaque</i>	300.96	3.54E+06	189.10
<i>Rabbit</i>	57.60	8.87E+05	119.23
<i>Rat</i>	8.08	4.10E+05	92.17
<i>Hamster</i>	2.60	3.76E+05	89.57
<i>Mouse</i>	0.67	1.60E+04	67.39

Table 14. Alveolar scattering for humans and animal models.

	μ_s (cm⁻¹)	g	μ_s' (cm⁻¹)
<i>Human</i>	114.01 \pm 0.55	0.818 \pm 0.001	20.75 \pm 0.13
<i>Macaque</i>	129.17 \pm 0.61	0.818 \pm 0.001	23.49 \pm 0.14
<i>Rabbit</i>	205.11 \pm 1.31	0.819 \pm 0.001	37.14 \pm 0.21
<i>Rat</i>	265.53 \pm 2.08	0.820 \pm 0.002	47.93 \pm 0.26
<i>Hamster</i>	273.24 \pm 2.15	0.820 \pm 0.002	49.30 \pm 0.27
<i>Mouse</i>	363.50 \pm 2.87	0.820 \pm 0.002	65.30 \pm 0.33

In conclusion, we have used a concentric sphere Mie scattering model to show the effects of ASL thickness on alveolar scattering at discrete points along the respiratory cycle, compared normal and pathological ASL/mucous thickness, and compared scattering across multiple species. It is important to note that these values are representative of the alveolar scattering, and that the absorption and scattering of the tissue of the lung will also play a role in the organ's bulk optical properties. This model suggests that the higher anisotropy provided by the ASL

contributes to the diffusive properties of the lung seen in previous experiments and modeling of intravital pulmonary illumination [10, 11]. These results show the potential and versatility of this model to analyze optical scattering in a dynamic in vivo environment.

5. MONTE CARLO MODELING FOR OPTIMAL ILLUMINATION OF MOUSE LUNG

5.1 Illumination of mouse lung for detecting fluorescent targets

Whole-animal imaging is a powerful tool to measure biological fluorescence and bioluminescence *in vivo*; however, the thickness of tissue that the optical excitation and emission must traverse leads to low sensitivity for optical targets located deep within the body⁴². A small animal whole-body imaging system using epi- or trans-illumination [Figure. 22(a)-22(b)] has been employed to detect a tdTomato-expressing strain of mycobacteria (Bacillus Calmette-Guerin - BCG) or Mtb-specific near infrared (NIR) reporter enzyme fluorescence (REF) probes *in vivo* in a mouse model^{39, 40, 109, 110}. These external illumination methods allow for longitudinal studies, but unfortunately, suffer from a relatively high detection threshold compared to physiologically relevant infectious doses of 1-10 bacteria¹¹¹. A pulmonary bacterial load of 10^5 colony forming units (CFU) or higher is needed to effectively detect signal. This high detection threshold limits these methods when determining therapeutic efficacy of antimicrobials for pathogenic bacteria. Recently, a microendoscope has been incorporated into the animal imaging system as an alternate illumination source to more effectively deliver the higher energy excitation light into the lung of the animal where the bacterial fluorescent target resides [Figure. 22(c)]. This addition to the imaging system improves the detection threshold by orders of magnitude^{45, 83}.

* Reprinted with permission from “Optical model of the murine lung to optimize pulmonary illumination” by Durkee, Madeleine S., Nooshabadi, Fatemeh, Cirillo, Jeffrey D., Maitland, Kristen C., 2018. Journal of Biomedical Optics, 23, 071208, Copyright 2018 by International Society for Optics and Photonics.

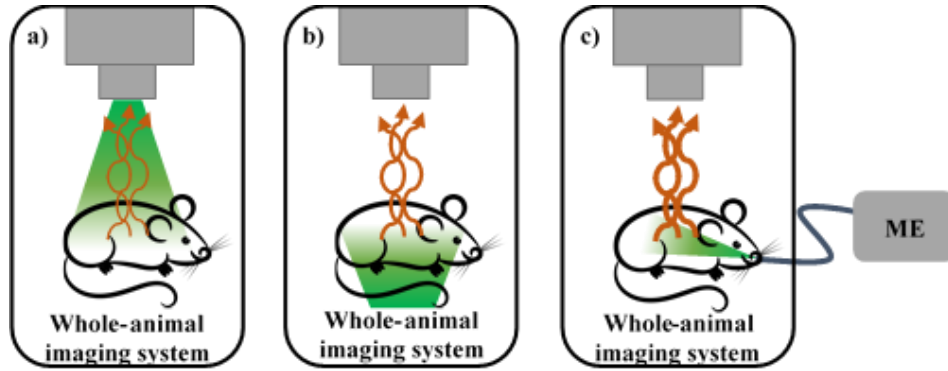


Figure 22. Fluorescence whole-animal imaging of mice can be accomplished through multiple illumination pathways including (a) external epi-illumination, (b) external trans-illumination, and (c) internal illumination with a microendoscope (ME) light source.

The sensitivity of whole-animal fluorescence imaging is also dependent on animal position. Figure 23 shows the irradiance collected from infected mice, including signal, tissue autofluorescence, and any source leakage. External illumination suffers from a high detection threshold at both ventral and dorsal positions. Fluorescence detection with internal illumination is also position dependent, with the dorsal position having an improved signal to noise ratio⁸³. Whether these differences stem from ineffective illumination of the lung or a limitation of collecting fluorescence signal is unknown, but this knowledge is integral to optimization of the imaging system for detection of low bacteria levels. A three-dimensional model of animal illumination will help explain differences in both the light source and animal position in effectively coupling excitation light into the lung where the bacteria reside.

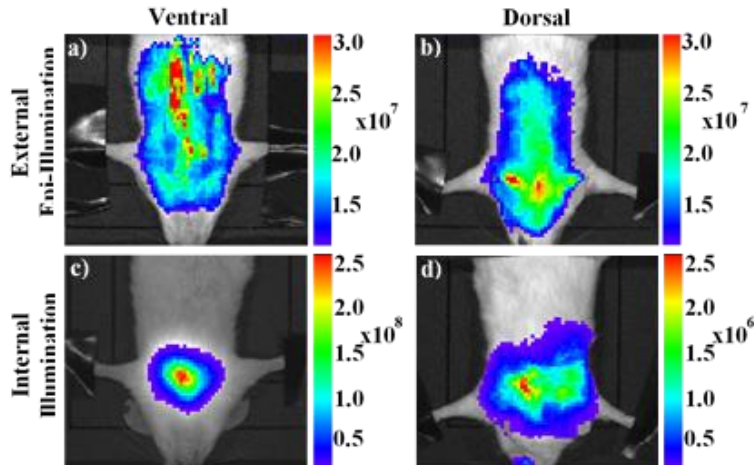


Figure 23. Position of the mouse in the imaging system effects collected fluorescence. Mice were intratracheally infected with 10^6 colony forming units BCG and administered REF substrate 24 hours post-infection. Fluorescence distribution is different with external epi-illumination in the ventral (a) and dorsal (b) position. Under the same infection conditions, detected fluorescence intensity with internal illumination also varies for mice imaged in the ventral (c) and dorsal (d) positions. Although the fluorescence signal is higher in the ventral position (c), the signal to noise ratio was found to be significantly higher for the dorsal position (d).⁸³ All radiance values are measured in photons/second/cm²/steradian.

Radiative transport models, specifically Monte Carlo simulations, are a powerful tool in quantifying the photon flux within biological tissue to help with optimizing medical and biological imaging techniques^{56, 112}. These models are a stochastic version of the radiative transport equation (RTE) in which the optical properties of the material—in this case, biological tissue—determine the path of a photon through that material. Therefore, an accurate solution to the RTE can be generated with a sufficiently high photon count. The scope of the application of Monte Carlo methods to biological systems has been expanded to represent complex, 3D biological structures, ranging from cutaneous blood vessels to a whole-mouse model, by using a variety of methods including voxelated models and triangulated meshes¹¹³⁻¹¹⁸.

We are primarily interested in light transport within the lung as the predominant organ affected by tuberculosis. However, to compare the effects of external illumination and different animal positions to internal illumination with a fiber optic source, we must also simulate the torso of the animal, and other organs that may have a significant effect on delivery of excitation light to fluorescent targets within the lung. LightTools (Synopsys, Inc.) illumination software uses the Monte Carlo method to track photons through free space and turbid media. This software has been used to model radiative transport in multi-layer epithelial models¹¹⁹ and in a more complex whole-finger model for the design of a ring pulse oximeter¹²⁰. For the purposes of designing a full-torso mouse model with external and internal illumination, the airway is a primary component of our illumination model. A solid model of the airway was imported into LightTools for the illumination model. The model described below compares various strategies of external and internal illumination of a mouse torso, including airway, lung, heart, and other soft tissues, to determine the optimal illumination strategy for sensing fluorescent bacteria or a bacteria-sensing probe at a low bacterial load in a live mouse. The system is modeled at visible and NIR wavelengths to account for fluorescence from genetically-modified bacteria (visible), and the bacteria-sensing fluorogenic probe (NIR)^{45, 83}. Rapid evaluation of modifications to the internal illumination system, including addition of a light diffuser tip, positioning of the fiber source within the airway, and modified divergence angle of the fiber source, are enabled by the computational model without the need for extensive animal experiments.

5.2 Phantom design and simulation validation

In the development of a computer model to simulate light transport in the mouse lung, a simplified physical lung phantom was first designed to validate the computational model. Optical properties of excised mouse lung tissue were experimentally measured and used as inputs into

the simplified model and phantom design. The validation model consisted of a block tissue phantom with the optical properties of a deflated mouse lung and a mesoscale, simplified airway. Once validated with imaging of the phantom, a more complex and anatomically representative airway, lung, and torso structure was generated in the computer model. Various illumination configurations were tested using this model. All Monte Carlo simulations (validation studies and the advanced model) were completed using LightTools Illumination software on a personal desktop computer (6 core Intel i7 processor, 3.3GHz, 72GB RAM).

5.2.1 Optical properties of healthy and infected mouse lung

Optical phantoms were created from PDMS with India ink and titanium dioxide (TiO_2) to replicate the measured absorbing and scattering properties of lung tissue, respectively. Two separate phantoms were created to simulate the optical properties of the tissue at the two wavelengths of interest (Table 15). Phantom 535 contains 3 mg TiO_2 and 7.5 μL India ink per gram of PDMS and approximates infected lung measured at 535 nm. Phantom 730 contains 2 mg TiO_2 and 3.5 μL India ink per gram of PDMS and models the infected lung at 730 nm. Both phantoms were imaged at both illumination wavelengths to provide additional validation data for the computer model.

5.2.2 Phantom fabrication

Structurally, the lung has a unique surface for internal illumination through the trachea. On the mesoscale, the airway branching results in a complex air-tissue interface where a stark contrast in refractive index between air and tissue will affect the transport of photons within the organ. The airway was included in both the computational and physical models of the physiological system to better evaluate the accuracy of the simulation to a biological environment. A fractal tree mock-airway was designed and printed out of a base-soluble material

as an internal mold for the PDMS airway phantom. The preliminary structure shown in Figure 24(a) was designed to be easily 3D printed in-house on a fused deposition modeling (FDM) printer (Stratasys®, Fortus360mc). This soluble structure was secured in a rectangular mold for pouring the PDMS and optical particle mixture. Upon curing, the mock airway was dissolved out of the phantom, leaving an airway void and a pathway for internal illumination of the solid rectangular block phantom. This method of incorporating complex geometry into a silicone matrix has previously been employed for designing flow systems for surgical training¹²¹. 3D printing is also becoming a popular method for fabricating phantom molds and for manufacturing the phantoms themselves¹²²⁻¹²⁴. The phantom fabrication methods used here are described in full detail by Durkee et. al¹²⁵.

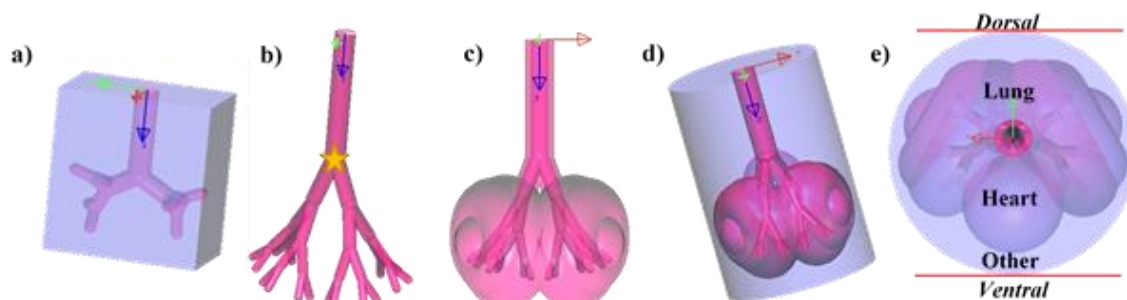


Figure 24. 3D models for photon transport in LightTools. The rectangular phantom used for validation studies has a 4-generation fractal tree as a model airway (a). The full-torso model of the mouse includes a more anatomically accurate model airway (b) and lungs of comparable volume to that of a mouse. The lung and heart are immersed in a cylindrical model of other soft tissues (d-e). The star in (b) is the location of the internal illumination source.

5.2.3 Validation of illumination model with phantom imaging

Imaging of the lung phantoms was performed in an IVIS Lumina II (PerkinElmer) whole-animal optical imaging system to validate the computer simulation of the analogous simplified model. For internal illumination, the IVIS illumination pathway was blocked, and a fiber

microendoscope light source was inserted into the airway void until the tip was in contact with the wall at the bifurcation¹²⁶. The microendoscope output power was set at 1 μ W for both wavelengths. The IVIS emission filter wheel was set to ‘open’ to collect the illumination light, and camera settings were set to automatic exposure. Total irradiance of the top surface of a phantom measured by the IVIS imaging system was compared to the simulation for 535 nm and 730 nm illumination studies.

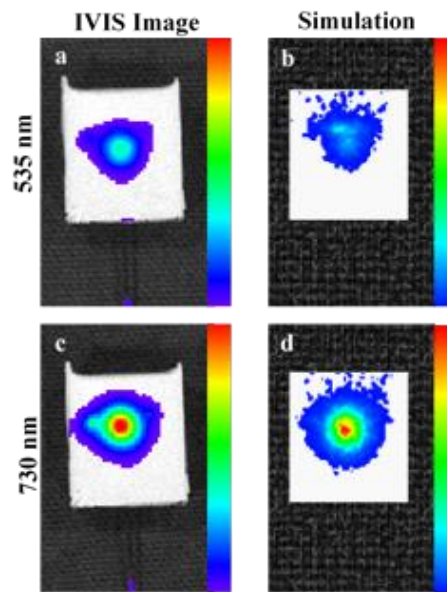


Figure 25. Validation of the computational model with IVIS imaging of optical phantoms shows a similar irradiance profile at the phantom surface. Phantom 535 is shown here illuminated internally with 535 nm (a) and 730 nm (c) microendoscope sources. The simulation replicates total flux output to the detector (Table 15) and the irradiance profile at 535 nm (b) and 730 nm (d).

The measured optical properties of the phantoms and the accuracy of the simulation to reproduce the experimental IVIS imaging results are shown in Table 15. The simulation was able to replicate the total photon flux within 5.0% for both phantoms at both wavelengths. Figure 25 also demonstrates a similar irradiance profile between phantom imaging and the computational model for both wavelengths. After verifying agreement between the computational and physical

models, we expanded on the computational model to better mimic the murine anatomy, as shown in Figure 24. All results following verification are from this advanced model.

Table 15. Absorption coefficients (μ_a) and reduced scattering coefficients (μ_s') of infected mouse lung and validation phantoms at wavelengths of interest. Percent error between total flux measured experimentally with the phantom and simulated in the model.

Measured infected, deflated mouse lung tissue			
Wavelength (nm)	μ_a (cm^{-1})	μ_s' (cm^{-1})	
535	5.99 ± 1.92	43.5 ± 14.6	
730	1.06 ± 0.49	35.2 ± 11.7	
Phantom properties and validation results			
Phantom 535	μ_a (cm^{-1})	μ_s' (cm^{-1})	Error [%] of Simulation v. Phantom
535nm	4.53	67.4	4.59 %
730nm	3.75	52.1	4.40%
Phantom 730	μ_a (cm^{-1})	μ_s' (cm^{-1})	Error [%] of Simulation v. Phantom
535nm	2.22	44.5	3.66 %
730nm	1.75	35.3	2.86%

5.3 Simulation design of murine anatomy and optical properties

Once the simulation was validated using the simplified phantom, the airway structure within the simulation was updated to be more representative of the largest branches of the murine airway [Figure 23(b)] based on computed tomography (CT) images^{127, 128}. The simulated lung was designed around the airway [Figure 23(c)], with the general anatomy and size constraints of the mouse lung modeled after similar CT images^{129, 130}. *In vivo*, the lung is a dynamic and porous organ that scatters light much more effectively than solid tissue. Within the computational model, the lung properties can be adapted from the measured values of deflated lung to represent inflated lung at different points in the respiratory cycle. Here, we optimize the

computational model to represent a point in the cycle indicative of passive respiration in order to analyze the illumination performance of external and internal illumination sources. The heart and other soft tissues are also represented [Figure 23(d)-23(e)] to more effectively model external illumination and to address photons scattered into the lung after traversing other tissues.

5.3.1 Simulated properties of inflated mouse lung

The optical properties of the lung were measured after excision, assuming the organ was deflated. In a living mouse, the lung will always have some level of inflation, with air making up at least 30% of the organ volume after expiration, and up to 90% of the organ volume after inspiration^{131, 132}. The simulated optical properties can be mathematically manipulated to represent the scattering and absorption of an inflated lung, based on the optical properties of the deflated lung, and the alveolar size and density⁹⁵.

For this model, we assumed a constant alveolar diameter of 55 μm ¹³³. Alveoli were assumed to be spherical in the calculation of the volume of a single alveolus, V_{alveolus} . A number density of alveoli was calculated based on mouse lung characteristics. First, because we have a static model, we assumed a constant level of inflation with air composing 80% of the organ volume. Using this inflation factor, f_i , and the properties listed in Table 16, the number of alveoli (N_{alveoli}) in the lung was calculated using

$$N_{\text{alveoli}} = f_i \frac{V_{\text{lung}}}{V_{\text{alveolus}}} . \quad (21)$$

The alveolar density,

$$\rho_{\text{alveoli}} = \frac{N_{\text{alveoli}}}{V_{\text{lung}}} , \quad (22)$$

was calculated to be 9,195 alveoli/ mm^3 . The alveolar density was used to find the new reduced scattering coefficient, μ_s' , of the inflated lung,

$$\begin{aligned}\mu_s'_{lung} &= \mu_s'_{tissue} + \mu_s'_{alveoli} \\ &= \mu_s'_{tissue} + (\rho_{alveoli}\sigma_s(1 - g_{alveoli}))\end{aligned}\quad (23)$$

(adjusted from Beek, et. al. ⁹⁵), where $\mu_s'_{tissue}$ was measured from the deflated tissue. Treating the alveoli as scatterers dispersed in lung tissue, the radius and refractive index of the alveoli allow the alveolar cross section to be used as the scattering cross-section (σ_s), as the alveoli fall into the regime of geometric optics ¹³⁴. The anisotropy factor, g , of the alveoli was estimated at 0.6⁹⁵. The resulting reduced scattering coefficients (μ_s') and mean free paths ($MFP = 1/\mu_s'$) are comparable to that of liquid foams with a similar liquid fraction to the air-tissue ratio used in the lung ^{135, 136}.

Table 16. Properties of inflated mouse lung used to calculate approximate optical properties.

*Lung tissue volume was calculated from lung volume and an inflation factor of 0.8.

Inflated lung characteristics				
Property	Value(s) in literature		Value used in model	
<i>Lung volume at max inspiration (mm³)</i>	1000-1500 ^{133, 137, 138}		1060	
<i>Lung tissue volume (mm³)</i>	100-200 ^{139, 140}		212*	
<i>Alveolar diameter (μm)</i>	35-75 ^{100, 141}		55	
Lung optical properties				
Wavelength (nm)	Deflated μ_a (cm⁻¹)	Deflated μ_s' (cm⁻¹)	Inflated μ_a (cm⁻¹)	Inflated μ_s' (cm⁻¹)
535	5.99	43.57	1.20	130.84
730	1.07	35.27	0.21	122.54

The absorption coefficient, μ_a , of inflated lung was also adjusted because the path length available for absorption changes significantly with air in the tissue⁹⁵. For the level of static inflation assumed in this model, only 20% of the total lung volume, V_{lung} , is actually tissue, V_{tissue} . With no absorption occurring in the air-space, the absorption coefficient is reduced according by this factor,

$$\mu_{a,lung} = \mu_{a,tissue} \frac{V_{tissue}}{V_{lung}}. \quad (24)$$

5.3.2 Heart and other soft tissues

The heart is important in this simulation because of its high blood content, and therefore high absorption in the visible range. While a majority of the photons contributing to the illumination profile of the lung come directly from the internal source, some fraction of the light will escape into the surrounding tissue. The properties of that tissue, including the heart, will determine how much the illumination of the lung is affected by its surroundings. The heart is assumed to be mainly an absorber, and the optical properties of partially oxygenated blood are used for the heart in this model (Table 17)¹⁴². The remaining tissue includes muscle, fat, skin, and bone; although, bone is not included in this model for simplicity. Overall optical properties for the collective “other soft tissues” are estimated based on values from the literature⁵¹ and are listed in Table 17. These values were used to determine the mean free path (MFP) and transmissivity (T) as inputs for the heart and other soft tissue materials. LightTools was set to interpolate values to determine the properties of material at wavelengths within the range listed in Table 17. If a wavelength simulated was out of the range listed, the value closest to that wavelength is used. For example, the optical properties of the heart at 535 nm were identical to those listed at 665 nm in Table 17.

Table 17. Optical properties for other soft tissues from Ref. 30. Values denoted with ‘*’ were calculated from scattering coefficient and anisotropy factor. Values from LightTools biological materials library were used for heart optical properties.

Epidermis		
Wavelength (nm)	μ_a (cm⁻¹)	μ_s' (cm⁻¹)
514	3.0	58*
585	3.0	41*
800	2.3	30*
Dermis		
Wavelength (nm)	μ_a (cm⁻¹)	μ_s' (cm⁻¹)
514	4.4	139*
585	3.6	99*
800	4.0	62*
Subcutaneous fat		
Wavelength (nm)	μ_a (cm⁻¹)	μ_s' (cm⁻¹)
520	4.4	33.1
570	3.1	28.9
820	1.0	19.8
Muscle		
Wavelength (nm)	μ_a (cm⁻¹)	μ_s' (cm⁻¹)
633	1.21	8.9
900	0.32	5.9
Calculated properties for “other soft tissues”		
Wavelength (nm)	μ_a (cm⁻¹)	μ_s' (cm⁻¹)
514	1.84	17.19
585	1.70	16.33
800	0.644	10.96
Heart		
Wavelength (nm)	μ_a (cm⁻¹)	μ_s' (cm⁻¹)
665	12.37	6.23
960	4.97	4.04

5.3.3 Illumination and detection parameters

The fiber bundle microendoscope used for internal illumination has a divergence half angle of 20.5°, and experimental protocol specifies the endoscope should be in contact with the tissue for imaging. This internal source was modeled as a point source with a divergence half angle of 20.5° to mimic the fiber bundle used in imaging experiments^{45, 83}. To model epi-

illumination within the whole-body imaging system, dorsal and ventral external illumination sources were placed 20 mm away from the simulated phantom or torso and uniformly illuminated a plane located at the surface nearest to that source. Validation simulations were run with $1e6$ photons with a source power of $1 \mu\text{W}$. All simulations of the mouse torso model were run in triplicate with $1e5$ photons. External illumination simulation times ranged from 30-45 minutes, and internal illumination simulation times ranged from 3.5-4 hours depending on source wavelength. External and internal sources at both wavelengths were set to 1 mW total power emitted.

Illumination of the lung was analyzed using average fluence rate in the lung and source efficiency, defined as average fluence rate in the lungs relative to average fluence rate in the entire simulated torso. Detection planes parallel to the coronal plane were placed at 0.5 mm intervals through the solid model of the torso to directly record photon flux, with bins of $0.1 \text{ mm} \times 0.1 \text{ mm}$ in each collection mesh. The complete detection matrix is $200 \times 250 \times 35$ elements, corresponding to a total of $1.75e6$ elements (8750 mm^3).

Spatial distribution of the light within the lung was analyzed by fitting the average fluence rate in the detection planes to the exponential curve,

$$f(x) = a * e^{-bx} . \quad (25)$$

where a is the average fluence rate nearest the source and b is the decay constant. For external illumination, a is calculated at the ventral or dorsal plane, and for internal illumination, a is calculated at the plane intersecting the internal source. Therefore, these decay curves move across the body for external illumination, and from the source outward for internal illumination. To quantitatively compare different sources, an average fluence rate for the entire lung was calculated from the collection matrix by masking each detection plane with the intersecting lung

geometry. The fluence rates from the masked data were averaged over the collection matrix to get an average fluence rate within the lung. The computational model of the mouse torso was used to evaluate 1) internal and external illumination, including ventral and dorsal positioning of the mouse; 2) the addition of a diffuser tip for radial illumination from the internal source; 3) positioning of the internal illumination source relative to the tracheal bifurcation; and 4) divergence angle of the optical fiber output.

5.4 Intravital v. external illumination of mouse lung

As described earlier, the position of the mouse relative to an external illumination source has an effect on the signal collected from a fluorescent target within the lung. The three-dimensional illumination of the lung was analyzed for external illumination from the dorsal and ventral sides, and for internal illumination. An internal source in contact with the tissue with a divergence half angle of 20.5° was used for the comparison between internal and external illumination.

Figure 24(e) shows a transverse view of the optical model, with the dorsal and ventral sides indicated. The asymmetry between dorsal and ventral causes a difference in the illumination profile of the lung [Figure 26(a)-26(b), 26(d)-26(e)]. Both positions yield an exponential decay in fluence rate with depth in the lung [Figure 26(g)]. The decay constant, b , varies for both orientation of the external source and wavelength ($p < 0.0001$) according to a comparison of fits of a nonlinear regression for each illumination strategy (Table 18). The difference in penetration depth of external illumination is most drastically affected by the heart, the main organ between the source and the lung in the ventral position. As a highly absorbing organ (due to blood content), the heart prevents a portion of the illumination from reaching the lungs, resulting in a lower a -parameter in the corresponding decay equations in Table 18.

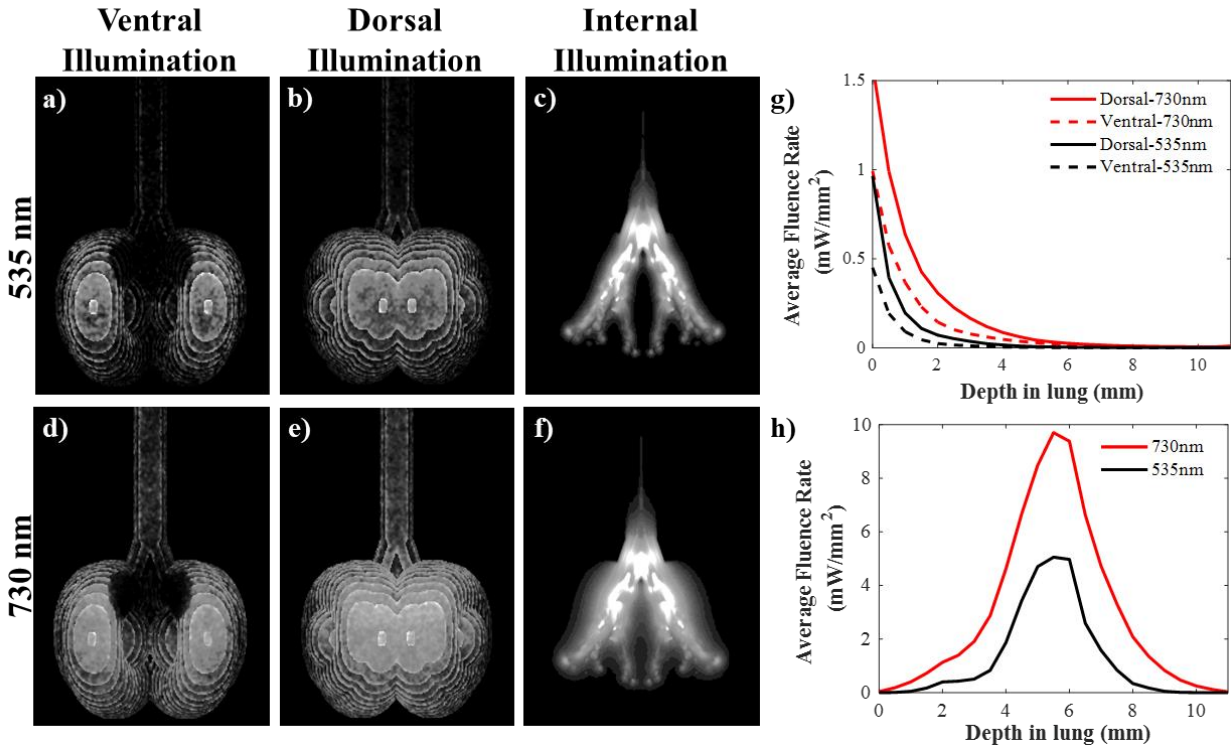


Figure 26. Maximum intensity projections of fluence rate (mW/mm²) are shown for ventral external illumination (a, d), dorsal external illumination (b, e), and internal illumination (c, f). Greater penetration can be seen at the excitation wavelength for the REF NIR probe (d-f) compared to that of tdTomato (a-c). All projections with epi-illumination are normalized to have the same maximum. Internal illumination projections are saturated to that maximum to better represent the fluence rate on the same scale. The average fluence rate within the lung decreases exponentially with distance away from the source for both external illumination (g) and internal illumination (h).

Internal illumination avoids the problem of traversing other tissues, and minimal light is lost to surrounding tissue. The illumination still decays exponentially with distance from the light source [Figure 26(h), Table 18], but the efficiency of the light source at coupling light into the lung is much higher (>60%), compared to less than 10% efficiency for either external illumination orientation at either wavelength (Table 19). The average fluence rate in the lung

with the internal source is also significantly higher than external illumination when the sources have equal power ($p \ll 0.0001$).

Table 18. Decay of fluence rate within lung. Average power was fit to a decaying exponential:

$f(x) = a \cdot \exp(-b \cdot x)$ where a is the initial average fluence rate at the detection plane nearest the source and b is the decay constant.

External illumination (decay from lung surface inward)	Initial average fluence rate (mW/mm²) (a)	Decay constant (b)	R²
<i>Dorsal- 535nm</i>	0.9546	1.642	0.9958
<i>Ventral- 535nm</i>	0.4476	1.631	0.999
<i>Dorsal- 730nm</i>	1.563	0.8641	0.9978
<i>Ventral- 730nm</i>	0.9782	0.997	0.9977
Internal illumination (decay from trachea outward)	Initial average fluence rate (mW/mm²) (a)	Decay constant (b)	R²
<i>Trachea → Dorsal side- 535nm</i>	4.948	1.194	0.9985
<i>Trachea → Ventral side- 535nm</i>	4.874	0.9384	0.9852
<i>Trachea → Dorsal side- 730nm</i>	9.476	0.6618	0.999
<i>Trachea → Ventral side- 730nm</i>	8.785	0.6207	0.9936

Table 19. Ability of different illumination sources to couple light into the lung.

Illumination	Efficiency at 535 nm	Average fluence rate at 535 nm	Efficiency at 730 nm	Average fluence rate at 730 nm
<i>External- Dorsal</i>	3.14%	0.064 $\mu\text{W}/\text{mm}^2$	2.77%	0.20 $\mu\text{W}/\text{mm}^2$
<i>External- Ventral</i>	1.05%	0.020 $\mu\text{W}/\text{mm}^2$	1.21%	0.089 $\mu\text{W}/\text{mm}^2$
<i>Internal</i>	66.66%	3.8 $\mu\text{W}/\text{mm}^2$	76.92%	8.9 $\mu\text{W}/\text{mm}^2$

Previous animal experiments show a difference in fluorescence detected in different positions of the mouse in the imaging system, specifically in positioning the mouse ventrally or dorsally within the imaging system⁸³. Simulations of dorsal and ventral external illumination

show that positioning the mouse dorsally with respect to the external imaging source more effectively couples the excitation light into the lung, supporting previous experimental results. The main explanation for this is the location of the heart within the thoracic cavity. At visible wavelengths, the heart and blood are highly absorbing. In the NIR, the heart does not absorb as much light, but it increases the path length that a photon must travel to arrive at the lung, increasing the likelihood that a photon is absorbed or scattered away from the lung. This model demonstrates the effect of the heart on ventral illumination. The simplification of all other biological tissues into one layer is an approximation, but is anatomically similar from either side of the animal, incorporating skin, other soft tissue, and rib cage (not included in this model), which are all present both ventrally and dorsally.

5.5 Intravital illumination source manipulation

The goal of the internal illumination source is to better couple excitation light into the tissue of interest, which may contain a fluorescent marker. For the specific application of detecting bacteria within the lung, there is no a priori knowledge about the location of the bacteria within the lungs of a given mouse. Diffuse, widespread illumination would therefore be an ideal tool for effectively detecting low numbers of bacteria within the lung. By simulating the physiology of the mouse and the optical system, the efficacy of different sources, different protocols, and even different animal positions can be analyzed without performing a large number of animal imaging experiments.

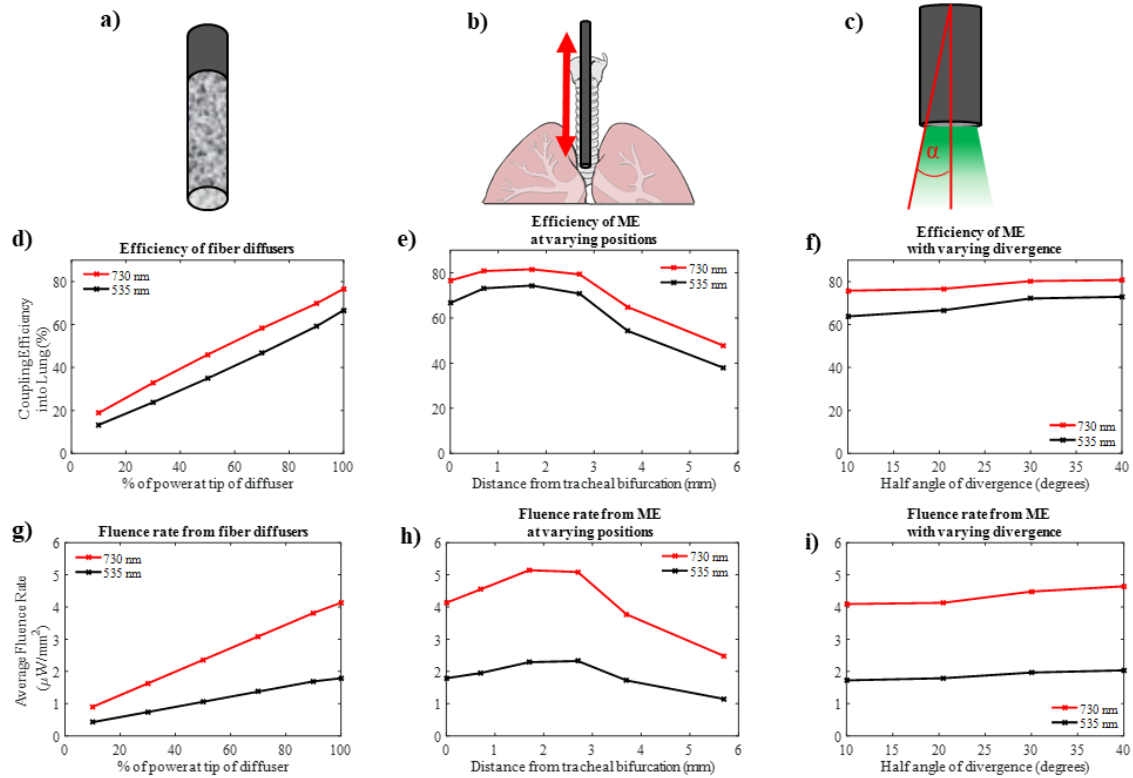


Figure 27. The fluence rate in the lung is sensitive to the parameters of the internal source, including diffuser tip (a), fiber position (b), and divergence angle of the fiber (c). The efficiency of a fiber diffuser increases as more source power is emitted through the tip of the fiber rather than radially (d). The microendoscope (ME) efficiency is more sensitive to position (e) than divergence angle (f). The average fluence rate in the lung follows similar trends to efficiency for all source manipulations (g-i).

5.5.1 Fiber diffuser

Simulations and previous animal experiments indicate that internal illumination is more efficient than external illumination in either position. To estimate the potential for further improvement in illumination of the lung, modifications to the internal source were designed and tested with the optical model. First, a 5 mm long cylindrical light diffuser design was simulated [Figure 27(a)]. Diffusing fibers can be designed to preferentially emit light radially or out the distal end of the diffuser¹⁴³. The percentage of power emitted from the distal end of the diffuser

relative to the homogeneous radial emission along the length of the diffuser was varied from 10% to 100%. 100% power emitted from the tip of the diffuser is equivalent to the microendoscope condition. All simulations were performed with the diffusing fiber tip in contact with the tissue at the tracheal bifurcation. As less power was emitted along the length of the diffuser, the efficiency of the source at coupling light into the lung increased, along with average fluence rate in the lung. Trends in efficiency and average fluence rate were similar across both wavelengths of interest [Figure 27(d), 27(g)].

5.5.2 Position of internal illumination source

The original internal source modeled off the microendoscope specifications was simulated at different positions within the trachea to determine the effect of source placement on the illumination of the lung [Figure 27(b)]. Starting with the internal source in contact with the tissue at the tracheal bifurcation (0 mm), the endoscope was moved away from the tissue surface, up to 6 mm offset, effectively pulling the endoscope out of the airway. As the internal source was moved away from the tracheal bifurcation [Figure 27(e)], the efficiency increased moderately ($p \ll 0.0001$) until peaking near 2 mm distance from the bifurcation, then decreased below the initial efficiency at the tissue surface. In the region where efficiency hit a maximum, the simulation also indicated a maximum fluence rate within the lung [Figure 27(h)].

5.5.3 Divergence angle of microendoscope

The final source manipulation simulated was changing the divergence angle of the fiber bundle source [Figure 27(c)]. The effects of the divergence angle on illumination were simulated for angles above and below the current design (20.5° half angle). The simulation results show an upward trend with increasing angle [Figure 27(f), 27(i)], with a slope of $0.021 \mu\text{W}/\text{mm}^2/^\circ$

divergence and $0.039 \mu\text{W}/\text{mm}^2/^\circ$ divergence for NIR and visible wavelengths, respectively ($R^2 > 0.90$).

5.5.4 Optimal parameters of internal source

Illumination of the mouse lung was improved by independently changing the location and divergence of the internal source. The optimal source placement and optimal angle were combined to further improve the lung illumination. To find the optimal illumination, a divergence half angle of 40° and source locations of 0.7 mm and 1.7 mm away from the tracheal bifurcation were selected as inputs for the optical model. While these simulations show an improved illumination over the current experimental design, the optimal internal source parameters were achieved at the original 20.5° divergence half angle with the source placed 1.7 mm away from the tissue surface at the tracheal bifurcation (Table 20).

Table 20. Parameters and performance of optimized internal illumination. The bolded values are represented spatially in Figure 28.

Modified Internal Source Parameters					
<i>Divergence angle</i>	20.5°	40°	20.5°	40°	40°
<i>Offset from tissue</i>	0 mm	0 mm	1.7 mm	0.7 mm	1.7 mm
535 nm					
<i>Efficiency of coupling to lung</i>	66.66%	72.91%	74.40%	73.24%	62.90%
<i>Avg. fluence rate in lung</i>	$3.8 \mu\text{W}/\text{mm}^2$	$4.3 \mu\text{W}/\text{mm}^2$	$4.9 \mu\text{W}/\text{mm}^2$	$4.7 \mu\text{W}/\text{mm}^2$	$4.4 \mu\text{W}/\text{mm}^2$
730 nm					
<i>Efficiency of coupling to lung</i>	76.92%	81.14%	82.05%	81.28%	72.30%
<i>Avg. fluence rate in lung</i>	$8.9 \mu\text{W}/\text{mm}^2$	$10.1 \mu\text{W}/\text{mm}^2$	$11.0 \mu\text{W}/\text{mm}^2$	$10.8 \mu\text{W}/\text{mm}^2$	$9.5 \mu\text{W}/\text{mm}^2$

The fiber diffuser was determined to be a poor illumination source in the trachea due to its low efficiency of coupling light into the lung. While it did show a more uniform illumination

of the lungs, the light coupled into the lung was much lower than the current microendoscope design. It is possible that a single lobe of the lung could be illuminated well by the fiber diffuser if the diffuser could be positioned deeper into the airway. In the current model, most of the power that was emitted along the length of the diffuser escaped through the trachea and into the surrounding tissue without ever reaching the lung. While positioning the diffuser deeper in the lung could remedy this, the current microendoscope does not have the capability to steer the tip in the airway. The current fiber bundle diameter (0.66 mm) is close to the inner diameter of the trachea (~1.3 mm), so there is also an anatomical size limitation with going much deeper in the mouse lung with these sources. Given a larger animal model, such experiments and corresponding simulations might be feasible.

The most effective manipulation of the internal illumination source was the placement of the source within the trachea. While the simulations indicate an enhanced illumination of the lung model, the effect of source placement *in vivo* may vary between animals. The airway will follow similar branching patterns in every mouse, but variability in animal size and lung development will likely hinder the reproduction of the simulation results *in vivo*. A change in the experimental protocol would still be recommended, as a small distance between the light source and tracheal bifurcation should show an increase in delivery of light to the lungs in any animal.

While changing the divergence angle of the source did not show the greatest increase in source efficiency or average fluence rate in the lung, it may be the best way to reproducibly enhance the illumination of the lung in animal experiments. An increase ($p \ll 0.0001$) in average fluence rate and coupling efficiency into the lung was found with the 40° half angle source relative to the current 20.5° half angle divergence of the micro-endoscope source. An

increase of average fluence rate in the lung is expected to be more consistent with this change to the optical system than with an optimized experimental protocol regarding source placement.

5.5.5 Illumination with optimal source

To illustrate the light distribution in the lungs, the radiant flux of each detection plane was combined into a 3D representation of intravital illumination of the lung at both wavelengths of interest. Maximum intensity projections for each orientation are shown in Figure 28(a)-28(c) for 535 nm and Figure 28(d)-28(f) for 730 nm illumination to describe the spatial variance in the radiant flux. Video 1 [Figure 28(g)] of the complete rotating volumes at 535 nm (top) and 730 nm (bottom) show the dependence of radiant flux on the illumination wavelength due to the differences in optical properties.

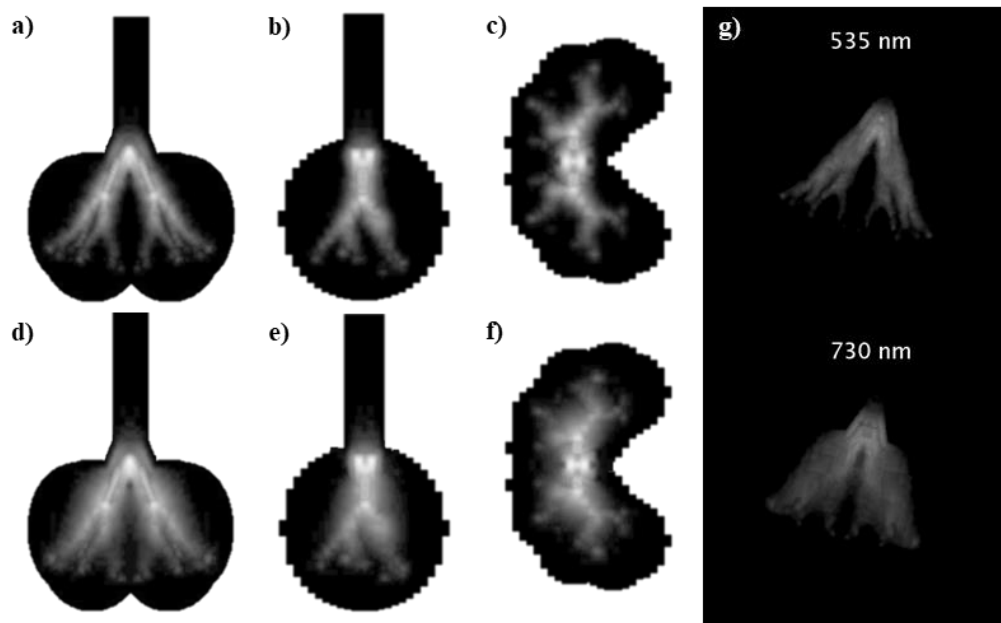


Figure 28. The three-dimensional illumination of the lung is shown for 535 nm (a-d) and 730 nm (e-h). Maximum intensity projections of the fluence rate (mW/mm^2) in the coronal plane (a, d), sagittal plane (b, e), and transverse plane (c, f). A mask of the lung is also shown in each projection. (g) 3D rendering of the illumination is shown for both wavelengths.

5.6 Limitations of illumination model

The optical simulation was designed to analyze the three-dimensional illumination of a complex physiological system, and optimize the illumination source and protocol for detection of optical targets *in vivo*. While the model is structurally and optically complex, it is important to note the assumptions and limitations of the optical model. An advanced phantom was designed to validate the ability of the optical model to replicate the boundary conditions of an internal airway and source placement within that airway. Due to manufacturing constraints, the airway modeled in the validation studies is less anatomically accurate than the airway in the full torso model. Assuming that this structural change does not affect the accuracy of the optical simulation, all tissue structure in the final model remains only an approximation of the natural anatomy.

While the porous tissue of the lung is approximated with the shifted scattering properties, in reality, the airway is continuous with the alveolar ducts and sacs. The boundary between the airway and the tissue might lead to some inaccuracy in the model, but it is assumed to be an underestimation of the diffusive properties of the lung. As the airway acts somewhat as a light guide, a continuous structure would likely yield a more uniform illumination. Unfortunately, modeling a structure of this complexity within a high-photon count Monte Carlo simulation is highly intensive computationally.

Simplifying all tissue except the lung and the heart into one bulk tissue layer might cause discrepancies in the model, particularly with the external illumination model. With fur unaccounted for on the external surface of the model, this model will overestimate the transmission of external illumination into the thoracic cavity. For internal illumination, the properties of this tissue layer have only a small effect on the illumination of the lung.

It is also important to note that both the internal and external power sources modeled are normalized to 1 mW. For animal experiments with this application, internal illumination power ranges from hundreds of microwatts to ~1.3 mW, and external illumination power is controlled by the IVIS software, but can be estimated to range from milliwatts to watts depending on filters and lamp settings. The average fluence rate calculation, used as a measure for illumination, scales well with source power, and efficiency of the source will not change. Therefore, with a consistent source power of 1 mW, the results for changing source power are easily predictable. As an estimation, if we were to operate at the American National Standards Institute (ANSI) standard for maximum permissible exposure (MPE) for a collimated beam on skin, the source power would scale by this value relative to the area of incidence of the source on the tissue. The smaller area of incidence of the internal source therefore requires a lower power than the external source to fall below the ANSI standard. While neither source is actually collimated, we are using these values to demonstrate the scalability of this model. Table 21 shows these values with the internal source in contact with the tissue and the external source incident on the cylindrical model, creating the largest difference in source power achievable while normalizing irradiance to the ANSI standard. The external source power becomes 1000x greater than the internal power. The corresponding average fluence rates for external illumination (Table 19) become roughly an order of magnitude higher than for internal illumination. However, as explained below, experimental limitations do not allow the external source to reach the same irradiance level as the internal source. If operation at the same irradiance levels was possible in the experimental setup, the efficiency rates and spatial distribution of light in the lung would remain poor for external illumination.

Table 21. Values relating source power in the simulations to ANSI standards for MPE of a collimated laser beam on skin for the wavelengths of interest.

Area of incidence	
<i>Internal source in contact with tissue</i>	0.342 mm ²
<i>External source</i>	400 mm ²
535 nm	
<i>MPE for skin</i>	2.00 mW/mm ²
<i>Internal source power</i>	0.68 mW
<i>External source power</i>	0.68 W
730 nm	
<i>MPE for skin</i>	7.96 mW/mm ²
<i>Internal source power</i>	2.7 mW
<i>External source power</i>	2.7 W

Specifically for our application, the external source in the whole animal imaging system at the highest setting is roughly 3-8 mW, depending on the spectral filtering. This power is evenly distributed over the entire platform at the base of the chamber (~3500 cm²),¹⁴⁴ and not over the surface of the animal (~400 mm²). A higher, yet still very safe, irradiance is achieved with the internal source, which operates at ~0.4-1.3 mW. This power is incident on a much smaller area than the external source (0.342 mm²). Using these values, the experimental irradiance ranges from 9-24 μW/mm² for the external source and 1200-3800 μW/mm² for the internal source, which is between 2 and 3 orders of magnitude difference. As stated earlier, the external source power would have to be about 1000x greater than the internal source to achieve the same irradiance. The comparisons drawn in this paper with the two sources both at 1 mW of power are therefore on the appropriate scale for comparing to experimental data.

5.7 Summary

A three-dimensional Monte Carlo model of the mouse lung and torso has been developed to analyze the capabilities of different excitation sources to illuminate the lung. The model approximates the physiology of the mouse torso, and can simulate both internal and external

light sources. By isolating the lung tissue, the radiative transport within the lung has been compared across internal and external sources, and across modifications to the internal source. By optimizing the illumination of the lung with the computational model, the system will ideally be well-suited to detect infection of a range of bacterial loads, regardless of the localization of the infection within the lung. The results of these simulations do help to explain the 2-3 fold improvement of the detection threshold of bacterial load in previous experiments^{45, 83}. However, a full analysis of the limitations of fluorescence detection is planned by extrapolating this model to include fluorescent bacteria to estimate the effect of optimal illumination on fluorescence detection in various infection scenarios. The model indicates that the system is very sensitive to the placement of the internal source, a variable which is not easily controlled experimentally, and could change significantly between animals. However, slightly improved illumination of the lung can be achieved by increasing the divergence of the internal source, which is an instrumentation change that can more readily be applied to the system. Overall, the validated model approximates the physiology well, and can be used as a tool to help optimize the imaging system and animal imaging protocol for future experiments.

6. MODELING *IN VIVO* FLUORESCENCE DETECTION OF PATHOGENIC BACTERIA

6.1 *Expanding the illumination model to cover fluorescence phenomena*

We have previously modeled the illumination of the murine lung to understand and enhance widespread illumination to probe for infectious bacteria. The illumination model takes a mock murine torso with experimentally determined values and values from the literature for absorbing and scattering properties of mouse lung, heart, and bulk soft tissue^{51, 145}. The model was used to describe the distribution of 535 nm and 730 nm light within the lung using three different illumination methods: 1) external illumination from the ventral side of the animal, 2) external illumination from the dorsal side of the animal, and 3) intravital illumination of the lung through an intratracheal microendoscope source. The intravital source was also manipulated within the simulation to describe the sensitivity of widespread illumination to scope position, divergence angle of the fiber microendoscope bundle, and diffusion efficiency of a fiber diffuser tip. We were able to gain an understanding of the physiological limitations imposed on each illumination method and provide a clear description of how source placement can affect inter-animal variability in imaging experiments.

In this section, we take the information from the illumination model and test if the effects of the modeled source parameters translate to a better fluorescence signal or enhanced signal to noise ratio. We also examine placement of the internal source in more detail to determine if any correlation exists between internal source placement and fluorescence signal collected, which would indicate that the microendoscope camera signal could be a reliable guidance tool for

* Reprinted with permission from “A fluorescence model of the murine lung for optical detection of pathogenic bacteria” by Durkee, Madeleine S., Cirillo, Jeffrey D., Maitland, Kristen C., 2017. *Clinical and preclinical diagnostics*, Volume 10411 (2017), Copyright 2017 by International Society for Optics and Photonics.

optimal placement of the internal source. Finally, we predict the performance of this system in human children with different clinical presentations of TB.

6.2 Preliminary infection model and validation

Optical simulations of the lung were performed in LightTools (Synopsys Inc.). A solid model of a simplified three-dimensional branching structure was designed represent the trachea and bronchi of the lung. Optical properties of the tissue were based on *ex vivo* measurements of excised infected mouse lungs (Tables 2-3). For validation of the model, the simulation was completed using only these parameters for tissue properties. Alveoli, heart tissue, and bulk tissue were excluded in the validation.

An optical tissue phantom of the lung was created to validate the fluorescence model of the lung. The phantom was designed to have the same optical coefficients (absorption and reduced scattering) as *ex vivo* murine lung tissue. Small diameter nitinol wires were included in the molding process to allow fluorophores to be placed at known locations within the phantom. After curing, the wires were removed and replaced with capillary tubes of rhodamine b. The phantom was then imaged using internal and epi-illumination and external detection with the IVIS whole-animal imaging system. A corresponding simulation with identical parameters is shown in Figure 29. This validation demonstrates that the simulation can predict the fluorescence signal with epi-illumination within an error of less than 3%.

After validating the simulation with the optical phantom, the physiology of the mouse was more accurately approximated. A cylindrical torso model including the lung, heart and bulk tissue (soft tissue, skin, and fur) was used to depict the *in vivo* environment. Separating the torso model into distinct regions also allows for the distribution of fluorophore (bacteria) to be localized to one region, specifically the lung for this application. Simulated fluorophores

matched the excitation and emission spectra of tdTomato (ex: 535nm; em: 585nm)⁴⁵. The simulation is used to simulate murine infections with tdTomato-transfected BCG (bacillus Calmette-Guèrin), a strain derived by attenuation of *Mycobacterium tuberculosis var. bovis*.

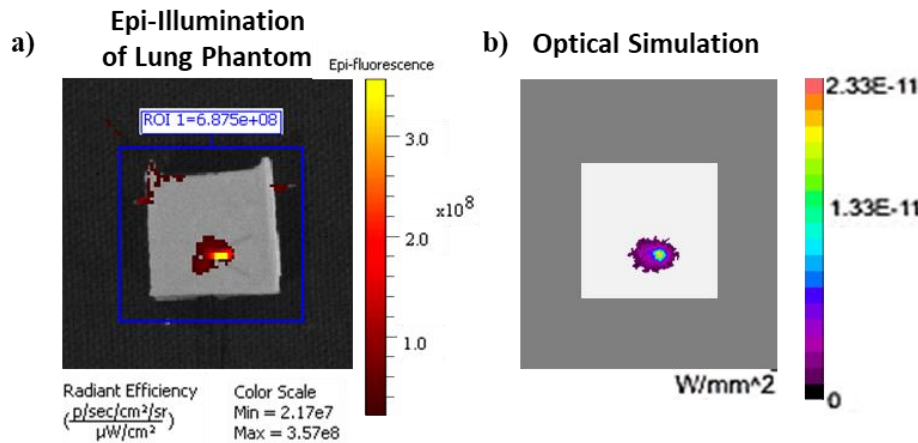


Figure 29. Validation of the fluorescence simulation. A) The IVIS image of the optical phantom shows the fluorescing capillary tubes emerging from the phantom. B) The optical simulations shows a very similar fluorescence distribution, with a percent error in radiant efficiency of only 2.36%.

Infections of bacterial loads ranging from 10^0 - 10^7 colony forming units (CFU) were simulated to determine the capabilities of the combined intra-vital illumination and small animal imaging system. A single CFU was estimated to contain 1000 tdTomato molecules. To predict the detection threshold of the optical system, the simulations represent the bacteria as being evenly distributed throughout the lung for each level of infection.

Based on this uniform infection simulation, the level of detection for the optical system with internal illumination and external detection is roughly 2500 CFU (Figure 30). Once this threshold is reached, there is a linear relationship ($R^2 = 0.9994$) between the bacterial load and

the fluorescence signal from the simulated infection. The number of photons collected for bacterial loads below 10^5 is low, resulting in larger error and more uncertainty. However, these data indicate that the signal collected for the system is limited by physiological variables, such as tissue scattering and absorption. These results correspond with previous animal experiments with the system⁴⁵. Unlike the previous animal experiments, these simulations indicate a correlation with internal detection as well. It is possible that detection with the microendoscope is more sensitive to location of the bacteria within the lung, and this simplified model of a uniform spatial distribution of bacteria may not be sensitive to those differences in infection dynamics.

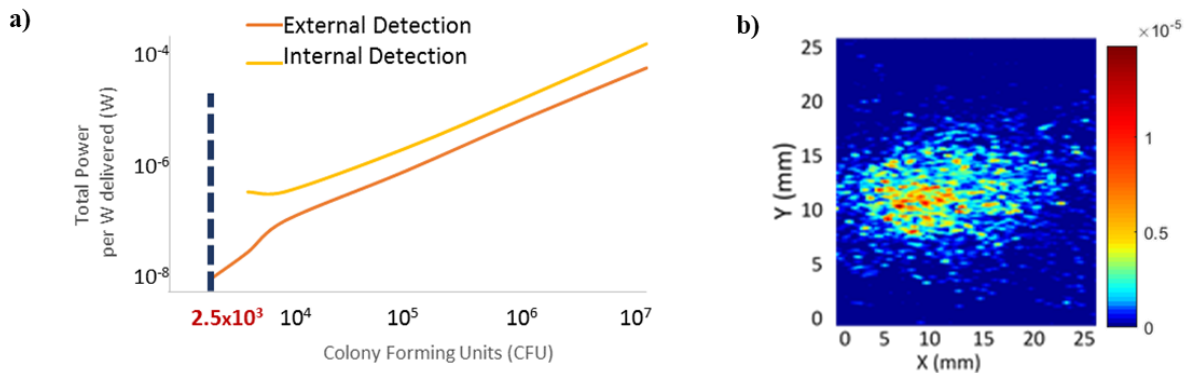


Figure 30. A) Fluorescence signal from model related to bacterial load. Simulations of infections below the level of detection are not shown for clarity. For an evenly distributed infection, signal is expected to be linearly related to bacterial load in this simplified model. B) A characteristic irradiance map of a high bacterial load simulation is shown to reference the spatial distribution of fluorescence signal.

Using this model that effectively retroactively validates the results from previous animal experiments, it is possible to test the effects of different light sources on sensitivity of the optical system, just as with the illumination model discussed in chapter 5. The first source tested was a

fiber diffuser. The diffuser was modeled to have the same diameter as the current scope with a length of 5 mm. The axial illumination of the diffuser was varied from 0% to 75% to view any effects on the bacterial signal (Figure 31a). While fluorescence is detected with all simulated diffusers, these results show a limitation of this model. The trachea is included in the lung layer, and is therefore part of the even distribution of fluorophores. This fluorescence signal detected on a plane that bisects the torso model is shown in Figure 31b. It is clear that the fluorescence signal is localized to the trachea and not the lung parenchyma, which is an unrealistic infection model.

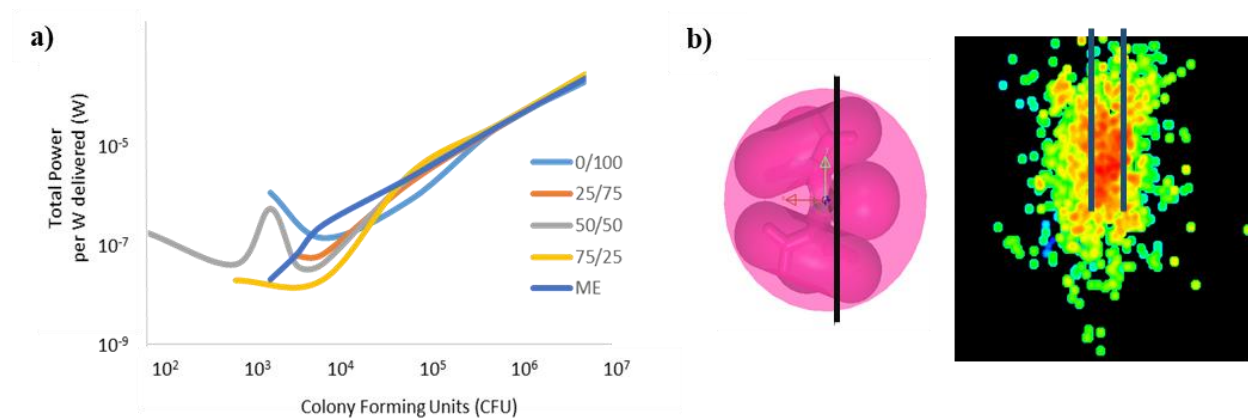


Figure 31. A) Predicted fluorescence signal after excitation with a fiber diffuser. The illumination profile of the fiber diffuser varies from 100% power coming from the tip of the diffuser (0/100) to only 25% reaching the tip, the remaining 75% of the power emitted from the length of the diffuser (75/25). ME: current microendoscope. B) Incident power density on a plane bisecting the torso model. The trachea is delineated in blue to show that fluorescence signal detected at lower CFU is in response to simulated bacteria residing in the trachea, and not the lung tissue.

The second change in source, just as in the illumination model, was manipulating the divergence angle of excitation light from the fiber microendoscope (Figure 32). Neither

sensitivity nor level of detection was improved by changing the fiber bundle divergence. While the illumination model, showed a statistically significant enhancement in power density of excitation light within the lung for larger divergence angles, the enhancement does not translate to the fluorescence model. The simulation shows that while the illumination of the lung was enhanced by these source manipulations, the effect does not translate to fluorescence. A larger divergence angle has no effect on system sensitivity over the current intra-vital illumination design.

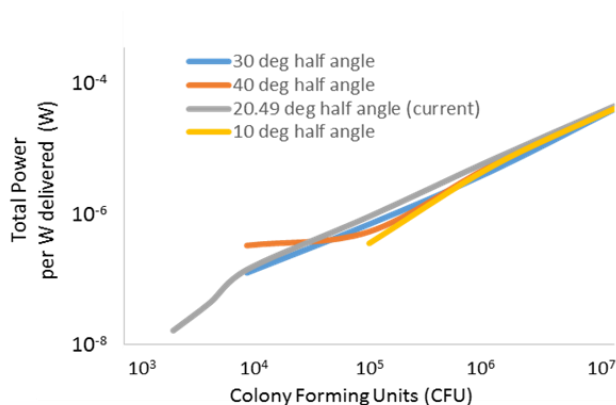


Figure 32. Predicted fluorescence signal collected after excitation with a fiber source of varying numerical aperture.

This preliminary model was able to retroactively validate previous animal imaging experiments, but there are still many limitations of the model. First, murine physiology can be better represented. In the next section, we discuss the addition of the airway surface liquid (ASL), a continuous lining of the airway that is hypothesized to improve delivery of light to more distal regions of the lung. Secondly, tissue autofluorescence (TAF) is very problematic for in vivo fluorescence detection, particularly in the visible wavelength range. Without TAF, all limitations come from the anatomical distribution of tissue absorption and scattering. Adding TAF will not only increase background, but the absorption of photons by the TAF molecules will

effectively increase the absorption coefficient of excitation light. However, it is difficult to elucidate the interplay between the excitation light, bacteria, and TAF excitation/emission without a more in depth model.

6.3 Improved replication of the murine anatomy: TAF and ASL

6.3.1 Improved representation of mouse torso anatomy

This simulation builds on the illumination model discussed in *Durkee et. al.*¹⁴⁶ and the preliminary fluorescence model¹⁴⁷. Briefly, the simulated mouse torso is composed of four compartments: bulk tissue, heart, lung, and a mucosal lining of the airway (ASL). The bulk tissue layer is representative of soft tissue, dermis, and epidermis. Fur is not accounted for in this model, but can be assumed to be a diffusing layer on the outer surface of the torso. Neglecting this effect, it can be assumed that this model slightly overestimates the fluorescence signal that is collected outside of the animal. The heart is modeled as a spherical organ with the optical properties of hemoglobin at a healthy (97%) oxygen saturation level.

6.3.2 Airway surface liquid

Anatomically, this model builds upon the previous models through the addition of the airway surface layer (ASL), a liquid layer lining the transport and respiratory airways in the lung^{99, 148, 149}. In the large scale branching structure, the ASL is modeled as a 100 micron-thick layer coating the inner surface of the airway (Figure 33a). At the alveolar level, the ASL is modeled with the multi-layer Mie scattering model discussed in chapter 4. Rather than modeling the alveoli as air-filled sacs inside of the tissue to determine an alveolar scattering coefficient as done in the illumination model, the alveoli are modeled as coated spheres with a 1 micron thick ASL shell. Similar to the previous model, the overall scattering and absorption coefficients are calculated from the measured tissue properties and the calculated alveolar scattering. Figure 33b-

33e show effect of this layer on the illumination of the lung. In these 100,000 photon simulations, the internal source was placed at the tracheal bifurcation, in contact with the ASL, (c&e), and offset within the airway (b&d). It is clear that the ASL has a “piping” effect on the illumination light when the source is in contact with this liquid layer. However, the overall power density of light within the lung is not significantly different when the source is offset from the ASL. The spatial distribution of light changes, but the overall power density of excitation light within the parenchyma does not. The ASL directs light deeper within the lung, resulting in an exponential decay outwards from the ASL, rather than outwards from the source location.

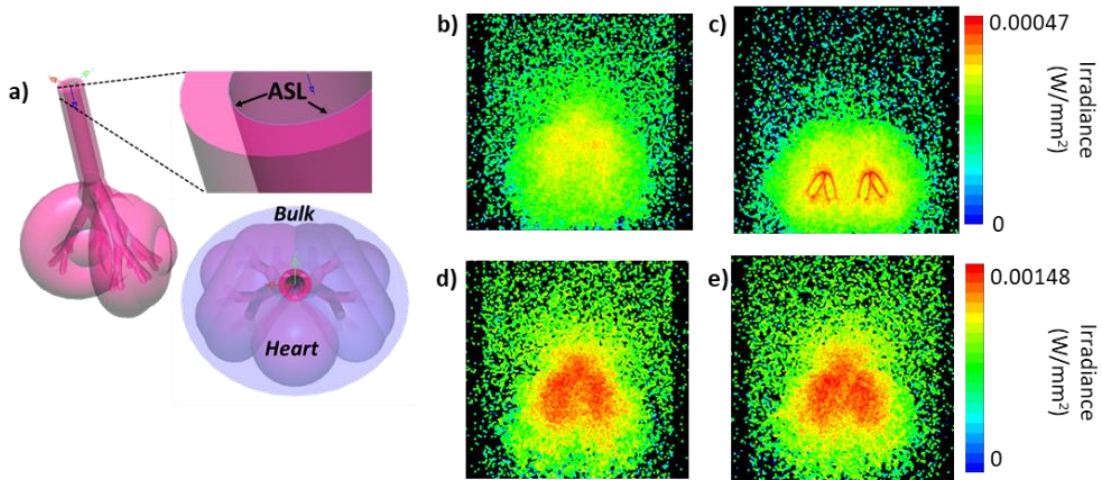


Figure 33. Effects of ASL on illumination. A) A 3D representation of the torso structure in the simulation. The ASL is noted on the inset. B-E) Illumination on a plane bisecting the lung layer of the phantom. Panels B&C show illumination with the ASL included in the model with the internal source offset (B) and in contact with the ASL. Panels D&E show illumination with no ASL modeled with the source offset (D) and in contact (E) with the tissue at the tracheal bifurcation.

6.3.3 Modeling tissue autofluorescence

In addition to the ASL, this model also includes tissue autofluorescence (TAF). Including TAF in this model is integral for determining the SNR of the integrated imaging system. A single population of fluorescent particles was used to approximate all sources of TAF in the torso

(Figure 34). The emission spectra at excitation wavelengths ranging from blue (480 nm) to NIR (800 nm) at 20 nm intervals, the conversion efficiencies, and the absorption cross sections at each of these excitation wavelengths were taken from values in the literature¹⁵⁰. Because up to 80% of the lung layer is actually modeled as air (due to the Mie scattering calculations), the concentration of TAF fluorophores in the lung layer was set to be one order of magnitude less than in the bulk layer.

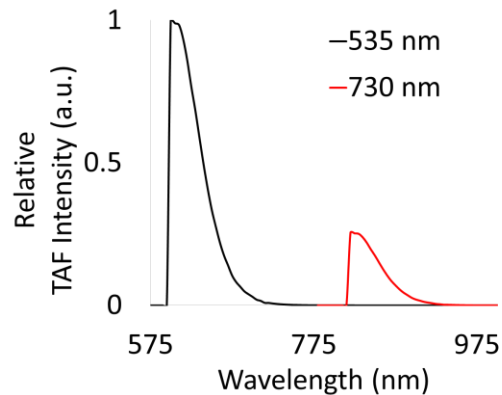


Figure 34. Simulated tissue autofluorescence spectra when the tissue is illuminated with 535 nm light (black) and 730 nm light (red). Spectra are normalized to the 535 nm TAF peak.

6.4 Spectral unmixing

The largest source of noise in *in vivo* detection of pathogenic bacteria is tissue autofluorescence (TAF)⁴⁵. Especially in the visible wavelength range, the endogenous molecules within the animal have a relatively high emission response to stimulation with visible light⁵². Spectral unmixing is a mathematical processing technique to separate the animal TAF from desired signal. In a radiative transport model, the spectra of the TAF and the fluorophore are both inputs to the model, and for our model, TAF is uniform throughout each layer. Assuming the collected signal is a linear combination of the TAF and bacterial fluorescence, we can separate the signal from each population of fluorophores.

In animal imaging experiments, a series of emission filters are used to collect signal along the spectrum of light emitted from the animal. Usually, 3-5 images are taken along the fluorescence spectrum. The variable intensity of these images is used to estimate the signal collected from TAF and the signal collected from fluorescence signal. Ideally, this normalizes the inter-animal TAF variability; however, the limited number of collection points and spectral overlap between fluorophores (especially in the tdTomato wavelength range) makes it difficult to achieve an accurate estimation of bacterial signal. Additionally, the emission spectra from a fluorophore—tdTomato for example—will have a red shift after traversing perfused tissue (Figure 35). With no a priori knowledge of the depth of this embedded fluorophore, it is difficult to isolate its spectrum for the unmixing process. In the computational model, we have a well-sampled tdTomato spectrum, and a simplified autofluorescence spectrum that does not vary between simulations (Figure 34). With these simplifications, we can still capture any interplay between the fluorophores, but can still analytically separate the spectral content collected.

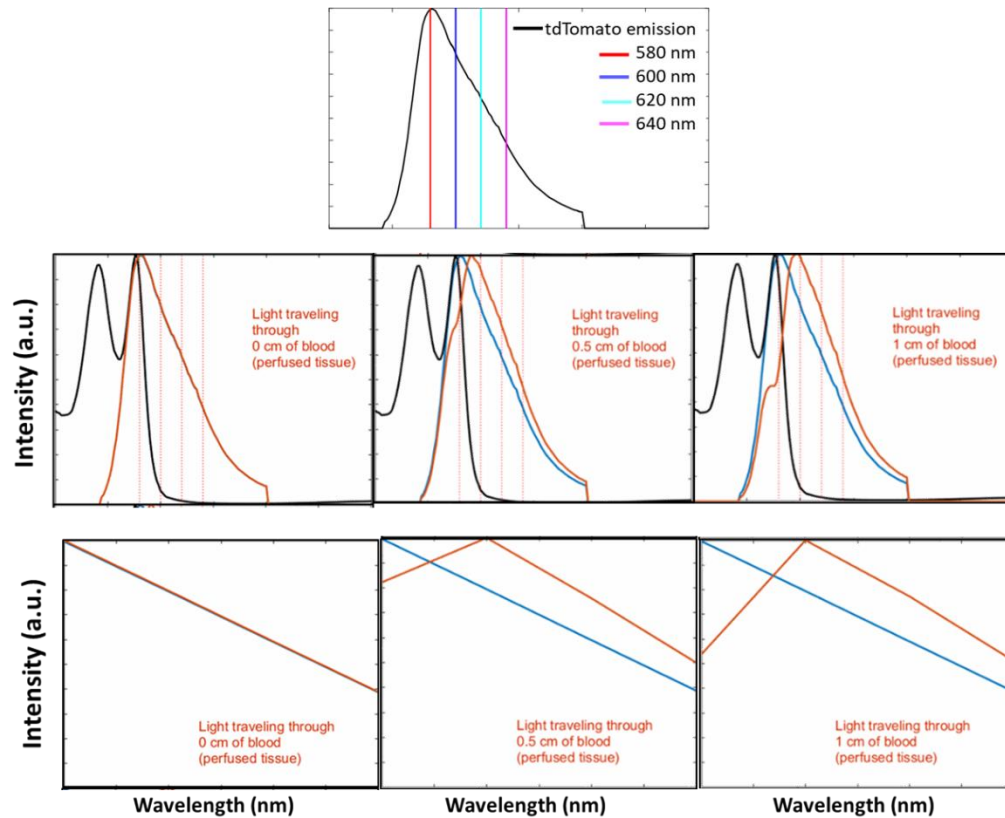


Figure 35. tdTomato fluorescence traversing perfused tissue. As emitted photons travel through perfused tissue, the higher energy photons are more likely to be absorbed by hemoglobin. The result is a red-shifted fluorescence spectrum. The peak of the resulting spectrum (orange) will continue to shift from the original spectrum (blue) as it travels through more tissue. When sampled at discrete spectral points the shape of the spectrum appears quite different.

6.5 Infection modeling in advanced murine torso model

The preliminary simulation of radiative transport simplified the mouse physiology and bacterial infection to isolate a few key variables related to the optical system. In this section, we expand on this model to better represent the murine physiology. We have improved the anatomical model of the mouse torso, improved the modeling of the optical properties of lung tissue, added a liquid lining to the airway, and modeled tissue autofluorescence. We have also

modeled fluorescence collection in both wavelength regions of interest: for detection of tdTomato fluorescent protein, and the bacteria-sensing fluorogenic probe.

6.5.1 Simulating fluorescence for tdTomato-transfected BCG and exogenous CNIR probe

As discussed earlier, we are modeling two different bacteria detection schemes: 1) tdTomato-transfected BCG and 2) an exogenous fluorogenic probe which is sensitive to the BCG/Mtb beta-lactamase enzyme (Figure 36). Because we do not have detailed information on the pharmacokinetics of the exogenous probe or the rate of conversion from the quenched to excitable state *in vivo*, we are assuming for this model that we are imaging at a post-administration time point and probe dose that is equivalent to the quantum yield of the transfected bacteria. With this assumption, the conversion rate of a photon reaching a bacterium is the same between the two detection schemes, and the difference in signal collection comes from the underlying radiative transport phenomena at the excitation and emission wavelengths. In animal experiments, the cleaved NIR probe has been shown to build up in the infected macrophages,^{39, 151} which would lead to a higher fluorescence for the same bacterial load. For simplification purposes, that effect is neglected in this optical model.

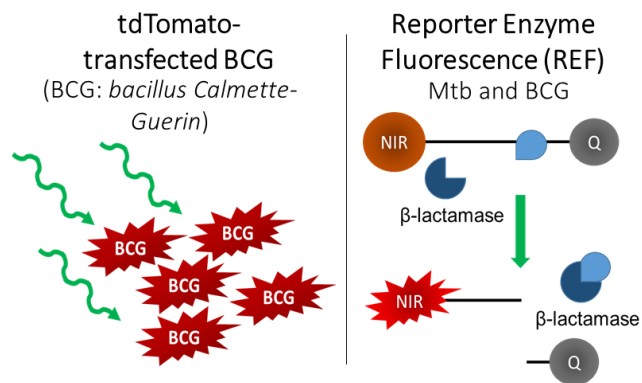


Figure 36. Different mechanisms for detection fluorescence from bacteria include genetic modification (left), and sensing with an external molecular beacon (right).

6.5.2 Modeling infection

6.5.2.1 Widespread infection

The simplest pulmonary infection model is a widespread infection model. In this model, each infectious dose (control- 10^7 CFU) is distributed evenly throughout the lung volume. Although the assumption of widespread infection is representative of late-stage, active TB, low doses were still modeled to estimate a detection threshold of the optical imaging system. Also, in mice at the time points imaged experimentally, there is not likely any isolation of bacteria. Within the model, fluorophores are defined as a single fluorescent molecule. However, transfected bacteria continually produces the fluorescent protein it is genetically modified to produce, so there is a baseline fluorescence level associated with 1 CFU¹⁵²⁻¹⁵⁴. For the widespread fluorescence model, this value is assumed to be 1000 molecules per bacterium.

In this fluorescence model of infection, we record total fluorescence signal at each wavelength, and mathematically unmix the TAF and bacterial signal. Placing the microendoscope in the same place in each animal is not only difficult, but impossible due to inter-animal anatomical variability. Additionally, in the previous illumination model¹⁴⁶, we showed that the illumination of the lung by the microendoscope was very dependent on source location. To more accurately represent the experimental procedure, we have modeled signal collection with “pseudo-random” placement of the microendoscope. This “pseudo-random” placement assumes that the experimentalist can have millimeter precision in placing the scope, and that the projection angle of the source can divert within roughly 5 degrees in any direction from the central axis of the animal.

Figure 37c-d shows the average unmixed bacterial signal with random source placement. The simulated fluorescence detected for this system varies with wavelength, animal position, and

illumination scheme. Table 22 compares the modeled detection thresholds for epi- and trans-illumination with the animal in ventral and dorsal positions for tdTomato and CNIR fluorophores. Simulations of infection with a bacterial load lower than 100 CFU show 0 photons from the tdTomato emission spectrum reaching the detector, with the exception of one epi-illumination trial, which is assumed to be a statistical anomaly due to the low (< 50) photon count on the simulated detector. We can assume that tissue absorption and scattering are the limiting factors in delivering of excitation photons to the bacteria and allowing transmission of emission photons outside of the body. For epi-illumination, the detection threshold was found to be position dependent, with dorsal illumination at both wavelengths showing roughly an order of magnitude decrease in detection threshold relative to ventral (Figure 37a). Trans-illumination was shown to be wavelength dependent, with the NIR probe yielding a lower detection threshold (Figure 37b). The detection threshold with internal illumination was also wavelength dependent, with collection from each position giving the same detection threshold (Figure 37c-d). A linear regression shows that collection in the dorsal position is more sensitive to CFU for epi- and internal illumination (Table 23). This indicates that a correlation between fluorescence signal and CFU is more likely to be achieved by imaging the mouse in the dorsal position. This model also shows a correlation between signal and CFU at the microendoscope tip (Figure 37c-d, Table 23), a result not found in past experiments. However, the data here is spectrally unmixed, and the current microendoscope design does not have multiple emission filters, so microendoscope detection does not currently have the capability of reaching this limit.

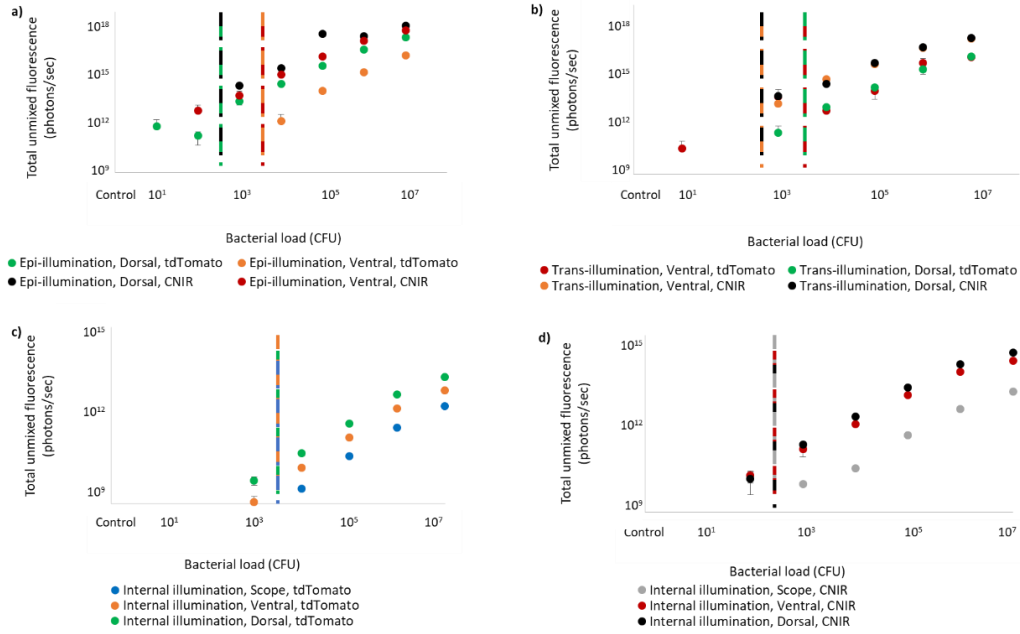


Figure 37. Unmixed tdTomato and CNIR probe fluorescence. A) For epi-illumination simulations, the unmixed detection threshold ranged from 10^2 - 10^4 CFU. Error bars represent the post-unmixing standard deviation with $n = 3$ simulations. B) Trans-illumination simulations showed a detection threshold of 10^3 CFU, which was not dependent on position. C-D) Internal illumination yielded a wavelength-dependent detection threshold at every collection position.

Table 22. Simulated detection thresholds for fluorescence detection are wavelength dependent after spectral unmixing for all internal and trans-illumination. The epi-illumination threshold is dependent on the positioning of the mouse.

<i>tdTomato</i>			
	Ventral	Dorsal	Scope
Epi-illumination	10^3 - 10^4	10^2 - 10^3	N/A
Trans-illumination	10^3 - 10^4	10^3 - 10^4	N/A
Internal illumination	10^3 - 10^4	10^3 - 10^4	10^3 - 10^4
<i>CNIR probe</i>			
	Ventral	Dorsal	Scope
Epi-illumination	10^3 - 10^4	10^2 - 10^3	N/A
Trans-illumination	10^2 - 10^3	10^2 - 10^3	N/A
Internal illumination	10^2 - 10^3	10^2 - 10^3	10^2 - 10^3

Table 23. Simulated fluorescence signal was linearly correlated with CFU. For epi- and internal illumination, the dorsal position was the most sensitive, while trans-illumination showed no position dependence.

	<i>Trans-illumination</i>			
	<u>tdTomato</u>		<u>CNIR</u>	
	Sensitivity ([photons/sec]/CFU)	R ²	Sensitivity ([photons/sec]/CFU)	R ²
<i>Dorsal</i>	2.00E+08	0.988	2.00E+09	0.9533
<i>Ventral</i>	2.00E+08	0.8275	2.00E+09	0.9553
	<i>Epi-illumination</i>			
	Sensitivity		Sensitivity	
	([photons/sec]/CFU)	R ²	([photons/sec]/CFU)	R ²
<i>Dorsal</i>	4.00E+09	0.988	2.00E+10	0.8655
<i>Ventral</i>	4.00E+08	0.9998	9.00E+09	0.9708
	<i>Internal illumination</i>			
	Sensitivity		Sensitivity	
	([photons/sec]/CFU)	R ²	([photons/sec]/CFU)	R ²
<i>Dorsal</i>	2.00E+06	0.9765	3.00E+07	0.9143
<i>Ventral</i>	7.00E+05	0.9788	1.00E+07	0.9732
<i>Scope</i>	2.00E+05	0.993	1.00E+06	0.9784

Because the internal source is also a microendoscope capable of collecting fluorescence, this microendoscope could potentially be used as feedback to the experimentalist to optimize source placement before taking images, given a correlation between the signal at the scope tip and the externally detected fluorescence. To test this theory, we compared the fluorescence collected at the fiber tip to dorsally collected fluorescence (Figure 38). The fluorescence recorded on the dorsal detector and the internal detector from each pseudo-random internal source location is shown for 10³ CFU in the tdTomato range (Figure 38a), and 10⁴ CFU in the NIR range (Figure 38b). No correlation was found between the internal and external source locations.

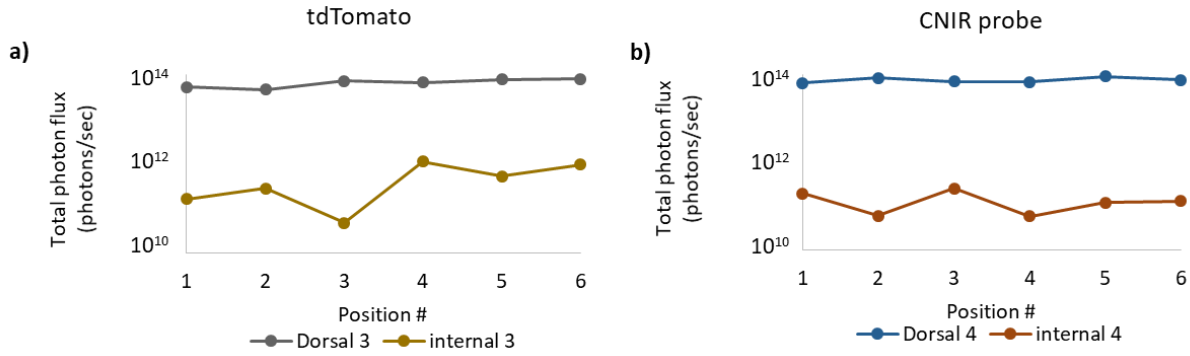


Figure 38. Signal at the microendoscope tip and dorsal collection for six different positions of the microendoscope. No correlation between microendoscope signal and dorsal fluorescence was found for tdTomato (A) or CNIR probe (B).

The illumination model showed an enhanced illumination for a higher divergence source¹⁴⁶. However, the preliminary fluorescence model showed no significant enhancement of signal with a higher divergence¹⁵⁵. To confirm this result, we also tested a source with a 40° divergence angle in this more advanced model. As with the internal illumination model with the 20.5° divergence source, we modeled the fluorescence detected with random source placement. Figure 39 shows that in most cases, there was no significant enhancement in the average fluorescence collected. The 40° source was significantly ($p < 0.005$) better at detecting 100 CFU in the NIR range. It was also shown to be significantly better than the 20.5° source for detection of 10⁴ CFU, specifically with ventral collection for tdTomato. However, the 20.5° source showed significantly better fluorescence detection ($p < 0.05$) for 10⁶ CFU in the ventral position in the NIR range. There was no consistent change in standard deviation across all groups between the 40° and the 20.5° source. This indicates that there is also no change in the robustness of the optical system with a higher divergence source because the inter-measurement variability is also not reduced.

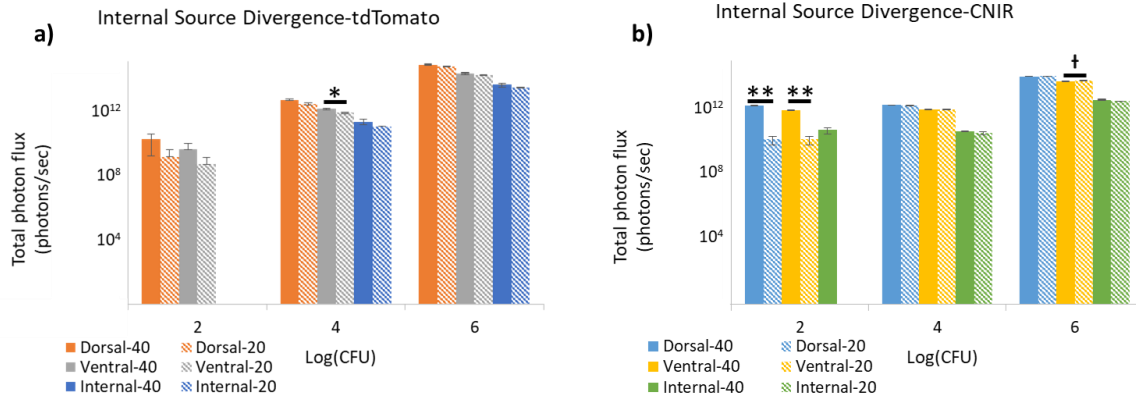


Figure 39. Simulated fluorescence signal with internal illumination sources of 20° and 40° divergence angles. Only ventral collection with 10⁴ CFU showed significant enhancement in the tdTomato range ($p < 0.05$) with increased divergence angle (A). Both dorsal and ventral collection with 10² CFU showed significant enhancement in the NIR range ($p < 0.05$) with increased divergence angle (B). However, there was also a significant decrease in fluorescence collection in the ventral position for 10⁶ CFU in the NIR range ($p < 0.05$).

6.5.2.2 Localized or cavitory infection: optical model of low bacterial loads

For the larger infectious doses, assuming an even distribution of molecules is a valid assumption because the bacteria are highly concentrated in the lung at those high doses (10⁴+ CFU). However, this is a poor assumption for lower numbers of bacteria. Therefore, we have also modeled the infection as a bolus of fluorescent particles. This can be thought of as a single lesion or granuloma containing multiple fluorescent bacteria. Not only does this better represent a low bacteria load, it also better represents the early stages of human pathogenesis, when Mtb is contained in by the immune system in a localized granuloma. Localizing the infection to a bolus of fluorescent particles allows us to analyze the sensitivity of the integrated imaging system to the location of the bacteria within the lung. We have modeled this bolus of infection to represent 10⁰-10³ CFU, and placed this “lesion” at five distinct points within the left lobe of the lung. None

of these locations or bacterial loads yielded a fluorescence signal statistically greater than control, indicating that the optical system is limited by tissue scattering at low bacteria loads. Without the ability to steer the endoscope deeper into the lungs, it is highly improbable that this system could get a high enough power density of excitation light to a cavitation or single CFU to produce a detectable signal.

6.6 Limitations of the infection model

The simulation of pulmonary infection supports results from previous animal experiments. Although the illumination simulation discussed in chapter 5 suggests that a higher divergence angle would improve illumination, this enhancement does not propagate to an improved threshold of detection for CFU in either the preliminary or advanced fluorescence models of infection. In this section we examine the limitations and assumptions of the fluorescence models, and discuss where these assumptions falter and how they might misrepresent *in vivo* infection.

The main limitation of the current model is the representation of anatomy. First, the mock torso does not have a fur layer. For internal illumination, this is not a very big concern, mainly because the illumination light is significantly attenuated by the time it reaches the outside of the animal. On the emission end of the process, the fur would act as a diffusing layer, mainly redirecting the emission light, but also absorbing and generating TAF. The redirection of the emission light will reduce overall signal collected and SNR, likely raising the detection threshold for bacteria. For external illumination, this fur layer would have a more significant effect. Illumination light would be reflected and scattered before entering the mouse, lowering the power density of excitation light reaching the lung. The attenuation of any resulting emission would be the same as the internal illumination case. The lack of this fur layer leads to a

discrepancy between the fluorescence model and previous experiments for both epi- and trans-illumination techniques. Figure 36 shows the detection threshold of epi- and trans-illumination to be comparable to internal illumination (Figure 36) and a signal correlation with CFU down to this limit, which disagrees with past experiments. It is possible that with ideal spectral unmixing, these external illumination methods could reach the values modeled, but the fur of the animal generates too much reflection and TAF for the bacteria signal to be pulled out. Essentially, by not modeling this fur layer, we are modeling a system with much less background noise than occurs during *in vivo* imaging experiments.

Another pitfall of this model is that it does not account for inter-animal variability. The simplified geometry is assumed to be close to the average mouse, but variability in airway branching, animal weight, and relative lung size would affect system performance. Also, some mice have a higher TAF. The model assumes the same TAF for each trial, which is not the case *in vivo*. If a mouse has a higher metabolism or is more stressed than the others in its cohort, it could have a vastly different TAF intensity, and even a different spectrum. TAF also varies across the animal. The ears, feet, and tail of the mouse have minimal fur, and yield a different TAF spectrum. In animal experiments, this makes spectral unmixing more difficult, because the spectrum used for unmixing does not necessarily fit for all pixels. For this model, we used a single fluorophore population to represent general TAF. This will again result in a reduction of the noise and background relative to animal imaging.

6.7 Summary of murine model of infection

We present results from an in-depth computational optical simulation of the mouse to investigate the performance of optical methods for detection of a pulmonary infection with Mtb. Retroactive validation with animal experiments demonstrate the accuracy of this fluorescence

model in replicating the results from animal experiments. Using the validated model, we can control physiological and system variables to better understand the interface between the optical system and the animal physiology. By controlling physiological variables and using a simplified TAF model, we were able to determine that tissue attenuation is the limiting factor for infectious doses below 100 CFU. We were also able to show that although the illumination model showed better illumination with a wider divergence angle at the endoscope tip, these results do not translate to fluorescence detection for either wavelength regime. The scattering-limited detection threshold for a mouse torso modeled without fur is between 10 and 100 CFU for internal illumination and external detection for the NIR, and between 100 and 1000 CFU for the Tomato spectral region. A linear correlation between fluorescence signal and CFU is shown for all detectable, post-spectral unmixing signals—regardless of animal position or illumination method. One limitation of the model suggests that these values might be underestimating the true values. As shown in Figure 33, the ASL acts as somewhat of a light guide for the excitation light. In an animal, this layer is continuous between the large scale airway and the alveoli, which may provide even more efficient coupling of light in and out of the lung parenchyma.

While none of the proposed manipulations of the internal source showed significant improvements across all bacterial loads, this model has been demonstrated as a readily available tool for feasibility testing of hypothetical enhancements. Based on the results from simulations so far, two changes can be recommended to enhance the imaging system. *1) Add more fluorescence filters to the microendoscope to allow for spectral unmixing.* The signal as the scope tip was shown to have a correlation with bacterial load after spectral unmixing, albeit with a higher detection threshold than external detection methods. *2) Add a second, spectrally separated illumination source to analyze TAF.* Figure 40 shows an interesting result with

illumination strategy and TAF. While external illumination yields a higher TAF signal with visible wavelengths, TAF signal collected is higher in the NIR with internal illumination. Also, table 24 shows that the relationship between TAF at a given wavelength is preserved across animal position rather than external illumination strategy (epi- v. trans-illumination).

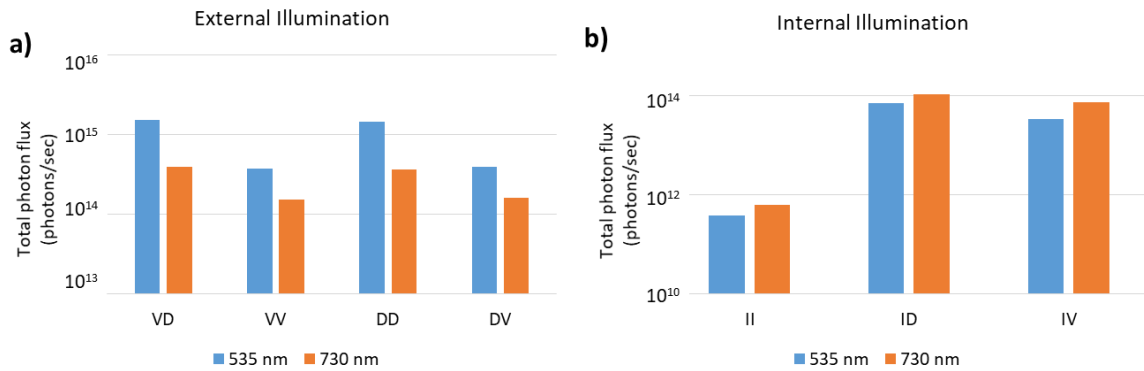


Figure 40. A) Tissue autofluorescence decreases at higher wavelengths for external illumination in any position (VD = ventral illumination with dorsal collection, VV = ventral illumination with ventral collection, DD = dorsal illumination with dorsal collection, DV = dorsal illumination with ventral collection). B) For internal illumination, an inverse trend in tissue autofluorescence signal is found. (II = internal illumination with internal collection, ID = internal illumination with dorsal collection, IV = internal illumination with ventral collection).

One of the simplifications of this model is that TAF is consistent throughout the torso and shows no regional dependence. Also, TAF intensity was not varied between trials. Animals show high variability in their TAF, between subjects and spatially within the same animal. Adding a secondary spectral illumination source would allow for a 2D TAF “map” for a given animal, which could be extrapolated to the spectral region of interest. Each animal could therefore serve as its own control, and spectral unmixing could better approach the theoretical limit. Fluorescence detection would become limited solely by tissue attenuation, and not by a high background (TAF) signal.

Table 24. Total TAF signal scales with wavelength at each position for external illumination. The trend does not hold for internal illumination.

	<i>730 nm TAF/535 nm TAF</i>		
	Ventral	Dorsal	Internal
<i>Trans-illumination</i>	0.409398	0.261786	--
<i>Epi-illumination</i>	0.405607	0.25142	--
<i>Internal illumination</i>	2.236976	1.548316	1.6532

6.8 Preliminary model of human anatomy: A clinical outlook

With a few broad assumptions, simulation of murine infection can be extrapolated to predict feasibility in human infants and young children. TB remains one of the deadliest childhood diseases, largely due to poor diagnostic tools. It is estimated that, although childhood TB represents 3.5% of reported TB cases, the true burden is closer to 11% of TB cases¹⁵⁶, but childhood TB is so underreported because it is so difficult to diagnose. Many rapid TB diagnostics rely on signals from the host immune system, indirectly determining if the patient has been exposed to the bacteria. However, young children—especially infants—have undeveloped immune systems, so their response to diagnostic tools and their disease progression vary from what is expected in adults. Because of this undeveloped immune response, infants are likely to progress to disease after the primary infection, and are very likely to succumb to disease.

6.8.1 Clinical presentations of childhood TB

TB manifestation in children can be very different than adults, making detection, diagnosis, and treatment more difficult (Figure 41). First, the limited immune systems of children do not form granulomas (also known as cavitory TB), making the radiographic evidence of TB different or nonexistent. Many childhood TB cases are paucibacillary, meaning they occur with a

small number of bacteria. This is problematic for two main reasons: 1) a lower bacterial load can still lead to late-stage illness, and 2) lower numbers of bacteria lead to an even lower sensitivity of detection methods. Because young children cannot expectorate, collection of a sample for culture is difficult. In sufficiently equipped medical facilities, gastric aspirations can be performed to get a culture sample. However, this method has been shown to have only a 15% sensitivity¹⁵⁷. Sputum can be induced from some children, which has a slight better sensitivity of about 40%¹⁵⁸. The physical disease progression is also different, as the infection in children tends to spread to the lymph nodes, with nearly 85% of childhood TB cases exhibiting lymphadenopathy, with 85% of lymphadenitis cases localized to the hilar lymph nodes^{157, 159}.

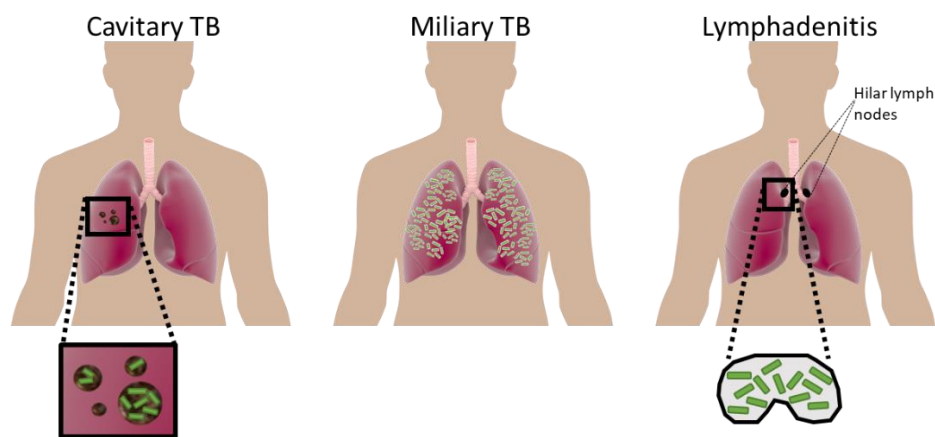


Figure 41. Clinical presentations of TB can vary. Adults usually exhibit cavitary TB, in which the bacteria reside in a focal lesion before reactivation and dissemination. Children more frequently present with miliary TB, a widespread, multifocal infection. Young children are also more susceptible to lymphadenitis of the hilar lymph nodes.

In addition to paucibacillary infections, children are more likely to develop miliary TB. While miliary cases make up < 2% of TB cases¹⁶⁰, 50% of miliary cases are in children¹⁶¹, with children also having a higher mortality rate¹⁶². Contrary to paucibacillary TB, miliary TB is associated with very high bacterial loads. The bacteria are encased in small (< 2 mm) “millet

seed” lesions disseminated throughout the lung and often also in extra-pulmonary sites^{4, 163}. These lesions have a much different radiographic presentation than cavitary TB, and often go unnoticed, with 50% of x-rays of miliary TB diagnosed as normal¹⁶⁴. Miliary TB is also a sputum-negative manifestation of TB, even in adults^{165, 166}, and the tuberculin skin test is negative in up to 50% of miliary cases. Because of this, miliary TB is often diagnosed through bronchoscopy and biopsy.

With bronchoscopy part of diagnostic practices, detection of miliary TB is the preliminary goal for optical detection of clinical cases of TB. We are specifically interested in diagnosis in children because of the limited number of sensitive and specific diagnostic tools for childhood TB. Also, the size of a child makes optical detection more feasible. As visible and NIR light has a relatively high attenuation by biological tissue, smaller subjects would be more ideal to achieve a better sensitivity. The illumination light will probe a larger percentage of the tissue, increasing the likelihood of detecting a miliary infection. Also, the tendency for lymphadenitis gives a defined region to probe for signal, and with the hilar nodes residing close to the bronchial tree, the infection becomes even more accessible by bronchoscopy. Here, we extrapolate our mouse model of infection to model infection in a human child. We increase the size of the modeled torso, change the optical properties of tissue, and change the source parameters to match that of a clinically used fluorescence endoscope probe. We model miliary TB as a widespread, high-dose infection, and lymphadenitis of the hilar lymph nodes with a range of bacterial infections.

6.8.2 Extrapolation of murine model to a human child

A young human child (< 5 years of age), has a total lung volume ranging from ~250 mL to ~1000 mL. For the purposes of this model, we assume a lung volume of 350 mL,

corresponding to the size of a young toddler (2-3 years of age)¹⁶⁷. Young children also have a higher density of smaller alveoli. To model the alveolar scattering for the human child model, we used an alveolar diameter of 80 μm , and a volume fraction of 70%. The concentric sphere model discussed in chapter 4 was used to estimate alveolar scattering, and the tissue absorption and scattering from mice was scaled to represent a 30% tissue volume. Bulk tissue and heart layers used the same optical properties as the mouse model. Assuming a chest circumference of 55 cm, the mouse model is scaled up by a factor of ~ 10 . The source power was increased to 25 mW, as the size of the clinical endoscope probe diameter (2 mm) is larger than the endoscope used in mouse experiments (0.66 mm). This larger area allows a higher power to be used while maintaining ANSI standard-safe irradiances at the probe tip. The miliary TB model of infection has a widespread distribution of fluorophores within the lung layer of the model, and the paucibacillary lymphadenitis model adds a hilar lymph node with fluorophores localized to the structure. Finally, because we are interested in diagnosis only for this model, we are only simulating infection in the NIR region. The assumptions for the pharmacokinetics of the CNIR fluorogenic probe are the same as discussed in section 6.5.1.

6.8.3 Miliary model of childhood TB

A miliary infection was modeled in the scaled-up model by distributing fluorophores evenly throughout the lung layer. Although many miliary TB cases disseminate to extrapulmonary infection, we are strictly modeling pulmonary infection. Also, because miliary TB is characterized by a very high bacterial load, we only simulated infections with bacterial loads ranging from 10^4 - 10^{12} CFU. The internal light source was placed in at the distal end of the second generation of the fractal tree airway model, near the apex of the right lung. All simulations modeled this single lobe illumination, although the bacterial load was distributed

throughout the entire lung region of the model. Figure 42 shows that with internal collection, the microendoscope can detect signal for bacterial loads greater than 10^6 CFU. The data is linearly correlated with an R^2 value of 1.

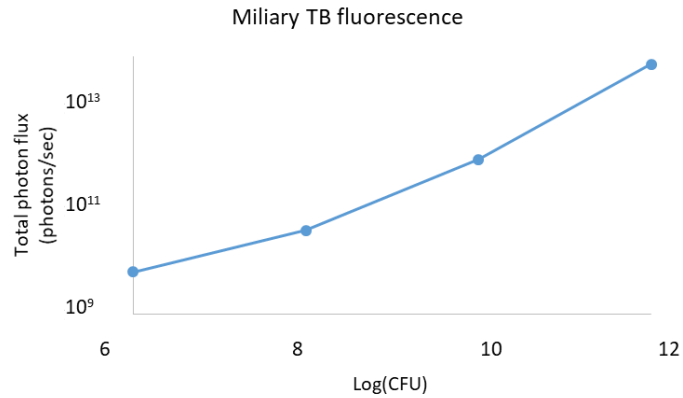


Figure 42. Simulated bacterial fluorescence in a child model of infection indicates that miliary TB in a child could be detected at doses higher than 10^6 CFU.

6.8.4 Lymphadenitis model of childhood TB

Previous simulations show that the optical system cannot detect very low levels of bacteria within the lung. However, if a paucibacillary infection were to cause lymphadenitis in the hilar lymph nodes, the localization of bacteria could allow for fluorescence detection of lower numbers of bacteria. Within this model, we place a spherical inclusion 4 mm in diameter near the apex of the lung, where the bronchus meets the parenchyma. The internal source is placed at the edge of the airway and directed at the simulated lymph node. Bacterial loads ranging from 0- 10^6 CFU, localized to the lymph node, were modeled. After unmixing, the minimum detectable bacterial load within the hilar lymph node was between 10^5 and 10^6 CFU.

6.8.5 Potential for optical diagnostic in children

Preliminary models show that the simulated fiber microendoscope could potentially serve as a diagnostic tool for childhood cases of miliary TB. However, it is unlikely that the device

will be able to detect paucibacillary infections, even in the case of lymphadenitis of the hilar lymph nodes. The current model assumes that the molecular probe associated with bacterial detection and fluorescence is roughly equivalent to fluorescence provided by genetically modified bacteria. However, previous studies indicate that the cleaved probe might remain within the infected macrophage with the bacteria for a period of time, serving as a molecular beacon for the bacteria. If this is the case *in vivo*, the buildup of this probe could result in signal amplification, which would enhance the detection threshold of the device, making it possible to detect lower numbers of bacteria. The radiative transport model indicates that it is possible to detect fluorescence with an internal source and detector, but the sensitivity of a translatable system will rely on the pharmacokinetics and signal amplification provided by the fluorogenic probe.

7. ENHANCEMENT OF LUMINESCENCE COLLECTION USING TURNING MIRRORS

7.1 Fluorescence detection of bacteria in vivo

Optical detection of pathogenic bacteria in animal models of disease is a powerful tool for longitudinal pathogenesis studies and therapy response trials. Bacterial infections of thoracic organs, such as pulmonary infections of Mtb, are more difficult to study because of the poor penetration of optical wavelengths in biological tissue. The optical attenuation of biological tissue limits both external and internal sources of excitation light and the collection of emitted photons from excited fluorophores¹⁴⁶. Previously, improving the optical detection threshold and sensitivity to CFU have been attempted through experiments and simulations by delivering the excitation light in a more efficient manner. *Nooshabadi et. al.* showed multiple orders of magnitude of enhancement by illuminating the animal with an internal excitation source rather than an external excitation source and a positional dependence on signal acquisition⁴¹. This enhancement minimized the path length of the excitation light, more efficiently delivering photons to fluorescent markers of bacteria within a live animal. However, the fluorescence signal from these internal excitation experiments is not always well correlated with bacterial load, and the threshold of detection is still two orders of magnitude higher than the infectious dose of Mtb.

We employ an external mirror platform to further improve fluorescence collection from the animal by collecting photons exiting the animal from multiple directions, increasing the number of photons collected. The mirror platform consists of two translatable 45° angled mirrors placed around the animal (Figure 43a, b). These mirrors will redirect light escaping the animal up to the external camera which would otherwise be undetectable (Figure 43c). Also, because the epi-illumination source of the IVIS is above the animal, the mirror platform should also improve

external illumination of the animal (Figure 43d). We use the fluorescence model discussed in earlier sections to predict the potential signal enhancement provided by this mirror platform, and use the platform to show signal enhancement in both phantom and animal imaging experiments.

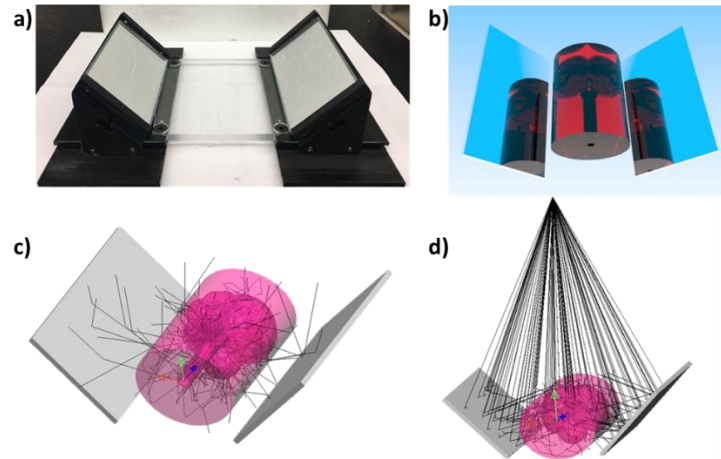


Figure 43. A) The mirror stage with 45° angled mirrors for use in the whole-animal imaging system. B) A photoreal rendering of the simulation in LightTools shows the multi-directional view provided by the mirrors. C) The mirrors are expected to enhance fluorescence collection from internal illumination experiments. D) The mirrors are also expected to provide multi-directional illumination in epi-illumination experiments.

7.2 Phantom validation of model and mirror stage

A commercial luminescence phantom (Xenogen) was simulated with LightTools to predict signal enhancement provided by the mirror platform. The phantom consists of an optically turbid elastomeric polymer molded into the shape of a mouse. Two LEDs are embedded in the phantom at different locations. The phantom was modeled as a scattering cylinder with the scattering and absorption coefficients used in the bulk tissue layer of the full-torso optical model discussed in chapter 5 (Figure 44a). Two monochromatic point sources (550 nm) were placed at the approximate locations of the LEDs within the phantom. The phantom was

simulated with and without the mirror platform under four conditions: 1) only LED A turned on, 2) only LED B turned on, 3) both LEDs turned on, and 4) both LEDs off. All simulations were run with $1e7$ photons. Figure 44b-d shows the total flux collected at the simulated external detector from the mirrors and the phantom. The simulated signal enhancement provided by the mirror platform ranges from 53-82% (Table 25).

Table 25. The simulations predict that the mirrors provide a signal enhancement ranging from 53-82%.

	Flux from Phantom [photons/second]	Flux from Phantom + Mirrors [photons/second]	% Difference
LED A	9.62E+12	1.66E+13	53.00
LED B	2.24E+12	5.37E+12	82.17
LED AB	1.19E+13	2.21E+13	60.09

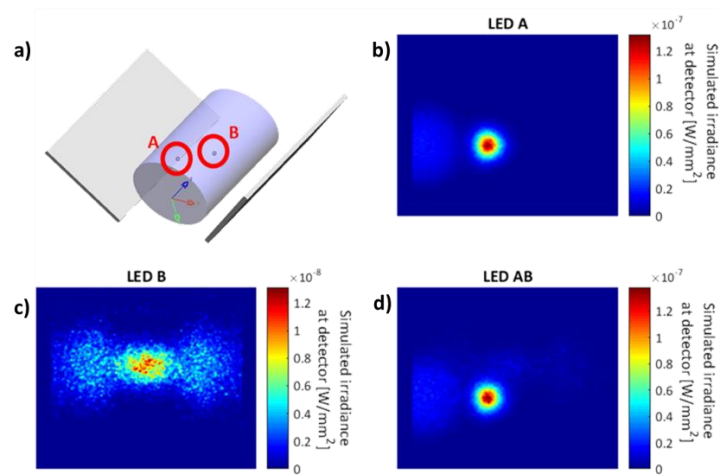


Figure 44. A) The simulated Xenogen phantom with two embedded LEDs (marked A and B) with angled mirrors. B) Predicted irradiance on the phantom and mirrors with only LED A turned on in the phantom. C) Predicted irradiance on the phantom and mirrors with only LED B turned on in the phantom. Note the image scale is one order of magnitude lower than panels B and D. D) Predicted irradiance on the phantom and mirrors with both LEDs turned on in the phantom.

To validate the model and the efficacy of the mirror platform, the Xenogen phantom was imaged using the IVIS Lumina II. The IVIS excitation source was blocked, and the emission filter set to open. The phantom was imaged as simulated: with and without the mirror platform under four conditions: 1) only LED A turned on, 2) only LED B turned on, 3) both LEDs turned on, and 4) both LEDs off (Figure 45). Five images were taken for each condition and averaged. The signal enhancement provided by the mirrors was similar to the modeled enhancement, ranging from 49-79% (Table 26). All signal enhancements were found to be statistically significant ($p \ll 0.0001$) (Figure 46).

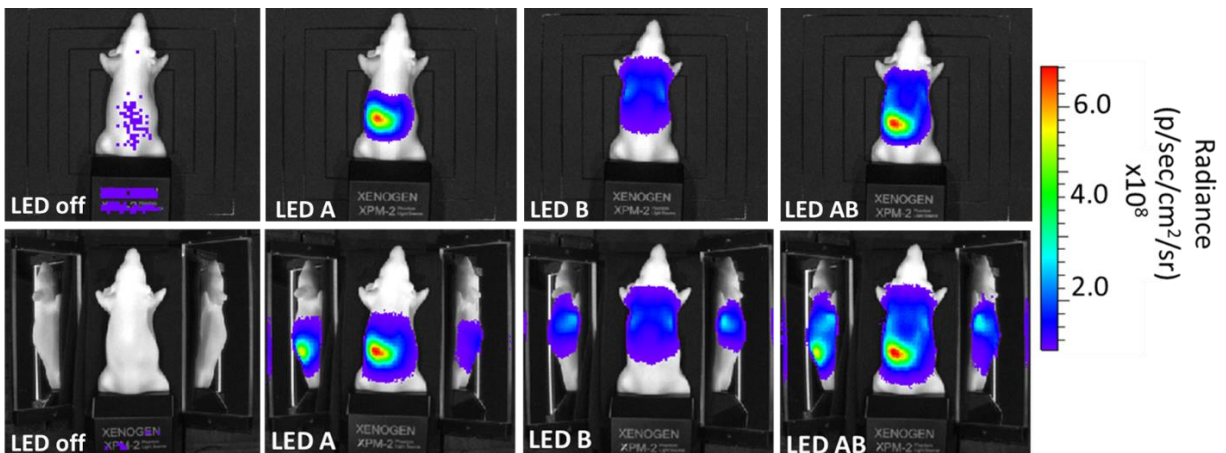


Figure 45. IVIS imaging of Xenogen phantom. The top row of images show the phantom imaged without the mirror stage. LED illumination is noted on each panel. A direct comparison can be made with the images of the phantom and mirrors below. For LED B imaged with the mirrors, the maximum signal is found on the mirrors.

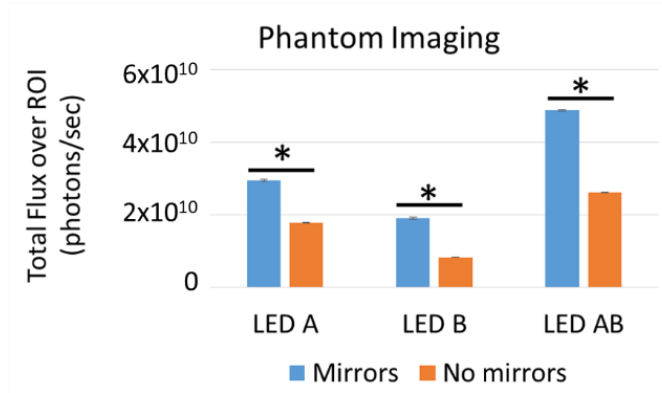


Figure 46. A statistical comparison shows that the mirrors provide a significant signal enhancement ($*p \ll 0.05$) for each source condition in the Xenogen phantom.

Table 26. The measured signal enhancement from the Xenogen phantom agrees well with the simulation, serving as a validation.

	Average Flux from Phantom [photons/second]	Average Flux from Phantom + Mirrors [photons/second]	% Difference
LED A	2.94E+10	1.77E+10	49.46
LED B	1.92E+10	8.31E+09	78.96
LED AB	4.88E+10	2.61E+10	60.58

The phantom fluorescence was also imaged to estimate the enhancement of epi-illumination in addition to the enhancement of signal collection (Figure 47). The IVIS illumination source was set to 465 nm, 500 nm, and 535 nm with the emission filter set to 580 nm to minimize leakage from the source. The phantom was again imaged with and without the mirror platform. For the experiments with the mirror platform, the photon flux was recorded from a region of interest (ROI) over just the phantom, or the phantom + the mirrors. A significant enhancement ($p \ll 0.005$) was found for both cases (Figure 48). For each spectral region, the enhancement over just the phantom was found to be ~45% (Table 27), indicating that the mirrors were providing multi-directional illumination, and generating more fluorescence

signal. Including signal collection from the mirrors, the total enhancement of fluorescence signal collection was ~100% for all illumination wavelengths.

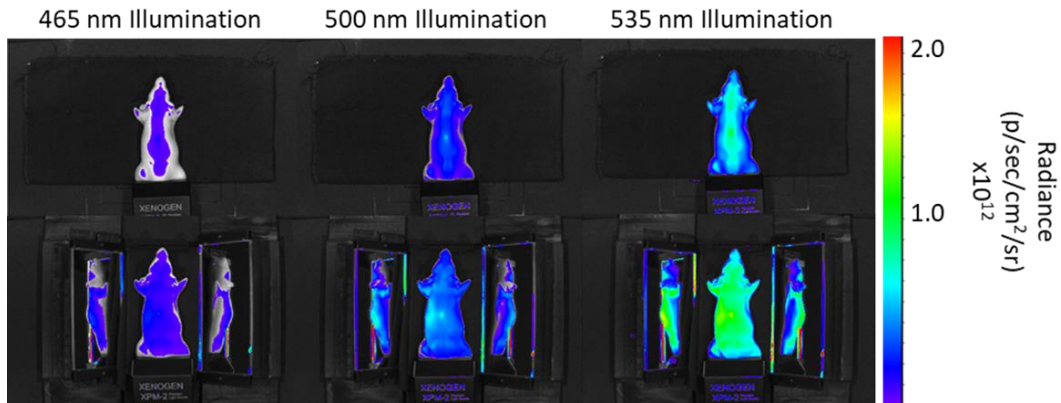


Figure 47. Fluorescence from the Xenogen phantom was measured with epi-illumination. The emission filter was held at 580 nm, and the source wavelength was shifted. The signal enhancement from the mirrors is a result of both multi-directional illumination and multi-directional fluorescence collection.

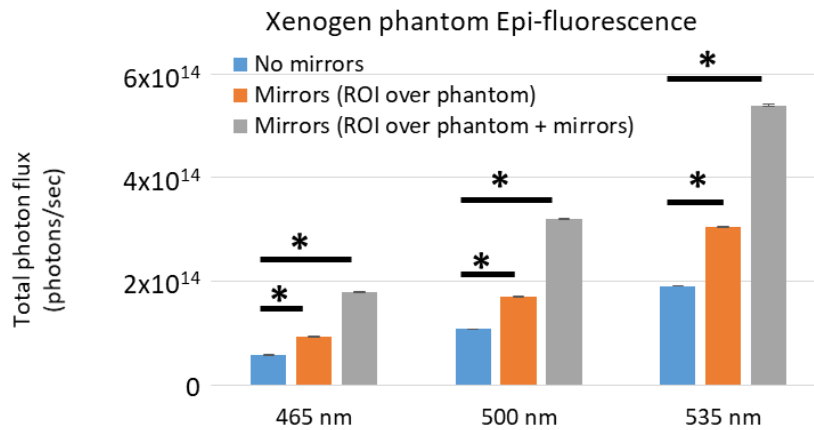


Figure 48. The multi-directional illumination is shown to enhance fluorescence signal. With the measured ROI covering only the phantom, and not the mirrors in the second row of images in figure 46, a statistically significant enhancement is still found (*p << 0.005).

Table 27. The measured signal enhancement from the multi-directional illumination provided by the mirror device is roughly 45% for every illumination wavelength. If the mirrors are included in the measurement ROI, the enhancement is measured to be ~ 100%.

	Average Total Flux (photons/sec)		
	465 nm	500 nm	535 nm
<i>ROI over phantom + mirrors</i>	1.80e14	3.20e14	5.40e14
<i>No mirrors</i>	5.85e13	1.08e14	1.91e14
% Difference	101.9 %	99.1%	98.2%
<i>ROI over phantom only</i>	9.31e13	1.71e14	3.04e14
<i>No mirrors</i>	5.85e13	1.08e14	1.91e14
% Difference	45.6%	45.2%	45.7%

7.3 Predicted performance with variable bacterial loads

After characterizing the mirror platform performance and validating the optical model of the mirrors with phantom imaging, the mouse torso model of infection was incorporated into the mirror model to predict the performance of the mirrors in a more complex sample. The mouse torso described in chapters 5-6 was used, including TAF and the ASL layer. Multiple variables were tested in the simulation. For each infectious dose (0, 10^2 , 10^4 , 10^6), fluorescence collection was simulated with and without the mirror platform, with internal and epi-illumination, with the mouse in ventral and dorsal positions (overall 8 different imaging conditions). For proof-of-concept animal experiments, we only used tdTomato-transfected BCG, with no CNIR fluorogenic probe. Therefore, fluorescence was only simulated in the visible wavelength range, with an excitation wavelength of 535 nm and emission collection at wavelengths greater than 580 nm. A single 106 photon count simulation was performed for each modeled CFU. Error for the total fluorescence collected was computed using Eq. 26, where σ is the variance at a given wavelength, and N is the number of photons reaching the detector in a given spectral bin.

$$error(\lambda) = \sigma/\sqrt{N} \quad (26)$$

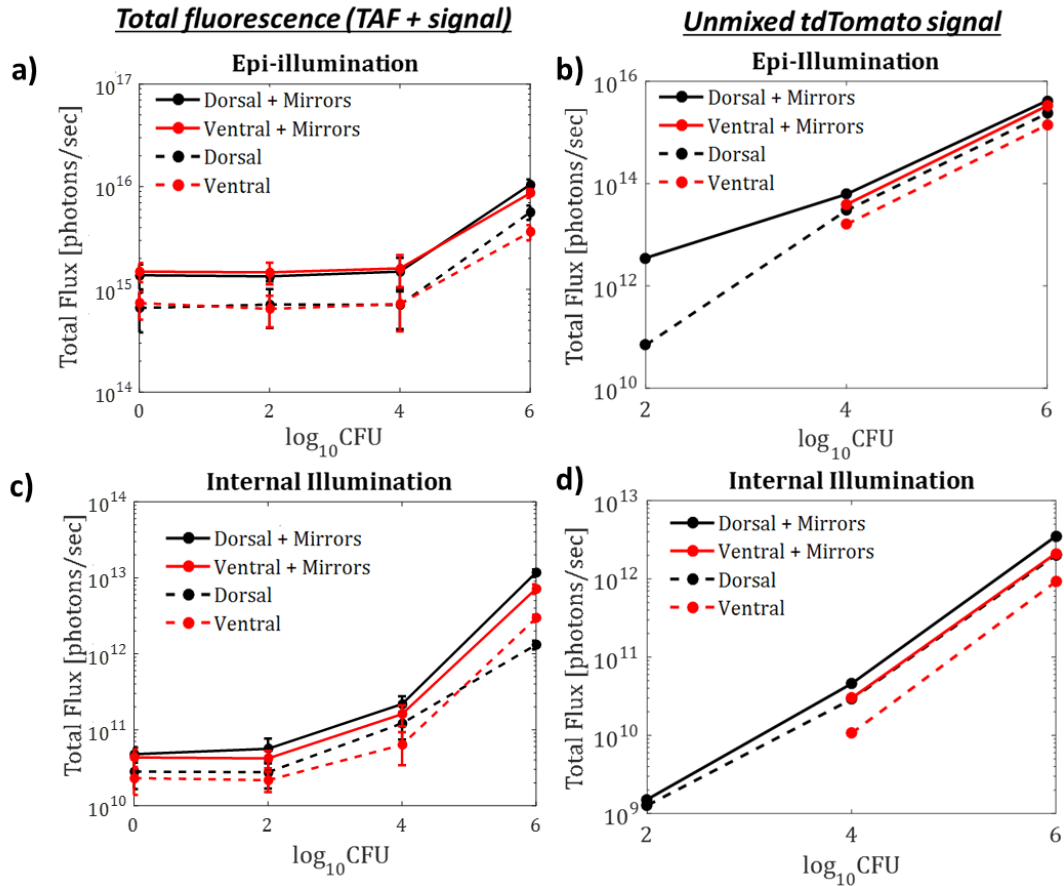


Figure 49. A) Total fluorescence signal collected from the simulated detector for epi-illumination is shown for the ventral and dorsal positions, with and without the mirror stage for CFU ranging from control to 10^6 . Error bars show average error in the simulation. NOTE: This error cannot be extrapolated to the unmixed data (B and D). B) The unmixed simulated fluorescence signal for epi-illumination shows the scattering-limited detection threshold. A signal enhancement from the mirrors is shown for both positions. C) Total simulated fluorescence signal for internal illumination is shown with ventral and dorsal collection, with and without the mirror stage. D) Unmixing the fluorescence signal shows the expected enhancement provided by the mirror platform for each CFU.

Figure 49 shows the predicted fluorescence signal for all 8 imaging conditions before and after spectral unmixing. Before spectral unmixing, only 10^6 CFU is different from control for all

epi-illumination simulations (Figure 49a). However, after spectral unmixing, dorsal collection with and without mirrors becomes significantly different from control at 10^2 CFU, and ventral collection becomes significantly different from control at 10^4 CFU (Figure 49b). Although internal illumination shows more difference from control pre-spectral unmixing, a similar trend with detection threshold emerges after spectral unmixing (Figure 49c-d).

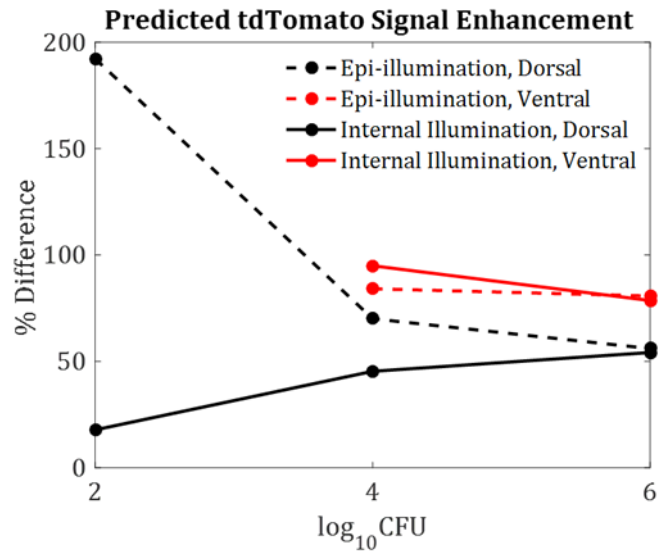


Figure 50. The predicted signal enhancement from the mirrors varies with CFU, animal position, and illumination method.

The simulated enhancement from the mirrors ranged from 18% to ~190% (Figure 50). However, this 190% enhancement of the mirrors with epi-illumination in the dorsal position is likely a factor of the low signal to noise ratio of the 10^2 CFU models. Just as with animal experiments, the TAF signal is much higher than the bacterial signal. Because these are stochastic simulations, the photon count from the bacteria is low for all of these simulations, especially for low CFU. The simulated signal enhancement by the mirrors is artificially high because the model likely underestimated the signal after spectral unmixing due to the low

number of photons in each spectral bin corresponding to tdTomato signal. Similar to animal experiments, the number of photons collected for these low bacterial loads is limited by tissue scattering and absorption, leading to higher variability and uncertainty in these simulations. While the simulation error remained low for total fluorescence detection (TAF + signal), the number of photons from the tdTomato fluorophore population was significantly lower, resulting in higher uncertainty in these simulations.

7.4 In vivo imaging of infection with turning mirrors for enhancement

7.4.1 Animal Experiments

Female BALB/C mice were separated into four different cohorts of three animals each. The control group was not infected with any bacteria, and each other cohort was anesthetized with a ketamine/xylazine mixture and intratracheally infected with a bacterial dose of 10^2 , 10^4 , or 10^6 CFU of *M. bovis* BCG transfected with a tdTomato vector. 24 hours after infection, mice were re-anesthetized and imaged with the IVIS Lumina II (PerkinElmer). Each mouse was imaged under 8 conditions: internal and epi-illumination in ventral and dorsal positions, with and without the mirror platform. To enable internal illumination, a 22G catheter (TERUMO Medical) was inserted into the trachea of the anesthetized mouse. Excitation light from 535 nm LED (Thorlabs) was launched into a 10,000-fiber bundle (Fujikura), which was threaded into the catheter as an intravital excitation source. Epi-illumination experiments used the IVIS illumination source, a 150 W Quartz Tungsten Halogen lamp (Schott) and a 535 nm excitation filter with a 35 nm FWHM. For all imaging experiments, three fluorescence images were taken with 20 nm bandwidth emission filters at 580 nm, 600 nm, and 620 nm. Each image was taken with an f-stop of 2 and automatic exposure time. After imaging, mice were sacrificed by injection of 100 μ L Fatal-Plus Solution (Vortech Pharmaceuticals Ltd.). The lungs were excised

and homogenized. Serial dilutions of the homogenized lung were plated on selective media to determine CFU. Animal use protocols were approved by the Texas A&M University Institutional Animal Care and Use Committee.

7.4.2 Spectral Unmixing

Manual spectral unmixing with Living Image software (Caliper Life Sciences) was used to separate TAF from tdTomato signal for each mouse in each imaging condition. A single control mouse was selected to collect the TAF spectra from, and a TAF spectrum was recorded for each of the following imaging conditions: 1) epi-illumination in the ventral position, 2) epi-illumination in the dorsal position, 3) internal illumination with ventral collection, and 4) internal illumination with dorsal collection. These TAF spectra were used for imaging experiments with and without mirrors. After loading the TAF spectra from the control mouse, the brightest pixel from the subject was selected from the merged image. The TAF spectrum was subtracted from the spectrum of that merged pixel to calculate a tdTomato spectrum. If there was not a relative maximum around 600 nm, as would be expected for tdTomato signal traveling through tissue (Figure 35), another pixel was selected. The software then unmixed the image pixel by pixel to separate the fluorescence overlay into tdTomato fluorescence and TAF. For all measurements, a measurement ROI was placed over the chest of the mouse, wide enough to cover both mirrors, even if there were no mirrors in that image. Total flux over the region of interest was used for statistical comparisons.

7.4.3 Signal enhancement with mirrors

For epi-illumination experiments, no bacterial load tested was found to be statistically different from control for ventral or dorsal, with or without mirrors (Figures 51-52). However, for most mice, the mirrors showed a 50-100% increase in tdTomato signal collected (Table 28).

In some cases, the spectral unmixing caused the tdTomato signal from the mirror experiments to drop below that of the experiments with no mirrors. Although the multi-directional illumination provided by the mirrors will provide more TAF fluorescence and more tdTomato fluorescence, it is hypothesized that there is a spectral unmixing error in these images. The percent enhancement is so high for most epi-illumination trials, that it is likely there was improper pixel selection for the spectral unmixing process in the images that yield a negative “enhancement”.

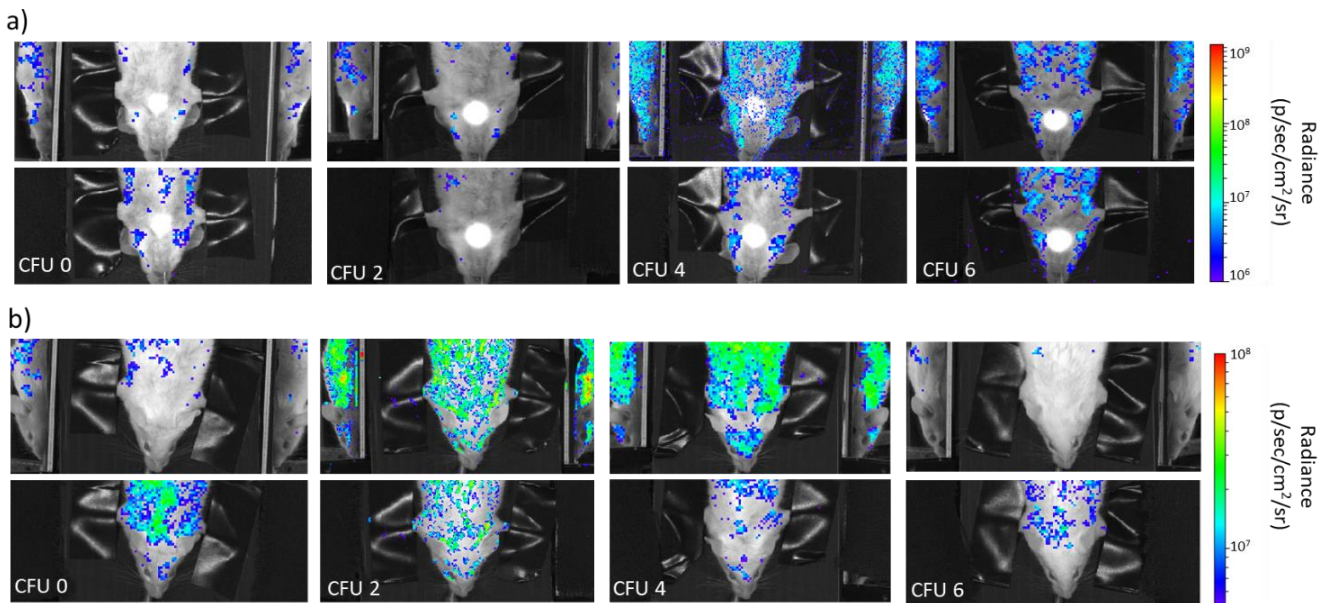


Figure 51. A) Representative spectrally unmixed images of mice imaged ventrally with epi-illumination at 0, 10², 10⁴, and 10⁶ CFU. The top and bottom images show the same mouse imaged with and without the mirror platform. B) Representative spectrally unmixed images of mice imaged dorsally with epi-illumination at 0, 10², 10⁴, and 10⁶ CFU. The top and bottom images show the same mouse imaged with and without the mirror platform.

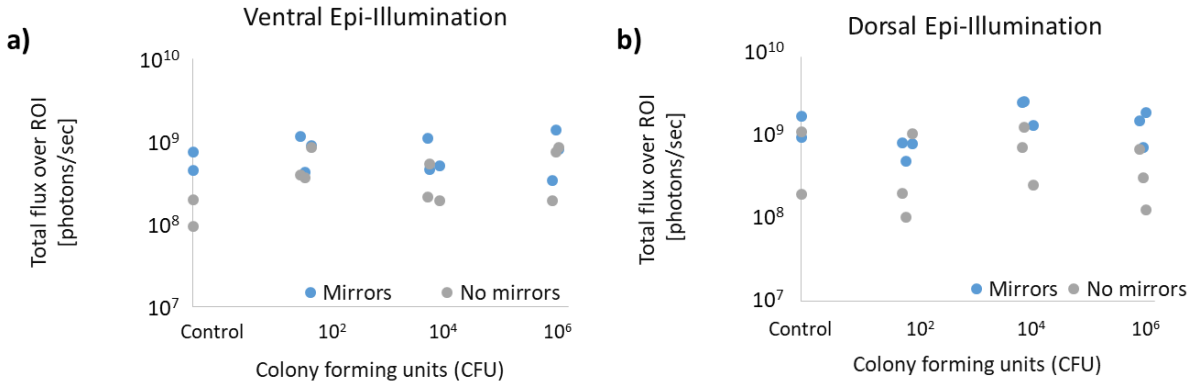


Figure 52. Spectrally unmixed data show no significant difference from control for any cohort, with or without the mirrors for ventral (A) or dorsal (B) epi-illumination experiments.

Internal illumination results showed a much more position-dependent enhancement. As shown by the representative results in Figure 53, qualitatively speaking, the mirrors do not direct much more signal to the camera than escapes off the ventral surface of the mouse. Contrarily, the fluorescence maximum for most dorsal images is actually located on one of the mirrors. Without the mirrors, only 10^6 CFU in the ventral position was found to be different than control (Figure 54). However, in adding the mirrors, 10^2 CFU and 10^6 CFU cohorts became higher than control in the dorsal position.

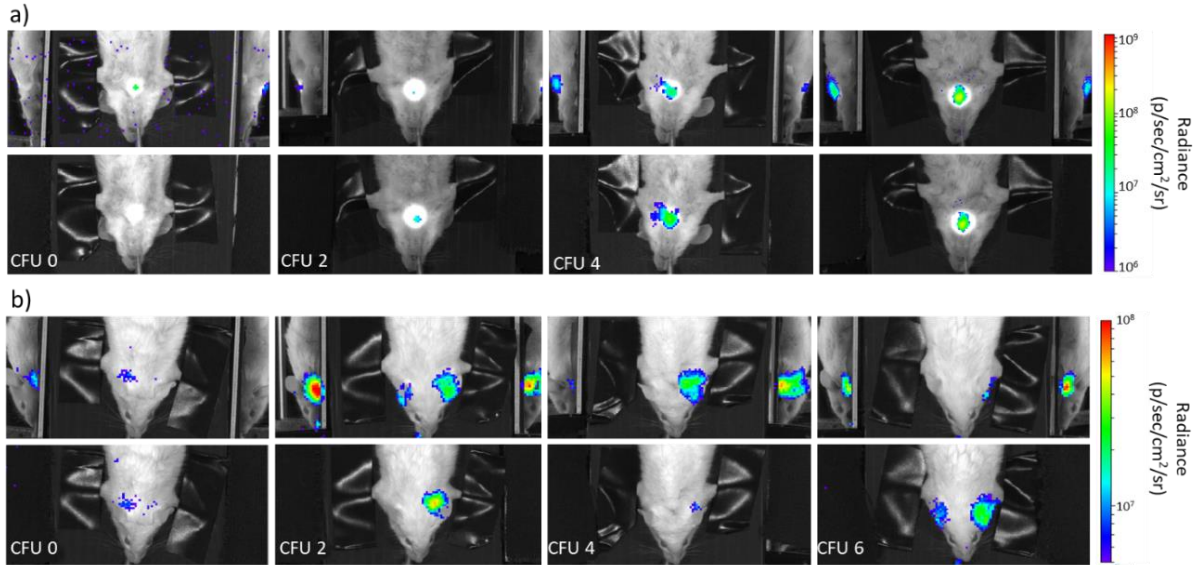


Figure 53. A) Representative spectrally unmixed images of mice imaged ventrally with internal illumination at 0, 10^2 , 10^4 , and 10^6 CFU. The top and bottom images show the same mouse imaged with and without the mirror platform. B) Representative spectrally unmixed images of mice imaged dorsally with internal illumination at 0, 10^2 , 10^4 , and 10^6 CFU. The top and bottom images show the same mouse imaged with and without the mirror platform.

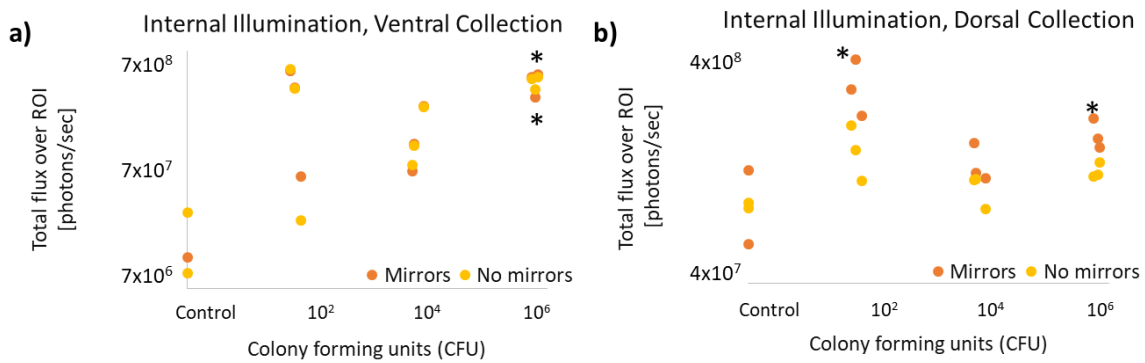


Figure 54. Spectrally unmixed data show a significant difference from control for only the 10^6 CFU cohort ($p < 0.05$), with and without the mirrors for internal illumination with ventral collection (A). For dorsal collection, no cohort without the mirrors is different from control. However, with mirrors, 10^2 and 10^6 CFU cohorts are significantly different from “control with mirrors” ($p < 0.05$).

Table 28. For an individual mouse, the mirrors usually provided a signal enhancement after spectral unmixing. Negative “enhancements” are bolded and italicized. These values are likely due to spectral unmixing errors. Average signal enhancement for each cohort is shown in the bottom section of the table.

Signal enhancement from mirrors (%)				
	Ventral Epi-illumination	Ventral Internal Illumination	Dorsal Epi-illumination	Dorsal Internal Illumination
<i>Control</i>	155.63	<i>-40.18</i>	42.39	<i>-35.97</i>
<i>Control</i>	77.90	<i>-86.68</i>	133.87	33.46
<i>100</i>	98.43	<i>-3.93</i>	121.78	36.23
<i>120</i>	15.01	1.57	132.16	85.90
<i>160</i>	4.17	86.55	<i>-29.67</i>	64.42
2.4×10^4	133.64	<i>-13.00</i>	112.56	37.21
4.0×10^4	88.65	1.37	136.27	31.30
2.6×10^4	<i>-13.86</i>	4.26	69.64	6.90
5.0×10^6	55.43	4.74	75.33	57.07
6.0×10^6	59.54	<i>-17.35</i>	81.53	36.69
6.6×10^6	<i>-4.11</i>	4.97	175.75	15.52
% Signal enhancement (average)				
log(CFU)	Epi-illumination, ventral	Internal Illumination, Ventral	Epi-illumination, Dorsal	Internal Illumination, Dorsal
<i>Control</i>	116.77	-63.43	88.13	-1.26
2	39.20	28.06	74.76	62.19
4	69.48	-2.46	106.15	25.14
6	36.95	-2.55	110.87	36.43

7.5 Summary

By adding angled mirrors to the whole-animal imaging system, we have improved fluorescence collection from an in vivo infection model. However, all phantom experiments and simulations show a much more significant signal enhancement than found with the animal experiments. We believe the primary reason for this discrepancy is the spectral unmixing errors. TAF and tdTomato emission have a large spectral overlap, and TAF intensity is much higher

than the signal from tdTomato for most bacterial loads. Also, as shown in Figure 55, the spatial dependence of TAF on a single mouse is a big issue. Unless the ideal pixel is selected, the sparsely sampled TAF spectrum can look nearly identical to the tdTomato emission spectrum. Pixel selection becomes extremely important in this situation. For these experiments, a blinded spectral unmixing analysis would provide a less biased, more reliable statistical comparison of the data. These animal experiments could also be improved with a TAF map of the animal. As discussed in section 6.7, a spectrally separate illumination source could be used to extrapolate the TAF of an individual mouse. The TAF map provided by this secondary source would make pixel selection for spectral unmixing a much more well-defined process.

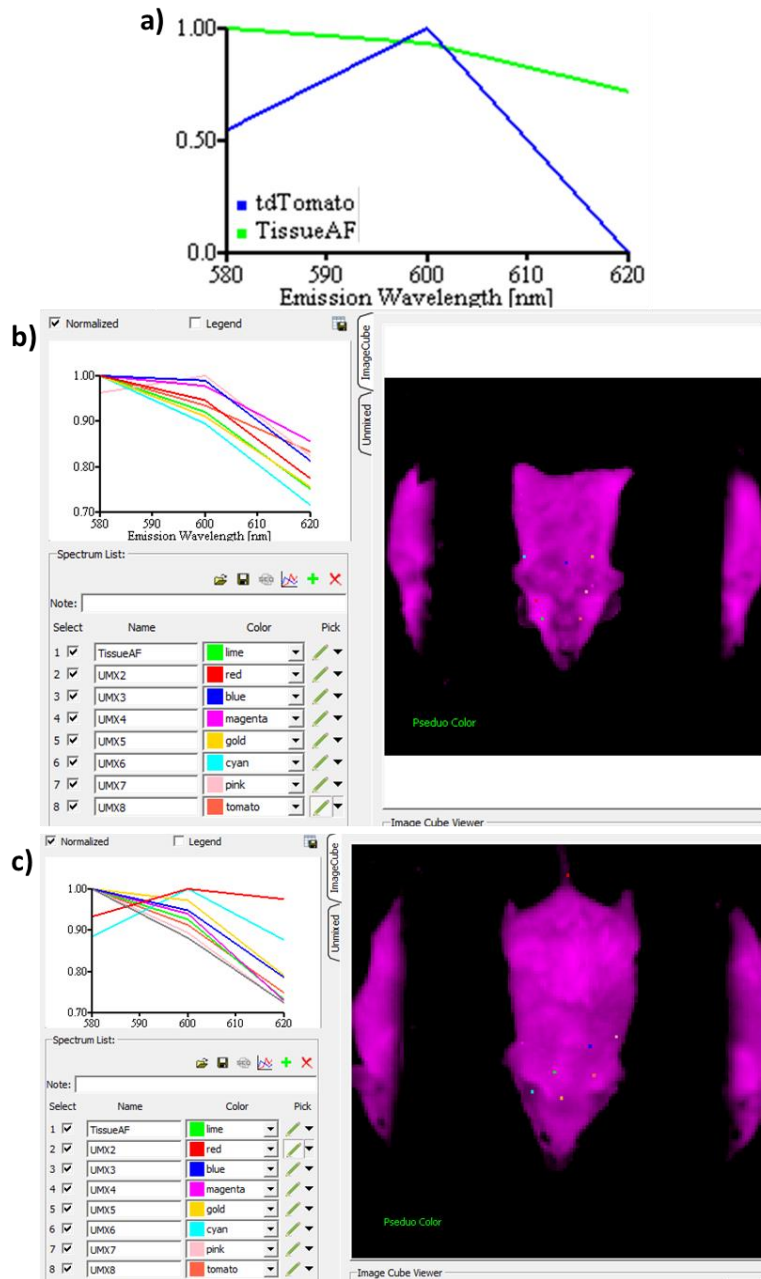


Figure 55. A) Example spectra of tdTomato and TAF spectra used for spectral unmixing for animal experiments. B) With a control mouse in the ventral position, the TAF spectrum varies spatially, with some spectra approaching the shape of the tdTomato spectrum. C) A control mouse in the ventral position also shows variable TAF spectra across the fluorescence overlay.

In closing, the mirror device is capable at further enhancing bacterial fluorescence collection, and even lowered the detection threshold of these experiments. A more controlled spectral unmixing process is expected to reduce the variability within animals for future experiments with and without the mirror platform.

8. CONCLUSION AND OUTLOOK

8.1 Pre-clinical applications: Improving optical detection

In vivo optical detection of pathogenic bacteria shows great potential as a tool for longitudinal pre-clinical studies of bacterial pathogenesis and therapeutic efficacy. In small animal models of disease, the optical path length of excitation and emission photons is reduced. This yields a more efficient delivery of excitation photons to fluorophores and a higher likelihood that the emitted photons will reach a detector. The physiological limitations that the optical system must overcome are tissue attenuation and low SNR due to TAF. Fortunately, the porous nature of the lung diffuses optical energy, increasing the probability that a photon will survive to excite a fluorophore. Here, we summarize the conclusions drawn from a computational model, and the implications that those have on using optical detection as a reliable tool for bacterial enumeration in longitudinal experiments.

8.1.1 Detecting tdTomato-transfected BCG

The most common model of optical detection of infection uses genetic modification of the bacteria, yielding a strain of bacteria that can produce an optical signal. We use tdTomato-transfected BCG for these experiments. The genetic modification of the bacteria allows a fluorescence signal to be generated from the bacteria themselves. With this model of infection, we know that any tdTomato fluorescence detected is localized to a live bacteria that is producing the tdTomato fluorescent protein. There is no time component associated with achieving optimal fluorescence, and the signal will always be spatially correlated with live bacteria. The major downfall of this method is the spectral range of tdTomato (530 nm – 600 nm). First, biological tissue has a fairly high attenuation coefficient in the spectral range of tdTomato excitation and emission. Hemoglobin absorption has a peak in this region, and the lung is a very well-perfused

organ, as it is responsible for blood oxygenation. Second, TAF has a similar spectral signature to tdTomato emission in this wavelength range. Both emission curves are decaying in this region after excitation with 535 nm light, making the two signals hard to spectrally unmix.

8.1.2 Detecting bacteria with a fluorogenic NIR probe

Unlike tdTomato-transfected bacteria, detecting bacteria with an exogenous NIR probe is not always localized to the bacteria. There is in vitro evidence that the probe remains localized to infected macrophages, but these results have yet to be proven in vivo. Also, the body naturally breaks down foreign substances and delivers them to the kidneys for clearing. This pharmacokinetic process is not fully defined for this probe. While we do have an idea about the optimal imaging time point after administration of the probe, the amount of broken down probe and its expected location within the body are less well-defined. The strengths of this method is that it potentially provides signal amplification, as a single bacterium can cleave multiple molecules of the fluorogenic probe. Exploitation of this catalytic activity is key to improving SNR with the optical system. Also, this bacteria-sensing probe is the main reason why this optical system could potentially be translated to a diagnostic tool. Wild-type bacteria seen in a clinical case will not be modified to produce a fluorescent protein, so it is necessary to have a molecular beacon-type sensing mechanism to determine whether or not bacteria are present. Also, simply by changing the spectral region of detection to the NIR, the detection threshold is improved by nearly an order of magnitude.

8.1.3 Potential improvements to device and protocol

Radiative transport modeling has shown that given complete spectral unmixing, the detection threshold of the optical system can reach between 10 and 1000 CFU depending on spectral region and animal position. An interesting result from the simulations suggest that the

TAF spectrum from internal illumination would actually increase with wavelength, rather than decrease as in external illumination experiments. This could be a contributing factor in the better performance of the internal illumination experiments. Not only is the excitation light being more efficiently delivered to the bacteria, but the high-intensity TAF becomes spectrally different from the bacterial signal and is spatially localized to similar tissues, meaning the same TAF spectrum will effectively unmix the entire fluorescence overlay.

To improve system performance in detecting bacteria in animal models, a few suggestions can be made. **1) *Manipulate the molecular markers used for detection.*** Red-shifting the fluorescence signal for genetically modified bacteria would improve the optical transport within biological tissue. For tdTomato-transfected BCG, the main limiting factors relate to the spectral region. The NIR probe is at a more ideal spectral region, but there is potential here for even higher sensitivity by exploiting chemical amplification methods of the exogenous probe to improve SNR. **2) *Illuminate the animal with a spectrally separated source for TAF mapping.*** TAF signal will be related when excited with two spectral bands. By illuminating with a light source that would not excite the bacteria, the spatial variability of TAF can be back-computed to the wavelength of interest. We suggest that this secondary light source be red-shifted from the bacterial excitation to minimize fluorophore cross-talk. Illuminating with a blue-shifted source could result in the TAF emission exciting the bacterial marker, which would contaminate a fluorescence signal meant to be used as a solely-TAF image for spectral unmixing. **3) *Add extra emission filters to the microendoscope.*** The microendoscope has not shown a signal correlation with CFU in previous animal experiments, but the simulations indicated that the physiology is not the limiting factor here. Just as with external detection, spectral unmixing of the microendoscope images could make internal detection more sensitive to CFU.

8.2 *Clinical implications: Potential diagnosis*

The secondary focus of the optical simulations was to help predict the performance of an optical diagnostic tool in children. Because young children, infants in particular, cannot expectorate³⁵, it is very difficult to achieve a sample for bacteriological isolation and confirmation of disease. Infants are also more likely to progress to active disease after the primary infection, and more likely to die from TB. Because of this, it is imperative that we develop more effective diagnostics for childhood TB, and get affected children effective treatment as early as possible. The optical system discussed in this dissertation has proven to be effective in sensing live bacteria in an animal model of disease, but not only do humans have different presentations of the disease, the fundamental light-tissue interactions are different, and something as simple as organism size can be highly limiting to the system performance. Because of the thickness of the human torso, even in infants and small children, internal illumination and fluorescence collection is the most likely method to achieve a signal from pulmonary bacteria.

Here, we have modeled two presentations of childhood TB, miliary TB and lymphadenitis. Although miliary TB is characterized by a high bacterial load, these bacteria are not usually present in the sputum, making traditional diagnostic methods ineffective at detecting the presence of Mtb. As shown by the optical simulations in chapter 6, it is very possible that a NIR system could detect miliary TB in a child the size of a toddler, a result that likely holds for a human infant. The model of lymphadenitis did not show as much potential in the simulation, but this could easily be due to the assumptions of the model. If the NIR probe truly does amplify the signal, lower numbers of bacteria within the hilar lymph nodes would provide a higher signal. To confirm this, experimental data on the NIR probe and bacterial load in human lymph nodes would be necessary to make more valid assumptions relative to this model of infection.

Overall, the preliminary optical simulations of human infection show potential for a diagnostic tool for childhood TB. The limitations and assumptions of the model are clear, and experimental data with humans is necessary to build a better model of infection before this device could be tested in children.

REFERENCES

1. W. H. Organization, "Global tuberculosis report 2016," (2016).
2. C. Dye, "Global epidemiology of tuberculosis," *The Lancet* **367**(9514), 938-940 (2006).
3. C. J. Cambier, S. Falkow, and L. Ramakrishnan, "Host Evasion and Exploitation Schemes of *Mycobacterium tuberculosis*," *Cell* **159**(7), 1497-1509 (2014).
4. A. Fanning, "Tuberculosis: 6. Extrapulmonary disease," *CMAJ: Canadian Medical Association Journal* **160**(11), 1597-1603 (1999).
5. J. G. Vallejo, L. T. Ong, and J. R. Starke, "Clinical Features, Diagnosis, and Treatment of Tuberculosis in Infants," *Pediatrics* **94**(1), 1 (1994).
6. R. M. Jasmer, P. Nahid, and P. C. Hopewell, "Latent Tuberculosis Infection," *New England Journal of Medicine* **347**(23), 1860-1866 (2002).
7. H. S. Schaaf, and A. Zumla, *Tuberculosis: A comprehensive clinical reference*, 1 ed., Elsevier (2009).
8. R. L. Riley, "Airborne infection," *The American Journal of Medicine* **57**(3), 466-475 (1974).
9. A. Rouillon, S. Perdrizet, and R. Parrot, "Transmission of tubercle bacilli: The effects of chemotherapy," *Tubercle* **57**(4), 275-299 (1976).
10. G. Sgaragli, and M. Frosini, "Human Tuberculosis I. Epidemiology, Diagnosis and Pathogenetic Mechanisms," *Curr Med Chem* **23**(25), 2836-2873 (2016).
11. A. S. Piatek et al., "Molecular beacon sequence analysis for detecting drug resistance in *Mycobacterium tuberculosis*," *Nature Biotechnology* **16**(359) (1998).

12. H. H. El-Hajj et al., "Detection of Rifampin Resistance in *Mycobacterium tuberculosis* in a Single Tube with Molecular Beacons," *Journal of Clinical Microbiology* **39**(11), 4131-4137 (2001).
13. W. A. Wells et al., "Alignment of new tuberculosis drug regimens and drug susceptibility testing: a framework for action," *The Lancet Infectious Diseases* **13**(5), 449-458 (2013).
14. C. Centers for Disease, and Prevention, "Extensively drug-resistant tuberculosis--United States, 1993-2006," *MMWR. Morbidity and mortality weekly report* **56**(11), 250 (2007).
15. Z. F. Udawadia et al., "Totally Drug-Resistant Tuberculosis in India," *Clinical Infectious Diseases* **54**(4), 579-581 (2012).
16. G. A. Colditz et al., "Efficacy of bcg vaccine in the prevention of tuberculosis: Meta-analysis of the published literature," *JAMA* **271**(9), 698-702 (1994).
17. J. A. M. Langermans et al., "Divergent effect of bacillus Calmette–Guérin (BCG) vaccination on *Mycobacterium tuberculosis* infection in highly related macaque species: Implications for primate models in tuberculosis vaccine research," *Proceedings of the National Academy of Sciences* **98**(20), 11497-11502 (2001).
18. D. G. Russell, C. E. Barry, and J. L. Flynn, "Tuberculosis: What We Don't Know Can, and Does, Hurt Us," *Science* **328**(5980), 852-856 (2010).
19. V. Balasubramanian et al., "Pathogenesis of tuberculosis: pathway to apical localization," *Tubercle and Lung Disease* **75**(3), 168-178 (1994).
20. D. G. Russell et al., "Foamy macrophages and the progression of the human tuberculosis granuloma," *Nature Immunology* **10**(943) (2009).
21. D. G. Russell et al., "The macrophage marches on its phagosome: dynamic assays of phagosome function," *Nature Reviews Immunology* **9**(594) (2009).

22. C. E. Barry et al., "The spectrum of latent tuberculosis: rethinking the biology and intervention strategies," *Nature Review Microbiology* **7**(12), 10 (2009).
23. N. K. Dutta, and P. C. Karakousis, "Latent Tuberculosis Infection: Myths, Models, and Molecular Mechanisms," *Microbiology and Molecular Biology Reviews* **78**(3), 343-371 (2014).
24. J. E. Gomez, and J. D. McKinney, "M. tuberculosis persistence, latency, and drug tolerance," *Tuberculosis* **84**(1), 29-44 (2004).
25. S. V. Capuano et al., "Experimental Mycobacterium tuberculosis Infection of Cynomolgus Macaques Closely Resembles the Various Manifestations of Human M. tuberculosis Infection," *Infection and Immunity* **71**(10), 5831-5844 (2003).
26. E. W. Tiemersma et al., "Natural History of Tuberculosis: Duration and Fatality of Untreated Pulmonary Tuberculosis in HIV Negative Patients: A Systematic Review," *PLOS ONE* **6**(4), e17601 (2011).
27. J. M. Davis, and L. Ramakrishnan, "The Role of the Granuloma in Expansion and Dissemination of Early Tuberculous Infection," *Cell* **136**(1), 37-49 (2009).
28. D. S. Ridley, and M. J. Ridley, "Rationale for the Histological Spectrum of Tuberculosis. a Basis for Classification," *Pathology* **19**(2), 186-192 (1987).
29. C. R. Shaler et al., "Within the Enemy's Camp: contribution of the granuloma to the dissemination, persistence and transmission of Mycobacterium tuberculosis," *Frontiers in Immunology* **4**(30) (2013).
30. N. Fogel, "Tuberculosis: A disease without boundaries," *Tuberculosis* **95**(5), 527-531 (2015).

31. J. Burrill et al., "Tuberculosis: A Radiologic Review," *RadioGraphics* **27**(5), 1255-1273 (2007).
32. L. Curvo-Semedo, L. Teixeira, and F. Caseiro-Alves, "Tuberculosis of the chest," *European Journal of Radiology* **55**(2), 158-172 (2005).
33. C. T. Sreeramareddy et al., "Time delays in diagnosis of pulmonary tuberculosis: a systematic review of literature," *BMC infectious diseases* **9**(1), 91 (2009).
34. P. Tucci, G. González-Sapienza, and M. Marin, "Pathogen-derived biomarkers for active tuberculosis diagnosis," *Frontiers in Microbiology* **5**(549) (2014).
35. D. S. Armstrong, "In Celebration of Expectorations," *American Journal of Respiratory and Critical Care Medicine* **168**(12), 1412-1413 (2003).
36. G. Manina, N. Dhar, and John D. McKinney, "Stress and Host Immunity Amplify Mycobacterium tuberculosis Phenotypic Heterogeneity and Induce Nongrowing Metabolically Active Forms," *Cell Host & Microbe* **17**(1), 32-46 (2015).
37. K. Andries, T. Gevers, and N. Lounis, "Bactericidal Potencies of New Regimens Are Not Predictive of Their Sterilizing Potencies in a Murine Model of Tuberculosis," *Antimicrobial Agents and Chemotherapy* **54**(11), 4540-4544 (2010).
38. A. Koul et al., "The challenge of new drug discovery for tuberculosis," *Nature* **469**(7331), 483-490 (2011).
39. H.-J. Yang et al., "Real-Time Imaging of Mycobacterium tuberculosis Using a Novel Near-Infrared Fluorescent Substrate," *Journal of Infectious Diseases* (2016).
40. Y. Kong et al., "Application of optical imaging to study of extrapulmonary spread by tuberculosis," *Tuberculosis* **89**(Supplement 1), S15-S17 (2009).

41. F. Nooshabadi et al., "Intravital excitation increases detection sensitivity for pulmonary tuberculosis by whole-body imaging with β -lactamase reporter enzyme fluorescence," *Journal of Biophotonics* (2016).
42. M. Baker, "Whole-animal imaging: The whole picture," *Nature* **463**(7283), 977-980 (2010).
43. F. Leblond et al., "Pre-clinical whole-body fluorescence imaging: Review of instruments, methods and applications," *Journal of photochemistry and photobiology B: Biology* **98**(1), 77-94 (2010).
44. H. Xie et al., "Rapid point-of-care detection of the tuberculosis pathogen using a BlaC-specific fluorogenic probe," *Nature chemistry* **4**(10), 802-809 (2012).
45. F. Nooshabadi et al., "Intravital fluorescence excitation in whole-animal optical imaging," *PLoS ONE* **11**(2), (2016).
46. J. N. Bixler et al., "Multi-scale fluorescence imaging of bacterial infections in animal models," *Photonic Therapeutics and Diagnostics IX* (2013).
47. C. F. Bohren, and D. R. Huffman, *Absorption and scattering of light by small particles*, John Wiley & Sons (2008).
48. V. Venugopalan, J. S. You, and B. J. Tromberg, "Radiative transport in the diffusion approximation: An extension for highly absorbing media and small source-detector separations," *Physical Review E* **58**(2), 2395-2407 (1998).
49. S. A. Carp, S. A. Prahl, and V. Venugopalan, "Radiative transport in the delta-P1 approximation: accuracy of fluence rate and optical penetration depth predictions in turbid semi-infinite media," *J Biomed Opt* **9**(3), 632-648 (2004).

50. S. L. Jacques, "Optical properties of biological tissues: a review," *Physics in Medicine and Biology* **58**(11), R37 (2013).
51. V. Tuchin, *Tissue Optics: Light Scattering Methods and Instruments for Medical Diagnostics*, 3 ed., SPIE, Bellingham, Washington, USA (2015).
52. M. Monici, "Cell and tissue autofluorescence research and diagnostic applications," *Biotechnology annual review* **11**(227-256 (2005).
53. L. V. Wang, and H.-i. Wu, *Biomedical optics: principles and imaging*, John Wiley & Sons (2012).
54. S. A. Prahl, M. J. C. van Gemert, and A. J. Welch, "Determining the optical properties of turbid media by using the adding-doubling method," *Appl. Opt.* **32**(4), 559-568 (1993).
55. J. Qu et al., "Optical properties of normal and carcinomatous bronchial tissue," *Appl Optics* **33**(31), 7397-7405 (1994).
56. L. Wang, S. L. Jacques, and L. Zheng, "MCML—Monte Carlo modeling of light transport in multi-layered tissues," *Computer Methods and Programs in Biomedicine* **47**(2), 131-146 (1995).
57. C. K. Hayakawa et al., "Perturbation Monte Carlo methods to solve inverse photon migration problems in heterogeneous tissues," *Optics Letters* **26**(17), 1335-1337 (2001).
58. I. Pavlova et al., "Monte Carlo model to describe depth selective fluorescence spectra of epithelial tissue: applications for diagnosis of oral precancer," *J Biomed Opt* **13**(6), 064012-064012-064013 (2008).
59. D. Arifler et al., "Spatially resolved reflectance spectroscopy for diagnosis of cervical precancer: Monte Carlo modeling and comparison to clinical measurements," *J Biomed Opt* **11**(6), 064027-064027-064016 (2006).

60. M. Keijzer, J. W. Pickering, and M. J. van Gemert, "Laser beam diameter for port wine stain treatment," *Lasers in surgery and medicine* **11**(6), 601-605 (1991).
61. Y. C. Huang et al., "Noninvasive blood flow imaging for real-time feedback during laser therapy of port wine stain birthmarks," *Lasers in surgery and medicine* **40**(3), 167-173 (2008).
62. B. W. Pogue, and M. S. Patterson, "Review of tissue simulating phantoms for optical spectroscopy, imaging and dosimetry," *J Biomed Opt* **11**(4), 041102-041102-041116 (2006).
63. A. Curatolo, B. F. Kennedy, and D. D. Sampson, "Structured three-dimensional optical phantom for optical coherence tomography," *Opt. Express* **19**(20), 19480-19485 (2011).
64. D. A. Miranda, K. L. Cristiano, and J. C. Gutiérrez, "Breast phantom for mammary tissue characterization by near infrared spectroscopy," *Journal of Physics: Conference Series* **466**(1), 012018 (2013).
65. M. Solomon et al., "Multimodal Fluorescence-Mediated Tomography and SPECT/CT for Small-Animal Imaging," *Journal of Nuclear Medicine* **54**(4), 639-646 (2013).
66. G. Wagnières et al., "An optical phantom with tissue-like properties in the visible for use in PDT and fluorescence spectroscopy," *Physics in Medicine & Biology* **42**(7), 1415 (1997).
67. N. Rajaram et al., "Non-Invasive, Simultaneous Quantification of Vascular Oxygenation and Glucose Uptake in Tissue," *PLoS ONE* **10**(1), e0117132 (2015).
68. M. J. Niedre, G. M. Turner, and V. Ntziachristos, "Time-resolved imaging of optical coefficients through murine chest cavities," *J Biomed Opt* **11**(6), 064017-064017-064017 (2006).

69. F. E. W. Schmidt et al., "Multiple-slice imaging of a tissue-equivalent phantom by use of time-resolved optical tomography," *Appl. Opt.* **39**(19), 3380-3387 (2000).
70. A. E. Cerussi et al., "Tissue phantoms in multicenter clinical trials for diffuse optical technologies," *Biomed. Opt. Express* **3**(5), 966-971 (2012).
71. N. M. Marín et al., "Calibration standards for multicenter clinical trials of fluorescence spectroscopy for in vivo diagnosis," *J Biomed Opt* **11**(1), 014010-014010-014014 (2006).
72. G. Alexandrakis, R. R. Fernando, and A. F. Chatziioannou, "Tomographic bioluminescence imaging by use of a combined optical-PET (OPET) system: a computer simulation feasibility study," *Physics in Medicine and Biology* **50**(17), 4225 (2005).
73. Q. Wan et al., "Monte Carlo modeling and phantom study for implantable fluorescent analyte sensors for human head," *Optical Diagnostics and Sensing VII* 64450J-64450J-64457 (2007).
74. C. Chen et al., "Preparation of a skin equivalent phantom with interior micron-scale vessel structures for optical imaging experiments," *Biomed. Opt. Express* **5**(9), 3140-3149 (2014).
75. M. S. Wróbel et al., "Use of optical skin phantoms for preclinical evaluation of laser efficiency for skin lesion therapy," *J Biomed Opt* **20**(8), 085003-085003 (2015).
76. R. Cubeddu et al., "A solid tissue phantom for photon migration studies," *Physics in Medicine and Biology* **42**(10), 1971 (1997).
77. Y. Bae et al., "Fabrication of a thin-layer solid optical tissue phantom by a spin-coating method: pilot study," *J Biomed Opt* **18**(2), 025006-025006 (2013).
78. J. Park et al., "Fabrication of double layer optical tissue phantom by spin coating method: mimicking epidermal and dermal layer," *Design and Performance Validaiton of*

- Phantoms Used in Conjunction with Optical Measurement of Tissue V 85830G-85830G-85836* (2013).
79. L. Luu et al., "Microfluidics based phantoms of superficial vascular network," *Biomed. Opt. Express* **3**(6), 1350-1364 (2012).
 80. A. I. Chen et al., "Multilayered tissue mimicking skin and vessel phantoms with tunable mechanical, optical, and acoustic properties," *Medical Physics* **43**(6Part1), 3117-3131 (2016).
 81. K. L. Lurie et al., "Three-dimensional, distendable bladder phantom for optical coherence tomography and white light cystoscopy," *J Biomed Opt* **19**(3), 036009-036009 (2014).
 82. A. Golabchi et al., "Refractive errors and corrections for OCT images in an inflated lung phantom," *Biomed. Opt. Express* **3**(5), 1101-1109 (2012).
 83. F. Nooshabadi et al., "Intravital excitation increases detection sensitivity for pulmonary tuberculosis by whole-body imaging with β -lactamase reporter enzyme fluorescence," *J Biophotonics* **10**(6-7), 821-829 (2017).
 84. G. J. Greening et al., "Characterization of thin poly(dimethylsiloxane)-based tissue-simulating phantoms with tunable reduced scattering and absorption coefficients at visible and near-infrared wavelengths," *J Biomed Opt* **19**(11), 115002 (2014).
 85. D. M. de Bruin et al., "Optical phantoms of varying geometry based on thin building blocks with controlled optical properties," *J Biomed Opt* **15**(2), 025001-025001-025010 (2010).
 86. S. Meissner et al., "Simultaneous three-dimensional optical coherence tomography and intravital microscopy for imaging subpleural pulmonary alveoli in isolated rabbit lungs," *J Biomed Opt* **14**(5), 054020-054020-054026 (2009).

87. A. H. Morris et al., "A new nuclear magnetic resonance property of lung," *Journal of Applied Physiology* **58**(3), 759-762 (1985).
88. K. Hearon et al., "Porous shape-memory polymers," *Polymer reviews* **53**(1), 41-75 (2013).
89. K. J. Chalut, M. G. Giacomelli, and A. Wax, "Application of Mie theory to assess structure of spheroidal scattering in backscattering geometries," *J Opt Soc Am A* **25**(8), 1866-1874 (2008).
90. A. L. Aden, and M. Kerker, "Scattering of Electromagnetic Waves from Two Concentric Spheres," *J Appl Phys* **22**(10), 1242-1246 (1951).
91. T. K. Jain et al., "Magnetic nanoparticles with dual functional properties: Drug delivery and magnetic resonance imaging," *Biomaterials* **29**(29), 4012-4021 (2008).
92. E. C. Dreaden et al., "The golden age: gold nanoparticles for biomedicine," *Chem Soc Rev* **41**(7), 2740-2779 (2012).
93. E. Prodan et al., "A Hybridization Model for the Plasmon Response of Complex Nanostructures," *Science* **302**(5644), 419 (2003).
94. P. K. Jain et al., "Calculated Absorption and Scattering Properties of Gold Nanoparticles of Different Size, Shape, and Composition: Applications in Biological Imaging and Biomedicine," *The Journal of Physical Chemistry B* **110**(14), 7238-7248 (2006).
95. J. Beek et al., "The optical properties of lung as a function of respiration," *Phys Med Biol* **42**(11), 2263 (1997).
96. R. H. Notter, *Lung Surfactants: Basic Science and Clinical Applications*, Marcel Dekker, Inc. (2000).

97. J. A. J. Vanoirbeek et al., "Noninvasive and Invasive Pulmonary Function in Mouse Models of Obstructive and Restrictive Respiratory Diseases," *Am J Resp Cell Mol* **42**(1), 96-104 (2010).
98. R. R. Mercer, M. L. Russell, and J. D. Crapo, "Alveolar septal structure in different species," *J Appl Physiol* **77**(3), 1060-1066 (1994).
99. H. Bachofen, and S. Schürch, "Alveolar surface forces and lung architecture," *Comp Biochem Phys A* **129**(1), 183-193 (2001).
100. S. E. Soutiere, C. G. Tankersley, and W. Mitzner, "Differences in alveolar size in inbred mouse strains," *Resp Physiol Neurobi* **140**(3), 283-291 (2004).
101. S. M. Tenney, and J. E. Remmers, "Comparative Quantitative Morphology of the Mammalian Lung: Diffusing Area," *Nature* **197**(54) (1963).
102. C. Mätzler, "MATLAB functions for Mie scattering and absorption, version 2," *IAP Res. Rep* **8**(1-26) (2002).
103. E. Fröhlich et al., "Measurements of Deposition, Lung Surface Area and Lung Fluid for Simulation of Inhaled Compounds," *Front Pharmacol* **7**(181) (2016).
104. E. R. Weibel, *Morphometry of the human lung*, Springer (1965).
105. K. E. Barrett et al., "Ganong's review of medical physiology. 23," *NY: McGraw-Hill Medical* (2009).
106. N. Wauthoz, and K. Amighi, "Formulation Strategies for Pulmonary Delivery of Poorly Soluble Drugs," in *Pulmonary Drug Delivery: Advances and Challenges*, p. 87, John Wiley & Sons (2015).
107. H. D. C. Smyth, and A. J. Hickey, *Controlled pulmonary drug delivery*, Springer (2011).

108. A. N. Bashkatov et al., "Optical properties of human skin, subcutaneous and mucous tissues in the wavelength range from 400 to 2000 nm," *J Phys D Appl Phys* **38**(15), 2543 (2005).
109. V. E. Calderon et al., "A Humanized Mouse Model of Tuberculosis," *PLOS ONE* **8**(5), e63331 (2013).
110. Y. Kong et al., "Whole-Body Imaging of Infection Using Fluorescence," *Current protocols in microbiology* 2C. 3.1-2C. 3.21 (2011).
111. E. A. Nardell, "Transmission and institutional infection control of tuberculosis," *CSH Perspect Med* **6**(2), a018192 (2016).
112. C. Zhu, and Q. Liu, "Review of Monte Carlo modeling of light transport in tissues," *BIOMEDO* **18**(5), (2013).
113. D. A. Boas et al., "Three dimensional Monte Carlo code for photon migration through complex heterogeneous media including the adult human head," *Opt. Express* **10**(3), 159-170 (2002).
114. Q. Fang, "Mesh-based Monte Carlo method using fast ray-tracing in Plücker coordinates," *Biomed. Opt. Express* **1**(1), 165-175 (2010).
115. H. Li et al., "A mouse optical simulation environment (MOSE) to investigate bioluminescent phenomena in the living mouse with the monte carlo method," *Academic Radiology* **11**(9), 1029-1038 (2004).
116. S. Ren et al., "Molecular Optical Simulation Environment (MOSE): A Platform for the Simulation of Light Propagation in Turbid Media," *PLOS ONE* **8**(4), e61304 (2013).
117. D. J. Smithies, and P. H. Butler, "Modelling the distribution of laser light in port-wine stains with the Monte Carlo method," *Physics in medicine and biology* **40**(5), 701 (1995).

118. T. J. Pfefer et al., "A three-dimensional modular adaptable grid numerical model for light propagation during laser irradiation of skin tissue," *IEEE Journal of Selected Topics in Quantum Electronics* **2**(4), 934-942 (1996).
119. H. Funamizu et al., "Simulation of spectral reflectances in human skin tissue using ray tracing and GPU-based Monte Carlo method," *OPT REV* **21**(3), 359-363 (2014).
120. C.-Y. Huang et al., "Novel Wearable and Wireless Ring-Type Pulse Oximeter with Multi-Detectors," *Sensors* **14**(9), (2014).
121. W. Hwang et al., "In Vitro Study of Transcatheter Delivery of a Shape Memory Polymer Foam Embolic Device for Treating Cerebral Aneurysms," *Journal of Medical Devices* **7**(2), 020932-020932-020932 (2013).
122. P. Diep et al., "Three-dimensional printed optical phantoms with customized absorption and scattering properties," *Biomed. Opt. Express* **6**(11), 4212-4220 (2015).
123. J. Wang et al., "Three-dimensional printing of tissue phantoms for biophotonic imaging," *Optics Letters* **39**(10), 3010-3013 (2014).
124. G. T. Smith et al., "Multimodal 3D cancer-mimicking optical phantom," *Biomed. Opt. Express* **7**(2), 648-662 (2016).
125. M. S. Durkee et al., "Fabrication and Characterization of Optical Tissue Phantoms Containing Macrostructure," *JoVE* **132**, e57031 (2018).
126. N. Mufti et al., "Fiber optic microendoscopy for preclinical study of bacterial infection dynamics," *Biomed. Opt. Express* **2**(5), 1121-1134 (2011).
127. X. Artaechevarria et al., "Evaluation of micro-CT for emphysema assessment in mice: comparison with non-radiological techniques," *European Radiology* **21**(5), 954-962 (2011).

128. N. L. Ford et al., "Optimization of a retrospective technique for respiratory-gated high speed micro-CT of free-breathing rodents," *Physics in Medicine and Biology* **52**(19), 5749 (2007).
129. X. Artaechevarria et al., "Airway segmentation and analysis for the study of mouse models of lung disease using micro-CT," *Physics in Medicine and Biology* **54**(22), 7009 (2009).
130. E. Namati et al., "Longitudinal assessment of lung cancer progression in the mouse using in vivo micro-CT imaging," *Medical Physics* **37**(9), 4793-4805 (2010).
131. W. Mitzner, R. Brown, and W. Lee, "In vivo measurement of lung volumes in mice," *Physiological Genomics* **4**(3), 215 (2001).
132. C. G. Tankersley, R. Rabold, and W. Mitzner, "Differential lung mechanics are genetically determined in inbred murine strains," *Journal of Applied Physiology* **86**(6), 1764 (1999).
133. C. Irvin, and J. Bates, "Measuring the lung function in the mouse: the challenge of size," *Respir Res* **4**(1), 1-9 (2003).
134. L. Bi et al., "Single-scattering properties of triaxial ellipsoidal particles for a size parameter range from the Rayleigh to geometric-optics regimes," *Appl. Opt.* **48**(1), 114-126 (2009).
135. M. U. Vera, A. Saint-Jalmes, and D. J. Durian, "Scattering optics of foam," *Appl. Opt.* **40**(24), 4210-4214 (2001).
136. D. J. Durian, D. A. Weitz, and D. J. Pine, "Multiple Light-Scattering Probes of Foam Structure and Dynamics," *Science* **252**(5006), 686 (1991).

137. L. Knudsen et al., "Assessment of air space size characteristics by intercept (chord) measurement: an accurate and efficient stereological approach," *J Appl Physiol* **108**(2), 412-421 (2010).
138. N. L. Ford et al., "Optimization of a retrospective technique for respiratory-gated high speed micro-CT of free-breathing rodents," *Phys Med Biol* **52**(19), 5749-5769 (2007).
139. C. G. Tankersley, R. S. Fitzgerald, and S. R. Kleeberger, "Differential control of ventilation among inbred strains of mice," *Am J Physiol Regul Integr Comp Physiol* **267**(5), R1371-R1377 (1994).
140. C. G. Tankersley, R. Rabold, and W. Mitzner, "Differential lung mechanics are genetically determined in inbred murine strains," *J Appl Physiol* **86**(6), 1764-1769 (1999).
141. E. Osmanagic et al., "Quantitative assessment of lung microstructure in healthy mice using an MR-based lung morphometry technique," *J Appl Physiol* **109**(6), 1592-1599 (2010).
142. "LightTools Biological Materials Library," Synopsys, Inc. (2014).
143. W. Small et al., "Fabrication and characterization of cylindrical light diffusers comprised of shape memory polymer," *J. Biomed. Opt.* **13**(2), 024018 (2008).
144. "IVIS Lumina System Manual," Xenogen Corporation (2006).
145. "LightTools Biological Materials Library," Synopsys, Inc. (2014).
146. M. S. Durkee et al., "Optical model of the murine lung to optimize pulmonary illumination," *J Biomed Opt* **23**(7), 071208 (2018).

147. M. S. Durkee, J. D. Cirillo, and K. C. Maitland, "A Fluorescence Model of the Murine Lung for Optical Detection of Pathogenic Bacteria," in SPIE Proceedings, *Clinical and Preclinical Optical Diagnostics* 104110H (2017).
148. D. Yager et al., "Airway surface liquid thickness as a function of lung volume in small airways of the guinea pig," *Journal of Applied Physiology* **77**(5), 2333 (1994).
149. S. Jayaraman et al., "Noninvasive in vivo fluorescence measurement of airway-surface liquid depth, salt concentration, and pH," *Journal of Clinical Investigation* **107**(3), 317-324 (2001).
150. M. Zellweger et al., "Absolute autofluorescence spectra of human healthy, metaplastic, and early cancerous bronchial tissue in vivo," *Appl. Opt.* **40**(22), 3784-3791 (2001).
151. Y. Kong et al., "Imaging tuberculosis with endogenous β -lactamase reporter enzyme fluorescence in live mice," *Proceedings of the National Academy of Sciences* **107**(27), 12239-12244 (2010).
152. J. T. Panteli et al., "Genetically modified bacteria as a tool to detect microscopic solid tumor masses with triggered release of a recombinant biomarker," *Integrative biology : quantitative biosciences from nano to macro* **7**(4), 423-434 (2015).
153. N. C. Shaner et al., "Improved monomeric red, orange and yellow fluorescent proteins derived from *Discosoma* sp. red fluorescent protein," *Nature Biotechnology* **22**(1567) (2004).
154. N. Soundrarajan et al., "Green fluorescent protein as a scaffold for high efficiency production of functional bacteriotoxic proteins in *Escherichia coli*," *Scientific Reports* **6**(20661) (2016).

155. M. S. Durkee, J. D. Cirillo, and K. C. E. D. B. J. Maitland, "A Fluorescence Model of the Murine Lung for Optical Detection of Pathogenic Bacteria," in SPIE Proceedings, *Clinical and Preclinical Optical Diagnostics* 104110H (2017).
156. B. Marais et al., "A proposed radiological classification of childhood intra-thoracic tuberculosis," *Pediatr Radiol* **34**(11), 886-894 (2004).
157. P. Piccini et al., "Clinical peculiarities of tuberculosis," *BMC Infectious Diseases* **14**(1), S4 (2014).
158. H. J. Zar et al., "Induced sputum versus gastric lavage for microbiological confirmation of pulmonary tuberculosis in infants and young children: a prospective study," *The Lancet* **365**(9454), 130-134 (2005).
159. M. R. Boloursaz et al., "Radiologic Manifestation of Pulmonary Tuberculosis in Children Admitted in Pediatric Ward-Massih Daneshvari Hospital: A 5-Year Retrospective Study," *Acta Medica Iranica; Vol Vol. 48, No No. 4* (2010).
160. S. K. Sharma et al., "Miliary tuberculosis: new insights into an old disease," *The Lancet Infectious Diseases* **5**(7), 415-430 (2005).
161. P. J. Dodd, C. Sismanidis, and J. A. Seddon, "Global burden of drug-resistant tuberculosis in children: a mathematical modelling study," *The Lancet Infectious Diseases* **16**(10), 1193-1201 (2016).
162. P. Glaziou et al., "Global Epidemiology of Tuberculosis," *Cold Spring Harbor Perspectives in Medicine* **5**(2), (2015).
163. S. K. Sharma et al., "Cytokine Polarization in Miliary and Pleural Tuberculosis," *Journal of Clinical Immunology* **22**(6), 345-352 (2002).
164. P. D. O. Davies, "The mycobacterioses," *Imaging (09656812)* **20**(4), 252-263 (2008).

165. P. J. Sime, E. R. Chilvers, and A. G. Leitch, "Miliary tuberculosis in edinburgh—A comparison between 1984–1992 and 1954–1967," *Respiratory Medicine* **88**(8), 609-611 (1994).
166. S. Menitove, and H. W. Harris, "Miliary Tuberculosis," in *Tuberculosis* D. Schlossberg, Ed., pp. 179-189, Springer New York, New York, NY (1988).
167. G. Davies, and L. Reid, "Growth of the alveoli and pulmonary arteries in childhood," *Thorax* **25**(6), 669-681 (1970).

APPENDIX A

Listed below are the inputs to the fluorescence model of murine infection including mouse tissue optical properties, tissue autofluorescence spectra, and bacteria fluorescence spectra.

Lung optical properties								
Refractive Index		1.396						
<i>Tissue Reduced MFP (mm)</i>			<i>Tissue Transmissivity (T)</i>			<i>Alveoli</i>		
λ (nm)	Healthy	Infected	λ (nm)	Healthy	Infected	λ (nm)	MFP (mm)	T
469	0.2608	0.3097	469	0.9707	0.9465	400	0.1530	1
493	0.1940	0.2428	493	0.9701	0.9249	420	0.1539	1
517	0.2044	0.2629	517	0.9666	0.9141	440	0.1547	1
541	0.1971	0.2443	541	0.9595	0.8704	460	0.1549	1
565	0.1878	0.2915	565	0.9596	0.8652	480	0.1548	1
589	0.1703	0.2741	589	0.9654	0.8666	500	0.1544	1
613	0.1600	0.2921	613	0.9827	0.9323	520	0.1538	1
637	0.1940	0.3112	637	0.9857	0.9514	540	0.1531	1
661	0.1935	0.3305	661	0.9880	0.9609	560	0.1525	1
685	0.2074	0.3113	685	0.9878	0.9649	580	0.1520	1
709	0.1985	0.3433	709	0.9901	0.9672	600	0.1513	1
733	0.2260	0.3540	733	0.9897	0.9736	620	0.1508	1
757	0.2126	0.3531	757	0.9827	0.9650	640	0.1505	1
781	0.2606	0.3870	781	0.9897	0.9681	660	0.1503	1
805	0.2124	0.3530	805	0.9876	0.9714	680	0.1502	1
829	0.3155	0.3373	829	0.9860	0.9740	700	0.1503	1
853	0.2667	0.3736	853	0.9883	0.9902	720	0.1506	1
877	0.5125	0.3826	877	0.9939	0.9897	740	0.1507	1
901	5.8662	0.2931	901	1.0000	0.9991	760	0.1508	1
						780	0.1511	1
						800	0.1513	1
						820	0.1517	1
						840	0.1522	1

Heart optical properties		
<i>Refractive Index</i>	1.371	
λ (nm)	MFP (mm)	Transmissivity
665	0.0080	0.8781
685	0.0071	0.7672
960	0.0198	0.7528

Bulk tissue optical properties		
<i>Refractive Index</i>	1.396	
λ (nm)	MFP(mm)	Transmissivity
665	3.0613	0.8990
685	3.2191	0.9010
960	4.7971	0.9430

Tissue Autofluorescence Absorption	
λ (nm)	Absorption Value
490	0.2380
505	0.2143
520	0.1930
535	0.1737
550	0.1564
565	0.1408
580	0.1268
595	0.1141
610	0.1028
625	0.0925
640	0.0833
655	0.0750
670	0.0675
685	0.0608
700	0.0547
715	0.0493
730	0.0444
745	0.0399
760	0.0360
775	0.0324
790	0.0292
805	0.0262

Tissue Autofluorescence							
Particle number density	1e4-1e5 /mm ³						
Particle radius	1000 nm						
Conversion Efficiency (all λ)	1						
<i>Em. λ \ Ex.</i>							
λ	480	500	520	540	560	580	600
560	0.9900	0.0000	0.0000	0.0000	0.0000	0.0000	0.0000
580	0.8520	0.9900	0.0000	0.0000	0.0000	0.0000	0.0000
600	0.4910	0.8520	0.9900	0.0000	0.0000	0.0000	0.0000
620	0.2190	0.4910	0.8520	0.9900	0.0000	0.0000	0.0000
640	0.0810	0.2190	0.4910	0.8520	0.9900	0.0000	0.0000
660	0.0300	0.0810	0.2190	0.4910	0.8520	0.9900	0.0000
680	0.0087	0.0300	0.0810	0.2190	0.4910	0.8520	0.9900
700	0.0031	0.0087	0.0300	0.0810	0.2190	0.4910	0.8520
720	0.0011	0.0031	0.0087	0.0300	0.0810	0.2190	0.4910
740	0.0004	0.0011	0.0031	0.0087	0.0300	0.0810	0.2190
760	0.0001	0.0004	0.0011	0.0031	0.0087	0.0300	0.0810
780	0.0001	0.0001	0.0004	0.0011	0.0031	0.0087	0.0300
800	0.0000	0.0001	0.0001	0.0004	0.0011	0.0031	0.0087
820	0.0000	0.0000	0.0001	0.0001	0.0004	0.0011	0.0031
840	0.0000	0.0000	0.0000	0.0001	0.0001	0.0004	0.0011
860	0.0000	0.0000	0.0000	0.0000	0.0001	0.0001	0.0004
880	0.0000	0.0000	0.0000	0.0000	0.0000	0.0001	0.0001
900	0.0000	0.0000	0.0000	0.0000	0.0000	0.0000	0.0001
920	0.0000	0.0000	0.0000	0.0000	0.0000	0.0000	0.0000
940	0.0000	0.0000	0.0000	0.0000	0.0000	0.0000	0.0000

Tissue Autofluorescence (cont'd)

<i>Em. λ</i>									
<i>Ex. λ</i>	620	640	660	680	700	720	740	760	780
560	0.0000	0.0000	0.0000	0.0000	0.0000	0.0000	0.0000	0.0000	0.0000
580	0.0000	0.0000	0.0000	0.0000	0.0000	0.0000	0.0000	0.0000	0.0000
600	0.0000	0.0000	0.0000	0.0000	0.0000	0.0000	0.0000	0.0000	0.0000
620	0.0000	0.0000	0.0000	0.0000	0.0000	0.0000	0.0000	0.0000	0.0000
640	0.0000	0.0000	0.0000	0.0000	0.0000	0.0000	0.0000	0.0000	0.0000
660	0.0000	0.0000	0.0000	0.0000	0.0000	0.0000	0.0000	0.0000	0.0000
680	0.0000	0.0000	0.0000	0.0000	0.0000	0.0000	0.0000	0.0000	0.0000
700	0.9900	0.0000	0.0000	0.0000	0.0000	0.0000	0.0000	0.0000	0.0000
720	0.8520	0.9900	0.0000	0.0000	0.0000	0.0000	0.0000	0.0000	0.0000
740	0.4910	0.8520	0.9900	0.0000	0.0000	0.0000	0.0000	0.0000	0.0000
760	0.2190	0.4910	0.8520	0.9900	0.0000	0.0000	0.0000	0.0000	0.0000
780	0.0810	0.2190	0.4910	0.8520	0.9900	0.0000	0.0000	0.0000	0.0000
800	0.0300	0.0810	0.2190	0.4910	0.8520	0.9900	0.0000	0.0000	0.0000
820	0.0087	0.0300	0.0810	0.2190	0.4910	0.8520	0.9900	0.0000	0.0000
840	0.0031	0.0087	0.0300	0.0810	0.2190	0.4910	0.8520	0.9900	0.0000
860	0.0011	0.0031	0.0087	0.0300	0.0810	0.2190	0.4910	0.8520	0.9900
880	0.0004	0.0011	0.0031	0.0087	0.0300	0.0810	0.2190	0.4910	0.8520
900	0.0001	0.0004	0.0011	0.0031	0.0087	0.0300	0.0810	0.2190	0.4910
920	0.0001	0.0001	0.0004	0.0011	0.0031	0.0087	0.0300	0.0810	0.2190
940	0.0000	0.0001	0.0001	0.0004	0.0011	0.0031	0.0087	0.0300	0.0810

tdTomato Fluorescence	
Particle number density	1- 1e7/mm ³
Particle radius	1500 nm
Conversion Efficiency (all λ)	1
<i>Em. WL\Ex. WL</i>	<i>535</i>
<i>490</i>	0.275
<i>500</i>	0.498
<i>510</i>	0.705
<i>520</i>	0.857
<i>530</i>	0.941
<i>540</i>	0.977
<i>550</i>	0.99
<i>560</i>	0.99
<i>570</i>	0.974
<i>580</i>	0.995
<i>590</i>	0.852
<i>600</i>	0.76
<i>610</i>	0.677
<i>620</i>	0.583
<i>630</i>	0.491
<i>640</i>	0.407
<i>650</i>	0.333
<i>660</i>	0.274
<i>670</i>	0.219
<i>680</i>	0.174
<i>690</i>	0.139
<i>700</i>	0.104
<i>710</i>	0.081
<i>720</i>	0.065
<i>730</i>	0.049
<i>740</i>	0.039
<i>750</i>	0.03
<i>760</i>	0.02
<i>770</i>	0.016
<i>780</i>	0.009

CNIR REF Probe Fluorescence	
Particle number density	1-1e7 /mm ³
Particle radius	1500 nm
Conversion Efficiency (all λ)	1
<i>Em. WL\Ex. WL</i>	<i>730</i>
<i>750</i>	0.606531
<i>760</i>	0.726149
<i>770</i>	0.83527
<i>780</i>	0.923116
<i>790</i>	0.9801
<i>800</i>	1
<i>810</i>	0.982199
<i>820</i>	0.923116
<i>830</i>	0.83527
<i>840</i>	0.726149
<i>850</i>	0.606531
<i>860</i>	0.486752
<i>870</i>	0.375311
<i>880</i>	0.278037
<i>890</i>	0.197899
<i>900</i>	0.135335
<i>910</i>	0.088922
<i>920</i>	0.056135

APPENDIX B

Appendix B contains the code for the multi-layer concentric sphere model.

```
clc;
%demoMie_shell_constant_ASL_vol.m
%
% Demonstrate use of Maetzler's MATLAB Mie calculation.
% Plots scattering, anisotropy, and reduced scattering
% for a range of wavelengths and range of particle diameters.
% - Steven Jacques 2009
%
% Christian Maetzler,
% MATLAB Functions for Mie Scattering and Absorption
% University of Bern, Institut fuer Angewandte Physik,
% Research Report No. 2002-08, June, 2002
% http://arcc.ou.edu/~rockee/NRA\_2007\_website/Mie-scattering-Matlab.pdf

% Corrected some errors, added table printing function in getMieScatter.m
% -Rob Brown, Rockwell Collins, June 2017
    %home
    %disp('=====')
    %disp('lambda outer dia inner dia rho mus g ') %header for printing
table of interesting parameters for use elsewhere...
%disp('lambda dia rho npar nmed real(m) imag(m) x qext qsca qabs qb asy
qratio mus g musp')

% Converted eqs. to concentric sphere Mie scattering model in mie_abcd.m file
% Other nested functions adjusted to account for extra inputs
% New file names: demoMie_shell.m, getMieScatter_shell.m, mie_shell.m,
% mie_abcd_shell.m
% - Madeleine S. Durkee, October 2017

% Adapted shell model to maintain constant shell volume when OD changes
% New file names: demoMie_shell_constant_ASL_vol.m, demoMie_shell_loop.m
% - Madeleine S. Durkee, February 2018

%%%
% USER CHOICES
%%%
%% tissue model

n_med = 1.4;
n_par = 1.00;
n_shell = 1.33;
fv = [0.62 0.77 0.81 0.88];

outdia = [157.81 198.82 214.17 269.84];
asl_vol = (4/3)*pi*((outdia(3)/2)^3-((outdia(3)/2)-0.005*(outdia(3)/2))^3);
d = zeros(1,4);
for index = 0:3
    d(index+1) = (outdia(index+1)/2)-((outdia(index+1)/2)^3-
(3*asl_vol/(4*pi)))^(1/3);
```

```

end
% inner_diadia2 = zeros(length(outer_diadia),length(d));
%
% for index = 1:length(d)
%     for index2 = 1:length(outer_diadia)
%         inner_diadia2(index,index2) = outer_diadia(index)-d(index2);
%     end
% end

%change n, vf, outer dia, inner dia

l_outherdia = length(outdia);
Lambda = zeros(1,451);
MusGP = zeros(451,l_outherdia,3);

for ii = 1:4
    india(ii) = outdia(ii)-2*d(ii);
    [Lambda,MusGP(:,ii,:)] =
demoMie_shell_loop(n_med,n_par,n_shell,fv(ii),outdia(ii),india(ii));
end

        %% plot results
figure(2);clf
clr = 'rgbmckyrb';
sz = 14;

yname(1).s = '\mu_s [cm^{-1}]';
yname(2).s = 'g [-]';
yname(3).s = '\mu_s' [cm^{-1}]';
ymax = [3000 1 400];

for k=1:3

    subplot(3,1,k)
    for j=1:l_outherdia
        switch j
            case 1
                name = 'no ASL, V_{Tmax}';
            case 2
                name = 'RV';
            case 3
                name = 'FRC';
            case 4
                name = 'V_{Tmax}';
            case 5
                name = 'TLC';
        end
        plot(Lambda, MusGP(:,j,k),[clr(j) '-'],'DisplayName',name)
        hold on
        y = ymax(k); dy = y/10; x = mean(Lambda);

    end
    set(gca,'fontsize',sz)
    xlabel('wavelength \lambda [\mu m]')
    ylabel(yname(k).s)

```

end

```
function [lambdalambda,musgp] =
demoMie_shell_loop(nmed,npar,nshell,vf,outer_diadia,inner_diadia);

lambdalambda = .4:.001:.85; % [um] (starting wavelength, interval, ending
wavelength)
%outer_diadia = [50 75 100 150 200 250]'; % [um] list them, [a b c]
%inner_diadia = [50 75 100 150 200 250]';%[155.33 155.25 155.15 154.35 153.85
153.35]'; % [um] list them, [a b c], must be less than outer_diadia

musgp = zeros(length(lambdalambda),1,3);

    out_dia = outer_diadia;
    in_dia = inner_diadia;

    for i=1:length(lambdalambda)
        lambda = lambdalambda(i);

            [musgp(i,1,:)] = getMieScatter_shell(lambda, out_dia, in_dia, vf,
npar, nmed, nshell);

    end % i
```

end

```
clc;
%demoMie.m
%
% Demonstrate use of Maetzler's MATLAB Mie calculation.
% Plots scattering, anisotropy, and reduced scattering
% for a range of wavelengths and range of particle diameters.
% - Steven Jacques 2009
%
% Christian Maetzler,
% MATLAB Functions for Mie Scattering and Absorption
% University of Bern, Institut fuer Angewandte Physik,
% Research Report No. 2002-08, June, 2002
% http://arcc.ou.edu/~rockee/NRA\_2007\_website/Mie-scattering-Matlab.pdf

% Corrected some errors, added table printing function in getMieScatter.m
% -Rob Brown, Rockwell Collins, June 2017
    %home
    %disp('=====')
    %disp('lambda outer dia inner dia rho mus g ') %header for printing
table of interesting parameters for use elsewhere...
%disp('lambda dia rho npar nmed real(m) imag(m) x qext qsca qabs qb asy
qratio mus g musp')
```

```

% Converted eqs. to concentric sphere Mie scattering model in mie_abcd.m file
% Other nested functions adjusted to account for extra inputs
% New file names: demoMie_shell.m, getMieScatter_shell.m, mie_shell.m,
% mie_abcd_shell.m
% - Madeleine S. Durkee, October 2017

%%
% USER CHOICES
%%

nmed = 1.40; % medium refractive index (air)
npar = 1.00; % particle refractive index (water)
nshell = 1.33; % shell refractive index glass or surfactant
vf = 0.81; % volume fraction of spheres in medium (PAY ATTENTION TO THIS.
Rho (concentration) changes with particle size!)

lambdalambda = .4:.001:.85; % [um] (starting wavelength, interval, ending
wavelength)
outer_diadia = [67.39]'; % [um] list them, [a b c]
inner_diadia = [67.39 67.37 67.29 67.19 66.39 65.39]'; % [155.33 155.25 155.15
154.35 153.85 153.35]'; % [um] list them, [a b c], must be less than
outer_diadia

musgp = zeros(length(lambdalambda),length(outer_diadia),3);

for j=1:length(inner_diadia)
    out_dia = outer_diadia;
    in_dia = inner_diadia(j);

    for i=1:length(lambdalambda)
        lambda = lambdalambda(i);

        [musgp(i,j,:)] = getMieScatter_shell(lambda, out_dia, in_dia, vf,
npar, nmed, nshell);

    end % i

end % j

%% plot results
figure(2);clf
clr = 'rgbmckyrb';
sz = 14;

yname(1).s = '\mu_s [cm^{-1}]';
yname(2).s = 'g [-]';
yname(3).s = '\mu_s'' [cm^{-1}]';
ymax = [3000 1 400];

for k=1:3

    subplot(3,1,k)
    for j=1:length(inner_diadia)

```

```

switch j
    case 1
        name = 'no shell';
    case 2
        name = '10 nm';
    case 3
        name = '50 nm';
    case 4
        name = '100 nm';
    case 5
        name = '500 nm';
    case 6
        name = '1000 nm';
    case 7
        name = '150 um';
    case 8
        name = '200 um';
    case 9
        name = '250 um';
end
plot(lambdalambda, musgp(:,j,k),[clr(j) '-'],'DisplayName',name)
hold on
y = ymax(k); dy = y/10; x = mean(lambdalambda);

end
set(gca,'fontsize',sz)
xlabel('wavelength \lambda [\umum]')
ylabel(yname(k).s)
end

disp('done')

```

```

function [musgp] = getMieScatter_shell(lambda, out_dia, in_dia, fv,
npar,nmed,nshell)
% function musgp = getMieScatter(lambda, dia, fv)
% fv          = volume fraction of spheres in medium (eg., fv = 0.05)
% lambda      = wavelength in um (eg., lambda = 0.633)
% dia         = sphere diameter in um (eg., dia_um = 0.0500)
% npar        = particle refractive index (eg. polystyrene = 1.57)
% nmed        = medium refractive index (eg., water = 1.33)
%             Note: npar and nmed can be imaginary numbers.
% returns musgp = [mus g musp]
%     mus       = scattering coefficient [cm^-1]
%     g         = anisotropy of scattering [dimensionless]
%     musp      = reduced scattering coefficient [cm^-1]
% Uses
%     Mie.m, which uses mie_abcd.m, from Maetzler 2002
%
% - Steven Jacques, 2009

% Corrected some errors, added table format printing of selected
% parameters. -Rob Brown, Rockwell Collins, June 2017

V1 = 4/3*pi*(out_dia/2)^3;      % volume 1

```

```

V2 = 4/3*pi*(in_dia/2)^3;      % volume inner sphere
V3 = V1-V2;                    % volume of shell

d_shell = (out_dia-in_dia)/2;  % thickness of shell
r_in = in_dia/2;

rho      = fv/V1;              % #/um^3, concentration of spheres

m_13 = npar/nmed;              % ratio of refractive indices
m_23 = nshell/nmed;

x_1 = pi*in_dia/(lambda/nmed); % ratio circumference/wavelength in
medium
x_2 = pi*out_dia/(lambda/nmed);

if r_in == 0;
    r_in = out_dia/2;
    x_1 = x_2;
    m_13 = m_23;
end

[u] = mie_shell(m_13, m_23, x_1, x_2, r_in); % <----- Matzler's subroutine
u = u';

% u = [real(m_13) imag(m_13) real(m_23) imag(m_23) x_1 x_2 qext qsca qabs qb
asy qratio];
%% edited through here 20171027
qsca = u(8);                   % scattering efficiency, Qsca
g      = u(11);                 % anisotropy, g

A      = pi*out_dia^2/4;        % geometrical cross-sectional area, um^2
sigma_s = qsca*A;              % scattering cross-section, um^2
mus     = sigma_s*rho*1e4;      % scattering coeff. cm^-1
musp    = mus*(1-g);           % reduced scattering coeff. cm^-1

if 0 % 1 = print full report, 0 = disable
    disp('----- choice:')
    fprintf('lambda   \t= %0.3f um\n', lambda)
    fprintf('out_dia   \t= %0.3f um\n', out_dia)
    fprintf('in_dia    \t= %0.3f\n', in_dia)
    fprintf('rho       \t= %0.3f #/um^3\n', rho)
    fprintf('npar      \t= %0.3f\n', npar)
    fprintf('nmed      \t= %0.3f\n', nmed)
    fprintf('nshell   \t= %0.3f\n', nshell)
    disp('----- result:')
    fprintf('real(m_13) \t= %0.3f\n', u(1))
    fprintf('imag(m_13) \t= %0.3f\n', u(2))
    fprintf('real(m_23) \t= %0.3e\n', u(3))
    fprintf('imag(m_23) \t= %0.3f\n', u(4))
    fprintf('x_1       \t= %0.3e\n', u(5))
    fprintf('x_2       \t= %0.3e\n', u(6))
    fprintf('qext      \t= %0.3e\n', u(7))
    fprintf('qsca      \t= %0.3e\n', u(8))
    fprintf('qabs      \t= %0.3e\n', u(9))
    fprintf('qb       \t= %0.3e\n', u(10))

```

```

fprintf('asy      \t= %0.4f\n', u(11))
fprintf('qratio  \t= %0.3e\n', u(12))
disp('----- optical properties:')
fprintf('mus      \t= %0.3f cm^-1\n', mus)
fprintf('g        \t= %0.4f\n', g)
fprintf('musp     \t= %0.3f cm^-1\n', musp)
end
%Print the just parameters you want, in table format. Mod header from
%demoMie (line 15) to properly label columns
fprintf('%0.3f %0.3f %0.3f %0.3f %0.3f %0.3f %0.3f %0.3f %0.3f %0.3f\n',
lambda, dia, rho, npar, nmed,
u(1),u(2),u(3),u(4),u(5),u(6),u(7),u(8),u(9), mus, g, musp)
fprintf('%0.3f %0.3f %0.3f %0.6f %0.3f %0.3f\n', lambda, out_dia, in_dia,
rho, mus, g)

musgp= real([mus g musp]);

```

```

function [result] = mie_shell(m_13, m_23, x_1, x_2, r_in)

% Computation of Mie Efficiencies for given
% complex refractive-index ratio m=m'+im"
% and size parameter x=k0*a, where k0= wave number in ambient
% medium, a=sphere radius, using complex Mie Coefficients
% an and bn for n=1 to nmax,
% s. Bohren and Huffman (1983) BEWI:TDD122, p. 103,119-122,477.
% Result: m', m", x, efficiencies for extinction (qext),
% scattering (qsca), absorption (qabs), backscattering (qb),
% asymmetry parameter (asy=<costeta>) and (qratio=qb/qsca).
% Uses the function "mie_abcd" for an and bn, for n=1 to nmax.
% C. MŠtzler, May 2002.

if x_2==0 % To avoid a singularity at x=0
    result=[real(m_13) imag(m_13) real(m_23) imag(m_23) 0 0 0 0 0 0 1.5];
elseif x_2>0 % This is the normal situation
    % summation terms
    nmax=round(2+x_2+4*x_2^(1/3));
    n1=nmax-1;
    n=(1:nmax);
    % coefficient for E and B fields
    cn=2*n+1; c1n=n.*(n+2)./(n+1); c2n=cn./n./(n+1);
    % size parameter squared
    x1_2 = x_1*x_1;
    x2_2=x_2*x_2;
    % get Mie coefficients
    f=mie_abcd_shell(m_13, m_23, x_1, x_2, r_in);
    % real and imaginary parts of an_in coefficient
    anp=(real(f(1,:))); anpp=(imag(f(1,:)));
    % real and imaginary parts of an_out coefficient
    bnp=(real(f(2,:))); bnpp=(imag(f(2,:)));
    % real and imaginary parts of bn_in coefficient
    bnp_in=(real(f(3,:))); bnpp_in=(imag(f(3,:)));
    % real and imaginary parts of bn_out coefficient
    bnp_out=(real(f(4,:))); bnpp_out=(imag(f(4,:)));
    g1(1:4,nmax)=[0; 0; 0; 0]; % displaced numbers used for

```

```

g1(1,1:n1)=anp(2:nmax); % asymmetry parameter, p. 120
g1(2,1:n1)=anpp(2:nmax);
g1(3,1:n1)=bnp(2:nmax);
g1(4,1:n1)=bnpp(2:nmax);
dn=cn.*(anp+bnp); % real part of sum of a_n and b_n
q=sum(dn);
qext=2*q/x2_2; % extinction coefficient; based on size parameter of
larger r
en=cn.*(anp.*anp+anpp.*anpp+bnp.*bnp+bnpp.*bnpp); % sum of magnitudes of
a_n and b_n
q=sum(en); % re-establish q
qsca=2*q/x2_2; % scattering coefficient; based on size parameter of
larger r
qabs=qext-qsca;
fn=(f(1,:)-f(2,:)).*cn;
gn=(-1).^n;
test=fn.*gn;
q=sum(test);
qb=q*q'/x2_2;
% asymmetry parameter
asy1=c1n.*(anp.*g1(1,:)+anpp.*g1(2,:)+bnp.*g1(3,:)+bnpp.*g1(4,:));
asy2=c2n.*(anp.*bnp+anpp.*bnpp);
asy=4/x2_2*sum(asy1+asy2)/qsca;
qratio=qb/qsca;
% result gives real and imaginary parts of refractive index for each
layer, size
% parameter for each layer, extinction efficiency, scattering efficiency,
backscatter
% efficiency, asymmetry parameter, and ratio of backscatter efficiency
% to scattering efficiency
result=[real(m_13) imag(m_13) real(m_23) imag(m_23) x_1 x_2 qext qsca
qabs qb asy qratio];
end;

```

```
function result = mie_abcd_shell(m_13, m_23, x_1, x_2, r_in)
```

```

% Computes a matrix of Mie coefficients, a_n, b_n, c_n, d_n,
% of orders n=1 to nmax, complex refractive index m=m'+im",
% and size parameter x=k0*a, where k0= wave number
% in the ambient medium, a=sphere radius;
% p. 100, 477 in Bohren and Huffman (1983) BEWI:TDD122
% C. MŠtzler, June 2002

```

```

% terms of summation
nmax=round(2+x_2+4*x_2^(1/3));
n=(1:nmax);
% Step for spherical Bessel and Hankel functions
nu = (n+0.5);
% ratio of circumference to wavelength in particle layer
a = x_1;
v = x_2;
N1 = m_13;
N2 = m_23;
N1a = N1.*a;
N1v = N1.*v;

```

```

N2a = N2.*a;
N2v = N2.*v;
% Y terms
Y1 = (m_13.*a)./r_in;
Y2 = (m_23.*a)./r_in;
Y3 = a./r_in;
% Bessel coefficients
sqa = sqrt(0.5*pi./a);
sqv = sqrt(0.5*pi./v);
sqN1a = sqrt(0.5*pi./N1a);
sqN1v = sqrt(0.5*pi./N1v);
sqN2a = sqrt(0.5*pi./N2a);
sqN2v = sqrt(0.5*pi./N2v);
% bessel fn of first kind
ba = besselj(nu,a).*sqa;
bv = besselj(nu,v).*sqv;
bN1a = besselj(nu,N1a).*sqN1a;
bN1v = besselj(nu,N1v).*sqN1v;
bN2a = besselj(nu,N2a).*sqN2a;
bN2v = besselj(nu,N2v).*sqN2v;
% bessel fn of second kind
ba2 = bessely(nu,a).*sqa;
bv2 = bessely(nu,v).*sqv;
bN1a2 = bessely(nu,N1a).*sqN1a;
bN1v2 = bessely(nu,N1v).*sqN1v;
bN2a2 = bessely(nu,N2a).*sqN2a;
bN2v2 = bessely(nu,N2v).*sqN2v;
% Hankel fn of first kind
ha = ba+1i.*ba2;
hv = bv+1i.*bv2;
hN1a = bN1a+1i.*bN1a2;
hN1v = bN1v+1i.*bN1v2;
hN2a = bN2a+1i.*bN2a2;
hN2v = bN2v+1i.*bN2v2;
% derivative term, bessel fn of first kind
dba = [sin(a)/a, ba(1:nmax-1)];
dbv = [sin(v)/v, bv(1:nmax-1)];
dbN1a = [sin(N1a)/N1a, bN1a(1:nmax-1)];
dbN1v = [sin(N1v)/N1v, bN1v(1:nmax-1)];
dbN2a = [sin(N2a)/N2a, bN2a(1:nmax-1)];
dbN2v = [sin(N2v)/N2v, bN2v(1:nmax-1)];
% derivative term, bessel fn of second kind
dba2 = [-cos(a)/a, ba2(1:nmax-1)];
dbv2 = [-cos(v)/v, bv2(1:nmax-1)];
dbN1a2 = [-cos(N1a)/N1a, bN1a2(1:nmax-1)];
dbN1v2 = [-cos(N1v)/N1v, bN1v2(1:nmax-1)];
dbN2a2 = [-cos(N2a)/N2a, bN2a2(1:nmax-1)];
dbN2v2 = [-cos(N2v)/N2v, bN2v2(1:nmax-1)];
% derivative term, hankel
dha = dba+1i.*dba2;
dhv = dbv+1i.*dbv2;
dhN1a = dbN1a+1i.*dbN1a2;
dhN1v = dbN1v+1i.*dbN1v2;
dhN2a = dbN2a+1i.*dbN2a2;
dhN2v = dbN2v+1i.*dbN2v2;
% eta functions; bessel
eta1_a = (a.*dba-n.*ba)./a;

```

```

eta1_v = (v.*dbv-n.*bv)./v;
eta1_N1a = (N1a.*dbN1a-n.*bN1a)./N1a;
eta1_N1v = (N1v.*dbN1v-n.*bN1v)./N1v;
eta1_N2a = (N2a.*dbN2a-n.*bN2a)./N2a;
eta1_N2v = (N2v.*dbN2v-n.*bN2v)./N2v;
% eta functions; hankel
eta3_a = (a.*dha-n.*ha)./a;
eta3_v = (v.*dhv-n.*hv)./v;
eta3_N1a = (N1a.*dhN1a-n.*hN1a)./N1a;
eta3_N1v = (N1v.*dhN1v-n.*hN1v)./N1v;
eta3_N2a = (N2a.*dhN2a-n.*hN2a)./N2a;
eta3_N2v = (N2v.*dhN2v-n.*hN2v)./N2v;

% solution terms
A1 = (Y2.^2).*eta1_N1a.*(bN2v.*hN2a-
bN2a.*hN2v)+Y1.*Y2.*bN1a.*(eta1_N2a.*hN2v-eta3_N2a.*bN2v);
A2 = Y2.*eta1_N1a.*(bN2a.*eta3_N2v-
hN2a.*eta1_N2v)+Y1.*bN1a.*(eta1_N2v.*eta3_N2a-eta1_N2a.*eta3_N2v);
A3 = (Y2.^2).*bN1a.*(eta1_N2v.*eta3_N2a-
eta1_N2a.*eta3_N2v)+Y1.*Y2.*eta1_N1a.*(bN2a.*eta3_N2v-hN2a.*eta1_N2v);
A4 = Y2.*bN1a.*(eta1_N2a.*hN2v-eta3_N2a.*bN2v)+Y1.*eta1_N1a.*(bN2v.*hN2a-
bN2a.*hN2v);

an = -(eta1_v.*A1+Y3.*bv.*A2)./(eta3_v.*A1+Y3.*hv.*A2);
bn = -(bv.*A3+Y3.*eta1_v.*A4)./(hv.*A3+Y3.*eta3_v.*A4);

result = [an; bn];
end

```